



저작자표시-비영리-변경금지 2.0 대한민국

이용자는 아래의 조건을 따르는 경우에 한하여 자유롭게

- 이 저작물을 복제, 배포, 전송, 전시, 공연 및 방송할 수 있습니다.

다음과 같은 조건을 따라야 합니다:



저작자표시. 귀하는 원저작자를 표시하여야 합니다.



비영리. 귀하는 이 저작물을 영리 목적으로 이용할 수 없습니다.



변경금지. 귀하는 이 저작물을 개작, 변형 또는 가공할 수 없습니다.

- 귀하는, 이 저작물의 재이용이나 배포의 경우, 이 저작물에 적용된 이용허락조건을 명확하게 나타내어야 합니다.
- 저작권자로부터 별도의 허가를 받으면 이러한 조건들은 적용되지 않습니다.

저작권법에 따른 이용자의 권리는 위의 내용에 의하여 영향을 받지 않습니다.

이것은 [이용허락규약\(Legal Code\)](#)을 이해하기 쉽게 요약한 것입니다.

[Disclaimer](#)

공학박사 학위논문

**First principles study on overall reaction
mechanism for tungsten atomic layer
deposition in the early stages**

텅스텐 원자층 증착 초기단계에서의 전반적인 반응
메커니즘에 대한 제일원리계산 연구

2019년 2월

서울대학교 대학원
재료공학부
박 환 열

Abstract

First principles study on overall reaction mechanism for tungsten atomic layer deposition in the early stages

Hwanyeol Park

Department of Materials and Science and Engineering

College of Engineering

Seoul National University

Following Moore's law for decades, thin film deposition techniques have been intensively advanced to meet the demand for miniaturized and highly integrated devices in the electronics industry. Recently, conformal film deposition techniques, which allows precise thickness control at atomic scale, are becoming very important. Nitride materials, such as titanium nitride and silicon nitride, have been deposited using conventional deposition methods such as low-pressure chemical vapor deposition (LPCVD), plasma-enhanced chemical vapor deposition (PECVD). However, development of memory devices has required another deposition technique such as atomic layer deposition (ALD) to meet the demand for excellent step coverage and high

conformality on extremely high aspect ratio structures. The ALD processes utilize well-controlled sequential surface reactions to obtain uniform and conformal films.

As one of the most essential materials in fabrication of future memory devices, tungsten (W) has been used for a metal gate with lower resistivity than other candidate materials, which results in enhancement of device performance. In the fabrication of recent memory devices, tungsten films have been deposited using ALD by alternatively exposing W precursors such as tungsten hexafluoride (WF_6) and reducing agents such as diborane (B_2H_6) in an ABAB... sequence. In the ALD processes for W deposition, B_2H_6 dosing process can play an important role in deposition of W films with low resistivity and in removal of residual fluorine (F) atoms on the surface.

However, as the size of the memory device becomes smaller and smaller, it becomes difficult to deposit W films having excellent step coverage and conformality due to a severe problem that a seam or void is formed in the process of filling the W metal gate. This problem is a primary obstacle of the development for future memory devices. To treat this problem, theoretical comprehension of the ALD process for W deposition is required due to the experimentally limited observations on the sub-nanometer scale. Although a few experimental results on ALD W have been reported, there has been no theoretical report on the overall reaction mechanism for ALD W process.

Firstly, we have investigated the dissociation reaction of B_2H_6 on three different TiN surfaces, TiN (001), Ti-terminated TiN (111), and N-terminated TiN (111), using DFT calculations. N-terminated TiN (111) shows the lowest overall reaction energy for B_2H_6 . These results imply that severe problems, such as a seam or void, in filling the W metal gate for memory devices could

be attributed to the difference in the deposition rate of W films on TiN surfaces. From this study, it was found that the control of the texture of the TiN film is essential for improving the subsequent W nucleation.

Secondly, we have investigated the effects of H₂ and N₂ treatment on TiN surfaces for B₂H₆ dosing process. In our DFT calculated results, H₂ treatment on the TiN surfaces is to make the surface to be H-covered TiN surfaces, which results in lowering the reactivity of B₂H₆ precursor since the overall reactions of the B₂H₆ on the H-covered TiN surfaces are energetically less favorable than the TiN surfaces. As a result, an effect of the H₂ treatment is to decrease the reactivity of the B₂H₆ molecule on the TiN surface. However, N₂ treatment on Ti-terminated TiN (111) surface is more likely to make the TiN surface to be N-terminated TiN (111) surface, which results in making a lot of N-terminated TiN (111) surfaces, having very reactive nature for B₂H₆ bond dissociation. As a result, the effect of N₂ treatment serves as a catalyst to decompose B₂H₆. From the deep understanding of the effect of H₂ and N₂ during the B₂H₆ dosing process, the use of proper gas treatment is required for improvement of the W nucleation layers.

Lastly, we investigated overall ALD reaction mechanism for W deposition on the TiN surfaces based on DFT calculation as well as the detailed dissociative reactions of WF₆. Our calculated results suggest that the overall reactions of the WF₆ on the B-covered TiN surfaces are energetically much more favorable than the one on the TiN surfaces, which means that the high reactivity of WF₆ with the B-covered TiN surface is attributed to the presence of B-covered surface made by B₂H₆ molecule. As a result, an effect of the B₂H₆ flow serves as a catalyst to decompose WF₆ molecule. Two additional reaction processes right after WF₆ bond dissociation, such as W substitution

and BF_3 desorption, were also explored to clearly understand the detailed reactions that can occur by WF_6 flow. At the first additional reaction process, W atoms can be substituted into B site and covered on the TiN surfaces due to the strong bonding nature of W with the TiN surface than B atoms. At the second additional reaction process, remaining atoms, such as B and F, can be easily desorbed as by-product, that is, BF_3 because BF_3 desorption is energetically favorable reaction with low activation energy. Furthermore, we also investigated the effect of H_2 post-treatment on W-covered TiN surface in order to remove residual F adatoms, which are known to cause severe problems that extremely degrade characteristics of memory devices. It was found that both H_2 dissociative reaction and HF desorption can occur enough well under somewhat high temperature and H_2 ambience, which is confirmed by the our DFT results and previously reported experimental results. These results imply that the understanding of the role of gas molecules used for W deposition gives us insight into improving the W ALD process for future memory devices.

Key Words:

First-principles study, Atomic layer deposition, Dissociative reaction, Energy barrier, Tungsten, B_2H_6 , WF_6

Student Number: 2014-21439

Contents

Abstract	i
Content	v
List of Tables.....	ix
List of Figures.....	xii
Chapter 1. Introduction	1
1.1. Recent targets for semiconductor industry	1
1.2. Overview of critical 3D NAND processes.....	5
1.2.1. Market and technology drivers for 3D NAND.....	5
1.2.2. Critical 3D NAND processes	6
1.2.3. Film deposition.....	8
1.2.4. High aspect ratio etch/deposition	10
1.3. History and future outlook of ALD	12
1.4. Comparison of CVD and ALD.....	16
1.5. Overview of reaction mechanism for various materials by ALD simulation ...	22
1.5.1. Modeling the ALD of oxide materials: HfO₂.....	23
1.5.2. Modeling the ALD of Si-based materials: SiO₂ & SiN_x	28
1.5.3. Modeling the ALD of metals: Cu	34
1.6. Literature survey of previous researches for W ALD	39
1.7. Technical issues of word-line W in VNAND	45
1.8. Objective of the thesis.....	48
1.9. Bibliography	50

Chapter 2. Theoretical background	57
2.1. Density Functional theory	57
2.1.1. The Many-Body Problem.....	57
2.1.2. The Hohenberg-Khon theorems.....	58
2.1.3. The Kohn-Sham equation	60
2.2. Approximation of exchange-correlation energy	62
2.4. Van der Waals (vdW) force.....	62
2.5. Bader Charge.....	65
2.6. Bibliography	67
Chapter 3. Dissociative reaction of B₂H₆ on TiN surfaces during atomic layer deposition	69
3.1. Introduction	69
3.2. Computational methods.....	73
3.3. Results and discussion	80
3.3.1. Dissociative reaction of B ₂ H ₆ on TiN(001) surface.....	80
3.3.2. Dissociative reaction of B ₂ H ₆ on Ti-terminated TiN(111) surface.....	85
3.3.3. Dissociative reaction of B ₂ H ₆ on Ti-terminated TiN(111) surface.....	90
3.3.4. Discussion	95
3.4. Summary.....	99
3.5. Bibliography	100
Chapter 4. Effects of H₂ and N₂ treatment for B₂H₆ dosing process on TiN surfaces during atomic layer deposition	104
4.1. Introduction	104

4.2. Computational methods.....	109
4.3. Results and discussion	119
4.3.1. Dissociative reaction of H ₂ and N ₂ on TiN(001) surface.....	119
4.3.2. Dissociative reaction of H ₂ and N ₂ on Ti-terminated TiN(111) surface	121
4.3.3. Dissociative reaction of H ₂ and N ₂ on N-terminated TiN(111) surface	124
4.3.4. Effect of N ₂ treatment on TiN surfaces during ALD process.....	128
4.3.5. Dissociative reaction of B ₂ H ₆ on H-covered Ti-terminated TiN(111) surface.....	129
4.3.6. Dissociative reaction of B ₂ H ₆ on H-covered N-terminated TiN(111) surface.....	136
4.3.7. Discussion	142
4.4. Summary.....	149
4.5. Bibliography	150

Chapter 5. Overall reaction mechanism for the early stages of

W ALD on TiN surfaces	156
5.1. Introduction	156
5.2. Computational methods.....	161
5.3. Results and discussion	167
5.3.1. Analysis of charge density distribution for prediction of the surface reactivity of WF ₆ precursor	167
5.3.2. Dissociative reaction of WF ₆ on N-terminated TiN(111) surface	175
5.3.3. Dissociative reaction of WF ₆ on B-covered N-terminated TiN(111) surface.....	181
5.3.4. Two additional reaction processes right after WF ₆ bond dissociation;	

W substitution into B atom, BF₃ desorption	186
5.3.5. H₂ post-treatment for removal of F adatoms	191
5.3.6. Proposed overall ALD reaction mechanism for W deposition	196
5.4. Future work	199
5.5. Summary	204
5.6. Bibliography	205
Chapter 6. Conclusions	209
국문초록	212
List of Publications	214

List of Tables

Table 3.1. The adsorption energies of B_2H_6 calculated on the TiN (001) surface for each orientation and position.	77
Table 3.2. The adsorption energies of B_2H_6 calculated on the Ti-terminated TiN (111) surface for each orientation and position.	78
Table 3.3. The adsorption energies of B_2H_6 calculated on the N-terminated TiN (111) surface for each orientation and position.	79
Table 3.4. Activation energies (E_a , eV) and reaction energies (E_{rxn} , eV) of B_2H_6 dissociation on the TiN (001) surface.	84
Table 3.5. Activation energies (E_a , eV) and reaction energies (E_{rxn} , eV) of B_2H_6 dissociation on the Ti-terminated TiN (111) surface.	89
Table 3.6. Activation energies (E_a , eV) and reaction energies (E_{rxn} , eV) of B_2H_6 dissociation on the N-terminated TiN (111) surface.	94
Table 4.1. The adsorption energies of H_2 and N_2 calculated on the TiN (001) surface for each orientation and position.	114
Table 4.2. The adsorption energies of H_2 and N_2 calculated on the Ti-terminated TiN (111) surface for each orientation and position.	115
Table 4.3. The adsorption energies of H_2 and N_2 calculated on the N-terminated TiN (111) surface for each orientation and position.	116
Table 4.4. The adsorption energies of B_2H_6 calculated on the H-covered Ti-terminated TiN (111) surface for each orientation and position.	117
Table 4.5. The adsorption energies of B_2H_6 calculated on the H-covered N-terminated TiN (111) surface for each orientation and position.	118
Table 4.6. Activation energies (E_a , eV) and reaction energies (E_{rxn} , eV) of	

B ₂ H ₆ dissociation on the Ti-terminated TiN (111) surface.	123
Table 4.7. Comparison of minimum and maximum activation energies ($E_{a, \text{minimum}}$, $E_{a, \text{maximum}}$, eV) and overall reaction energies ($E_{\text{rxn, overall}}$, eV) of B ₂ H ₆ bond dissociation on the H-covered TiN and the TiN surfaces.	131
Table 4.8. Activation energies (E_a , eV) and reaction energies (E_{rxn} , eV) of B ₂ H ₆ dissociation on the H-covered Ti-terminated TiN (111) surface.	135
Table 4.9. Activation energies (E_a , eV) and reaction energies (E_{rxn} , eV) of B ₂ H ₆ dissociation on the H-covered N-terminated TiN (111) surface.	141
Table 4.10. Comparison of minimum and maximum activation energies ($E_{a, \text{minimum}}$, $E_{a, \text{maximum}}$, eV) and overall reaction energies ($E_{\text{rxn, overall}}$, eV) of B ₂ H ₆ dissociation for path a, b, and c on the H-covered Ti-terminated TiN surfaces.	145
Table 4.11. Comparison of minimum and maximum activation energies ($E_{a, \text{minimum}}$, $E_{a, \text{maximum}}$, eV) and overall reaction energies ($E_{\text{rxn, overall}}$, eV) of B ₂ H ₆ dissociation for path a, b, and c on the H-covered N-terminated TiN surfaces.	146
Table 5.1. The adsorption energies of WF ₆ calculated on the N-terminated TiN (111) surface for each orientation and position.	164
Table 5.2. The adsorption energies of WF ₆ calculated on the B-covered N-terminated TiN (111) surface for each orientation and position.	166
Table 5.3. Bond lengths (Å) and amount of charge transfer (e) of the optimized structures for N-terminated TiN (111), B-covered N-terminated TiN (111), and WF ₆ molecule.	174
Table 5.4. Calculated energy diagram of B ₂ H ₆ decomposition on the Ti-terminated TiN (111) surface.	180
Table 5.5. Activation energies (E_a , eV) and reaction energies (E_{rxn} , eV) of	

WF ₆ bond dissociation on the B-covered N-terminated TiN (111) surface..	185
Table 5.6. Activation energies (E _a , eV) and reaction energies (E _{rxn} , eV) of B-F bond recombination on the W-covered N-terminated TiN (111) surface..	190
Table 5.7. Activation energies (E _a , eV) and reaction energies (E _{rxn} , eV) of H ₂ bond dissociation and HF desorption on the W-covered N-terminated TiN (111) surface.	194

List of Figures

Figure 1.1. Graph showing Moore's Law for various electronic technologies.	2
Figure 1.2. Technology roadmap of logic devices reported by Intel in 2013.	4
Figure 1.3. 3D NAND architecture showing some of the most challenging and critical deposition and etch processes.	7
Figure 1.4. As the number of layers increases in the 3D NAND, the effect of film stress can become magnified.	9
Figure 1.5. Transport limitation can lead to distortion (bowing and twisting), CD variation, and incomplete etch during channel formation.	11
Figure 1.6. Number of articles on the topics of DFT studies on ALD published per year (orange) as well as articles on both ALD and ALE published per year (black).	14
Figure 1.7. Overview of elements used for ALD materials.	15
Figure 1.8. Schematic representation of the titania deposition process in ALD and low temperature high-vacuum chemical vapor deposition (HV-CVD). (a) In ALD a substrate is exposed sequentially to a precursor and a reactive partner while the substrate is kept below the pyrolytic decomposition threshold. A parallel exposure without reaction between the precursor and reactive partner in the gas phase is only possible if high vacuum environment is used as shown in (b). Under these conditions the growth occurs simultaneously and continuously, and higher growth rates are achievable. ...	20
Figure 1.9. ALD saturation curve (left) vs CVD growth curve (right).	21

Figure 1.10. Snapshots are from ab initio MD calculation, starting at $T = 500$ K and running for 0.4 ps. (a) First half reaction of HfO_2 ALD. (b) second half reaction of HfO_2 ALD.27

Figure 1.11. Highlighted figures were organized. (a) Deposition rate versus exposure of SiO_2 (red diamonds) and Si_3N_4 (green circles) films deposited from chloro-silane precursors by ALD at 450°C with less than 2% absolute variation on per cycle deposition rate. (b) Proposed mechanistic steps for reactive chemisorption of SiH_2X_2 precursor and desorption of functional group X via proton transfer from a $\text{Si}-\text{Y}-\text{H}$ functionalized surface ($\text{Y} = \text{O}, \text{NH},$ or N). Structure 1 depicts the initial unbound reactants (UR) step; structure 2, the bound reactants (BR); structure 3, the transition state (TS); structure 4, the bound product (BP) step and structure 5, the final unbound products (UP). (c) BP86/SV(P) optimized geometries of bound reactants, transition state, and bound products structures for SiH_2DMA_232

Figure 1.12. Highlighted figures were organized. (a) First half of the reaction cycle of Cu ALD for the $\text{Cu}(\text{dmap})_2$ pulse. Reactant/product states are in black, and activation energies are in red (b) Adsorption (step A) and decomposition (step B) of $\text{Cu}(\text{dmap})_2$ on one (6×6) cell of the $\text{Cu}(111)$ surface. (c) Reaction energy diagram for the second half reaction cycle of the Cu ALD process when Et_2Zn is admitted. (d) By-product formation (step G) and desorption (step H). G1 which is obtained from F1, F2, and F3 configurations, shows the formation of $\text{Zn}(\text{dmap})_2$38

Figure 1.13. Highlighted figures were organized. (a) SIMS profile of fluorine in ALD W (b) TEM images of ALD W for sample A(left), B(center), and C(right).43

Figure 1.14. Highlighted figures were organized. (a) SIMS profile of fluorine in ALD W (b) XRD spectra in ALD W (c) SEM images of gap filling capability in ALD W.	44
Figure 1.15. a) Cross-section of Samsung 32-layer VNAND (b) Plan-view of Samsung 32-layer VNAND (c) two technical issues for voids and F attack.	47
Figure 1.16. Schematics of our research goals.	49
Figure 3.1. (a) TEM micrograph and selected area electron diffraction of a TiN film grown at 250 °C on Si/SiO ₂ wafer. (b) X-ray diffractograms of polycrystalline TiN thin films grown either by thermal (a) or plasma-enhanced (b) ALD at T=250 and 200 °C, respectively (N=500 cycles). The vertical red lines indicate the TiN reference diffraction angle.	72
Figure 3.2. Slab model of (a) TiN(001) (b) Ti-terminated TiN(111) (c) N-terminated TiN(111) surfaces.	76
Figure 3.3. Three orientations and three positions of B ₂ H ₆ on the TiN (001) surface.	77
Figure 3.4. Three orientations and three positions of B ₂ H ₆ on the Ti-terminated TiN (111) surface.	78
Figure 3.5. Three orientations and three positions of B ₂ H ₆ on the N-terminated TiN (111) surface.	79
Figure 3.6. The optimized structures for (a) adsorption state, (b) transition state and (c) reaction state of a B ₂ H ₆ on the TiN (001) surface.	82
Figure 3.7. Calculated energy diagram of B ₂ H ₆ decomposition on the TiN (001) surface.	83
Figure 3.8. Calculated energy diagram of B ₂ H ₆ decomposition on the TiN (001) surface.	84

Figure 3.9. The optimized structures for (a) adsorption state, (b) transition state and (c) reaction state of a B ₂ H ₆ on the Ti-terminated TiN (111) surface.	87
Figure 3.10. Calculated energy diagram of B ₂ H ₆ decomposition on the Ti-terminated TiN (111) surface.	88
Figure 3.11. Initial (IS), transition (TS), and final (FS) states of intermediate reactions from the 2nd reaction step to the 4th reaction step for the Ti-terminated TiN (111) surface.	89
Figure 3.12. The optimized structures for (a) adsorption state, (b) transition state and (c) reaction state of a B ₂ H ₆ on the N-terminated TiN (111) surface.	92
Figure 3.13. Calculated energy diagram of B ₂ H ₆ decomposition on the N-terminated TiN (111) surface.	93
Figure 3.14. Calculated energy diagram of B ₂ H ₆ decomposition on the N-terminated TiN (111) surface.	94
Figure 3.15. (a) Illustrations for modeling of atomic configurations of TiN(002) and TiN(111) (b) XRD patterns and cross-sectional SEM images of CVD TiN films.	97
Figure 3.16. (a) XRD patterns of Al ₂ O ₃ films (b) surface SEM images of Al ₂ O ₃ films.	98
Figure 4.1. Schematic of W ALD deposition process.	108
Figure 4.2. Two orientations and three positions of H ₂ and N ₂ on the TiN (001) surface. The yellow, blue, and pink spheres represent Ti, N, and H atoms, respectively.	114
Figure 4.3. Two orientations and three positions of H ₂ and N ₂ on the Ti-terminated TiN (111) surface.	115

Figure 4.4. Two orientations and three positions of H ₂ and N ₂ on the N-terminated TiN (111) surface.	116
Figure 4.5. Three orientations and three positions of B ₂ H ₆ on the H-covered Ti-terminated TiN (111) surface.	117
Figure 4.6. Three orientations and three positions of B ₂ H ₆ on the H-covered N-terminated TiN (111) surface.	118
Figure 4.7. The optimized structures for (a) adsorption state, (b) transition state and (c) reaction state of a B ₂ H ₆ on the TiN (001) surface.	120
Figure 4.8. The optimized structures for (a) adsorption state, (b) transition state and (c) reaction state of a B ₂ H ₆ on the Ti-terminated TiN (111) surface.	123
Figure 4.9. The optimized initial, transition, final structures of the dissociative chemisorption step for (a) H ₂ and (b) N ₂ on the N-terminated TiN (111) surface.	126
Figure 4.10. Calculated energy diagram(upper) of H ₂ and N ₂ decomposition on the TiN (001), the Ti-terminated TiN (111), and N-terminated TiN (111) surface. First half reaction for TiN (001) surface(below) is drawn.	127
Figure 4.11. Dissociative chemisorption of B ₂ H ₆ on the H-covered Ti-terminated TiN (111) surface: (a) the first reaction step (b) the second reaction step.	132
Figure 4.12. Calculated energy diagram of B ₂ H ₆ decomposition on the H-covered N-terminated TiN (111) surface.	133
Figure 4.13. Initial (IS), transition (TS), and final (FS) states of intermediate reactions from the 3rd reaction step to the 7th reaction step on the H-covered Ti-terminated TiN (111) surface.	134

Figure 4.14. Dissociative chemisorption of B_2H_6 on the H-covered Ti-terminated TiN (111) surface: (a) the first reaction step (b) the second reaction step.	138
Figure 4.15. Calculated energy diagram of B_2H_6 decomposition on the H-covered N-terminated TiN (111) surface.	139
Figure 4.16. Initial (IS), transition (TS), and final (FS) states of intermediate reactions from the 3rd reaction step to the 7th reaction step on the H-covered N-terminated TiN (111) surface.	140
Figure 4.17. Calculated overall energy diagram of B_2H_6 decomposition for path a, b, and c on the H-covered Ti-terminated TiN (111) surface.	145
Figure 4.18. Calculated overall energy diagram of B_2H_6 decomposition for path a, b, and c on the H-covered N-terminated TiN (111) surface.	146
Figure 4.19. (a) Passivated SiO_2 against W nucleation by adding H_2 (b) XPS and SEM for nucleated W on SiO_2	147
Figure 4.20. Proposed W ALD process.	148
Figure 5.1. W ALD deposition condition and motivation of this study.	160
Figure 5.2. Two geometries and three positions of WF_6 on the N-terminated TiN (111) surface.	164
Figure 5.3. Two geometries and thirteen positions of WF_6 on the B-covered N-terminated TiN (111) surface.	165
Figure 5.4. Description of Lewis Acid-Base Reaction.	170
Figure 5.5. 3D electron density distribution of the optimized structure of the WF_6 precursor. Charge depletion around the W atom with electron loss of 5.34e and accumulation (pink area) in the vicinity of the F atom with electron gain of -0.98e can be seen.	171

Figure 5.6. The optimized structure of the N-terminated TiN (111) surface: (a) 3D electron density of top and side views at 0.025 \AA^{-3} isosur-face. Charge depletion around the Ti atom with electron loss of 2.43e and accumulation (pink area) in the vicinity of the N atoms with electron gain of -1.55e can be seen. (b) 2D electron density map for top-layer of the same surface.172

Figure 5.7. The optimized structure of the B-covered N-terminated TiN (111) surface: (a) 3D electron density of top and side views at 0.025 \AA^{-3} isosurface. It shows charge depletion around the Ti atom and B atom with electron loss of 2.19e and 2.21e, respectively. Charge accumulation (pink area) in the vicinity of the N atoms with electron gain of -2.99e can be seen. (b) 2D electron density map for top-layer of the same surface.173

Figure 5.8. The optimized initial, transition, final structures for the first dissociative reaction step of WF_6 on the N-terminated TiN (111) surface..177

Figure 5.9. Calculated energy diagram of WF_6 decomposition on the N-terminated TiN (111) surface.178

Figure 5.10. Calculated energy diagram of B_2H_6 decomposition on the Ti-terminated TiN (111) surface.179

Figure 5.11. The optimized initial, transition, final structures for the first dissociative reaction step of WF_6 on the B-covered N-terminated TiN (111) surface.183

Figure 5.12. ALD Calculated energy diagram of WF_6 decomposition on the B-covered N-terminated TiN (111) surface.184

Figure 5.13. Initial (IS), transition (TS), and final (FS) states of intermediate reactions from 2nd reaction step to the 4th reaction step of WF_6 bond dissociation on the B-covered N-terminated TiN (111) surface.185

Figure 5.14. W adatom diffusion from atop (IS) to sub-layer (FS): (a) top and side views of W adatom on B-covered N-terminated TiN (111) surfaces. (b) energy profile.	188
Figure 5.15. Calculated energy diagram of BF ₃ desorption on the W-covered N-terminated TiN (111) surface.	189
Figure 5.16. Initial (IS), transition (TS), and final (FS) states of intermediate reactions from 1st reaction step to the 3rd reaction step of BF ₃ desorption on the W-covered N-terminated TiN (111) surface.	190
Figure 5.17. Calculated energy diagram of (a) H ₂ dissociation on the W-covered N-terminated TiN (111) surface and (b) HF desorption on the H-saturated W-covered N-terminated TiN (111) surface.	193
Figure 5.18. Initial (IS), transition (TS), and final (FS) states of H ₂ bond dissociation and HF desorption on the W-covered N-terminated TiN (111) surface.	194
Figure 5.19. Mass spectrometry results of W ALD using SiH ₄ /(WF ₆ +H ₂) and SiH ₄ /WF ₆	195
Figure 5.20. Proposed overall ALD reaction mechanism for W deposition.	198
Figure 5.21. DFT optimized various metal precursors and DFT calculated energies of hydrolysis in gas phase for various metal precursors.	202
Figure 5.22. Surface saturation algorithm Al ₂ O ₃ dep. on Al ₂ O ₃ surface (upper left) and TMA reaction pathways confirmed by DFT (upper right), Similarity of growth rate between MD simulation and experiments (lower).	203

Chapter 1. Introduction

1.1. Recent targets for semiconductor industry

Gordon E. Moore, in a landmark 1965 paper, reported that the density of transistors on an integrated circuit (IC) doubles approximately every two years and that with this comes increased performance and lower cost. Since the size of a fully operational IC is reduced, this proposal as shown in **Figure 1.1** is known as “Moore’s Law”[1]. Scientists have created amazing tools that are still emerging to solve the ever exponentially increasing problems. There is a constant demand for new materials to be formed, which can be deposited at nanometer scale. These materials should be deposited in 3D to keep up with the aforesaid law.

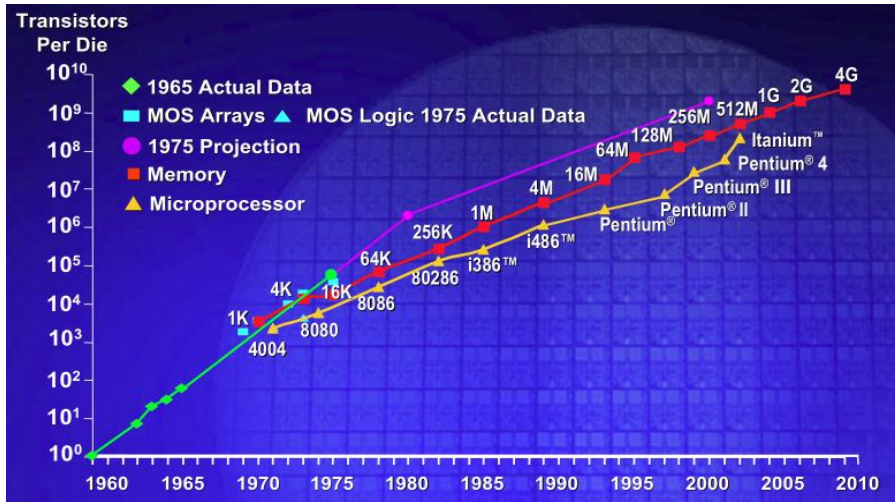


Figure 1.1. Graph showing Moore's Law for various electronic technologies.

(Source of the picture - Intel)[2]

Back in the '80s and '90s, it used to be a seriously noteworthy advance when Intel or IBM or TMSM announced that they'd successfully crossed yet another nanometer threshold and moved their CMOS chip fab process down the micron ladder. In 1985, 1 micron was the state of the art, and was used by the Intel 80386 processor. By 2004, the micron scale had been abandoned and 90nm processors like the Winchester AMD 64 and Prescott Pentium 4 were the norm.

Things have slowed down considerably since the heady days of 0.8, 0.6, and 0.35 micron, though. Most current digital devices use processors, sensors, and memory chips based on 45 and 60nm processes because very few silicon foundries have managed to make the jump to 32nm, let alone 22nm as shown in **Figure 1.2**. The fact is, the standard process of arranging components on a silicon wafer using a top-down, layer-by-layer approach, has hit a wall. Even atomic layer deposition, the process that will take us to 22nm, 16-and-14nm, and introduce FinFET "3D" transistors, can go no further.[3]

The thing is, atoms are very, very small, but they still have a finite size. A hydrogen atom, for example, is about 0.1 nanometers, and a caesium atom is around 0.3nm. The atoms used in silicon chip fabrication are around 0.2nm. In the case of the 22nm chips, the high- κ dielectric layer is just 0.5nm thick; just two or three atoms.

1.2. Overview of critical 3D NAND processes

Since its introduction several years ago, 3D NAND has become a mainstream technology because of its ability to increase bit density in memory devices. Its adoption has been accelerated by advances in the underlying manufacturing processes that are enabling 3D architectures and lowering the cost per bit. With all its advantages, however, the overall complexity and capital intensity of 3D NAND manufacturing add significantly to the challenges fabs are facing in terms of process control, yield, and economics. [4]

1.2.1. Market and technology drivers for 3D NAND

The main impetus for 3D NAND was the recognition that planar technology was approaching the end of its physical limits to deliver higher densities and a lower cost-per-bit. Past advances in conventional planar NAND technology have primarily been driven by physical scaling, where lithography capabilities determined just how many memory cells could fit within a given die size. Using multiple levels of charge within each cell by going from single- to multi-level cell designs has also enabled increased bit densities. However, these improvements typically have come at the expense of speed because of the need to differentiate between the multiple levels of charge. In addition, since the individual memory cells for these designs lie in a horizontal plane, scaling is still ultimately limited by lithography. Other

challenges in scaling 2D NAND beyond the 15 nm node include cell-to-cell interference, unscalable dielectrics, and electron leakage [5].

To address these challenges, 3D NAND fundamentally changes the scaling paradigm. Instead of traditional X-Y scaling in a horizontal plane, 3D NAND scales in the Z-direction by stacking multiple layers of NAND gates vertically. This allows more cells to be packed into the same X-Y space (planar area) on the die without shrinking dimensions horizontally. By easing cell size requirements, triple- and even quadruple-level cell designs are possible. As such, 3D NAND offers a significant increase in bit density over planar NAND.

Unlike planar NAND, where scaling is primarily driven by lithography, 3D NAND scaling is enabled by advances in deposition and etch processes. An incredible level of precision and repetition is required in defining complex 3D structures with extremely high aspect ratio (HAR) features. Achieving success with 3D NAND requires innovative deposition and etch solutions that minimize variability.

1.2.2. Critical 3D NAND processes

The 3D NAND architecture requires advanced capabilities enabling HAR and complex structures in **Figure 1.3**. Critical processes involved include multilayer stack deposition, HAR channel etch, wordline metallization, staircase etch, HAR slit etch, and stair contacts formation. The following sections look at some of these areas in more depth and describe the most critical process parameters that must be controlled.

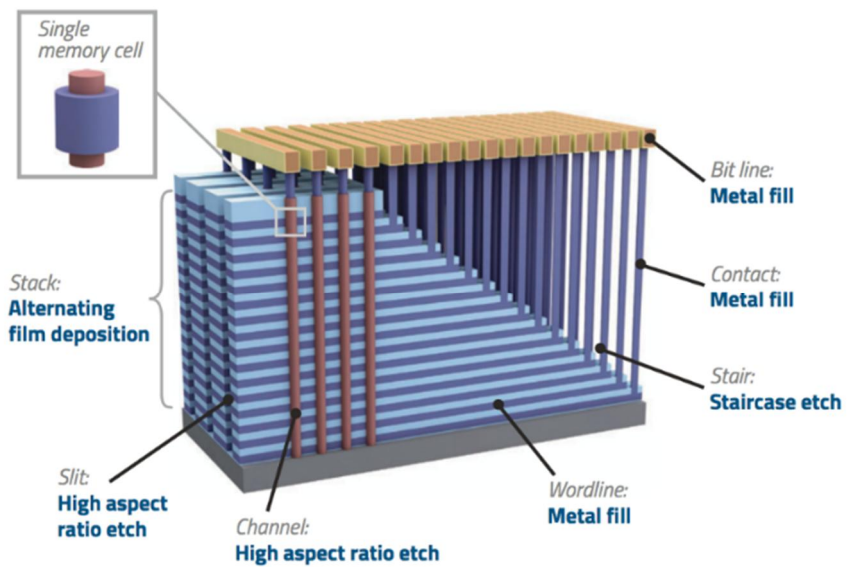


Figure 1.3. 3D NAND architecture showing some of the most challenging and critical deposition and etch processes.[4]

1.2.3. Film deposition

Creating stacked memory cells starts with depositing alternating layers of thin films. Unlike planar NAND, where cell pitch is defined by lithography, pitch in 3D NAND is determined by the film thickness. As such, precise control of layer-to-layer deposition uniformity is extremely important. Currently, commercial 3D NAND products in high-volume manufacturing have layers ranging from 32 to 48 pairs, while next-generation products with more than 60 pairs are now beginning high-volume ramps.

Critical requirements for depositing stacked films are the stress and uniformity of the individual layers within the overall stack. These requirements become more stringent and increasingly more challenging to meet as the number of layers grows. Wafer bow and local film stress in **Figure 1.4** directly impact the ability to achieve precise lithography overlay. Film thickness and repeatability affects the active area of cell and consistency of the litho/etch performance. As a result, both film stress control and excellent uniformity are critical to wafer yields. To address these concerns, careful management of stress by tuning deposition conditions and optimizing integration is needed not only for the film stack deposition, but also throughout 3D NAND manufacturing.

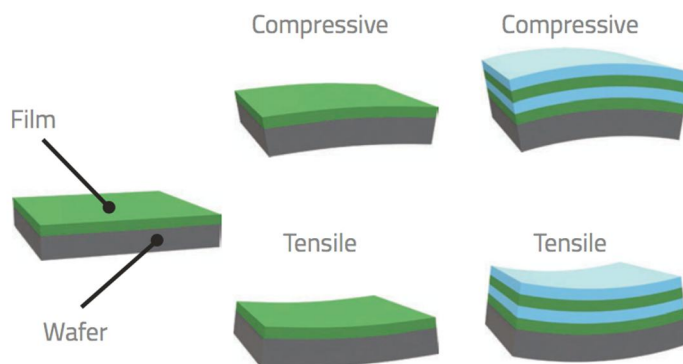


Figure 1.4. As the number of layers increases in the 3D NAND, the effect of film stress can become magnified.[4]

1.2.4. High aspect ratio etch/deposition

Deep etch on these multilayer stacks can push the limits of physics to achieve uniformity from top to bottom. As shown in **Figure 1.5**, the high aspect ratio of this etch leads to transport limitation challenges that can generate a range of problems. These include incomplete etch wherein some holes don't reach the bottom, bowing, twisting, and CD variation between the top and bottom of the stack. Such defects can lead to shorts, interference between neighboring memory strings, and other performance issues. Solving these HAR-related transport issues requires precise control of high-energy ions during the etch process. Technologies that help deliver this capability include a symmetric chamber design for intrinsic uniformity, a proprietary high ion energy source with advanced plasma confinement and modulation, and orthogonal (independent) uniformity tuning knobs, such as multi-zone gas delivery and temperature control to achieve required uniformity across the wafer. As the 3D NAND roadmap adds more layers to achieve higher bit density, channel hole etching becomes increasingly challenging due to higher aspect ratios. Managing the fundamental trade-offs among profile, selectivity, and CD requires continuous equipment innovation, not only to deliver HAR etching capabilities for more than 100 pairs, but also to do this at the productivity needed for volume manufacturing.

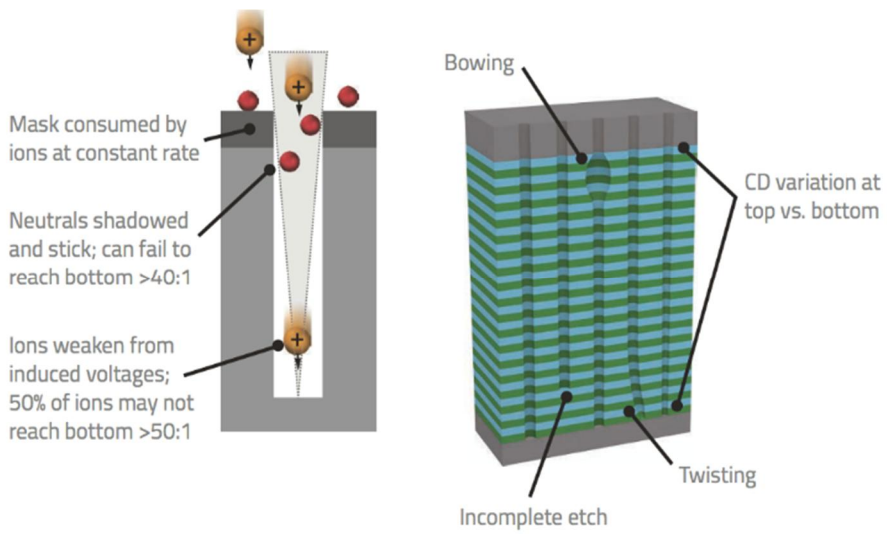


Figure 1.5. Transport limitation can lead to distortion (bowing and twisting), CD variation, and incomplete etch during channel formation.[4]

1.3. History and future outlook of ALD

The atomic layer deposition has been invented independently twice by two groups in neighbouring countries. The ALD principle of alternate self-limiting surface reactions was first documented by professor Aleskovskii and his group in Soviet Union in the 1960s. Inorganic materials were deposited using molecular precursors and the process was dubbed "molecular layering". A similar process was developed in Finland in the 1970s by Dr. Tuomo Suntola and his co-workers[6] dubbed "atomic layer epitaxy" (ALE). The Soviet-Russian origins were not known even to Suntola himself until the 1990s. The Finnish origin of ALD has since become widely known as the development of ALE lead to applications in thin film electroluminescent flat panel displays in the 1980s. [7-9]

Dr. Suntola was awarded the Millennium Technology Prize for the development of ALD in 2018.[10] Over time the process was titled atomic layer depositions, since the growth of the thin film was not necessarily epitaxial. The first ALD-conference was held in Finland in the 1984 and the first international conference, also in Finland, in 1990.

Interest in ALD has increased exponentially over the years as shown in **Figure 1.6**. The number of scientific articles published remained steady through the 1990s but started to grow rapidly after the change of the millennium. Similarly, the theoretical modelling of ALD has seen an increase over the years. However, the roots of theoretical modelling of ALD extend back to the beginning of ALD itself. Theoretical quantum chemical inves-

tigations of zinc sulphide were already presented in the first symposium on atomic layer epitaxy in 1984 by Tapani Pakkanen [11].

ALD has become a prominent method in thin film deposition and has great prospects for the future. The set of possible materials that can be deposited is large and expanding[12] and different special techniques based on the ALD procedure, such as atomic layer etching[13] and area selective ALD[14], are gaining interest. The available materials for ALD have been greatly expanded in the recent years. To date, more than 1000 ALD processors[15] have been explored including almost the whole periodic table, i.e. oxides, nitrides, sulfides, and metals (**Figure 1.7**). In addition, newly surged materials such as gold[16] had been exemplified by ALD, which is not included in this table. These studies have greatly promoted the development of ALD technology and nanomaterials, as well as its applications.

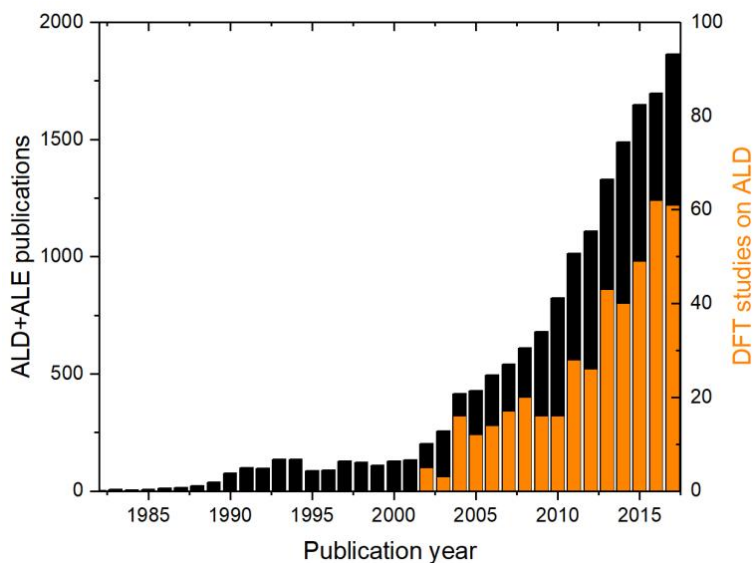


Figure 1.6. Number of articles on the topics of DFT studies on ALD published per year (orange) as well as articles on both ALD and ALE published per year (black). Source: Web of Science, accessed on January 30, 2018

ALD thin film materials

H																	He	
Li [*]	Be [*]											B [*]	C [*]	N [*]	O [*]	F [*]	Ne	
Na	Mg [*]											Al [*]	Si [*]	P [*]	S [*]	Cl	Ar	
K	Ca [*]	Sc [*]	Ti [*]	V [*]	Cr [*]	Mn [*]	Fe [*]	Co [*]	Ni [*]	Cu [*]	Zn [*]	Ga [*]	Ge [*]	As [*]	Se [*]	Br	Kr	
Rb	Sr [*]	Y [*]	Zr [*]	Nb [*]	Mo [*]	Tc	Ru [*]	Rh [*]	Pd [*]	Ag [*]	Cd [*]	In [*]	Sn [*]	Sb [*]	Te	I	Xe	
Cs	Ba [*]	La [*]	Hf [*]	Ta [*]	W [*]	Re	Os [*]	Ir [*]	Pt [*]	Au [*]	Hg [*]	Tl [*]	Pb [*]	Bi [*]	Po	At	Rn	
Fr	Ra	Lr	Rf	Db	Sg	Bh	Hs	Mt										
			Ce [*]	Pr [*]	Nd [*]	Pm	Sm [*]	Eu [*]	Gd [*]	Tb [*]	Dy [*]	Ho [*]	Er [*]	Tm [*]	Yb [*]	Lu [*]		
			Th	Pa	U	Np	Pu	Am	Cm	Bk	Cf	Es	Fm	Md	No	Lw		

- ★ Oxide
- Nitride
- ◆ Phosphide/Arsenide
- ▲ Sulfide/Selenide/Telluride
- Element
- ▼ Carbide
- ⊙ Fluoride
- ⊕ Silicide

Figure 1.7. Overview of elements used for ALD materials. [17]

1.4. Comparison of CVD and ALD

Chemical vapor deposition (CVD) is a mature technique for the deposition of high quality films for various applications.[18, 19]

Most CVD processes rely on the pyrolytic decomposition of precursors on the surface after adsorption. If no additional energy is applied (like in plasma CVD), the pyrolytic decomposition of the precursor results in the generation of new surface adsorption sites and enables thereby a continuous growth of the desired thin film. The substrate temperature is chosen to be above the pyrolytic decomposition threshold of the precursor to enable continuous film growth.

ALD represents one of the most popular subtypes of CVD.[12, 20, 21] In contrast to thermal CVD, low substrate temperatures are applied in ALD to avoid thermal decomposition of the precursor. Consequently, the precursor molecules do not decompose completely after chemisorption and the reaction stops as soon as no reactive surface site is accessible anymore. In order to complete the deposition process and trigger the next chemical reaction between unreacted ligands of the precursor with a reactive partner, either another precursor or a reactive gas such as H_2O , O_2 , etc. is added into the system which reacts with the adsorbed species in order to ultimately form the desired material.[22]

Due to the high reactivity between precursor and reactive partner even in the gas phase, both of them have to be separated either locally or temporally in order to prevent molecular collisions in the reactor, which would lead to undesired gas phase reaction, nucleation, particle growth, and powder formation. Such a separation is challenging in conventional CVD systems,

where usually less reactive precursor combinations but higher substrate temperatures are employed. In ALD, the formation of the thin film is realized stepwise as shown in **Figure 1.8(a)**: the substrate is exposed sequentially with the precursor and reactive partner, separated by a purging of the reactor. This temporal separation excludes gas phase interactions of the reactive partners and enables the precise control of film thickness and the high conformality, i.e., shape independent film growth rate, of ALD processes. However, it also ultimately limits the growth rate of the thin films.

We describe an alternative approach to separate the two reactive partners during the deposition process. As depicted in **Figure 1.8(b)**, we simultaneously expose the substrate with the precursor/reactive partner pair and avoid gas phase reactions by performing all experiments in a high vacuum environment (10^{-6} hPa).

A comparable approach has been described already by Terasako et al.[23] They report the deposition of zinc oxide from diethyl zinc and water, a chemistry that has been successfully employed in ALD.[24] The aim of their work was to increase crystallinity of the obtained films grown at elevated substrate temperatures in standard HV-CVD conditions, i.e., where the process is mainly driven by pyrolytic decomposition of the adsorbed precursor.[25] We, however, use substrate temperatures below the pyrolytic decomposition threshold of the utilized precursor to ensure that only the chemical reaction potential between two reactive partners drive the process on the surface.

Keeping high vacuum during the deposition process offers additionally numerous advantages over standard CVD and ALD processes. In the high

vacuum environment, the free mean path of the molecules is larger than their trajectory between the precursor source and the substrate. This ballistic nature of the precursor transport allows precise prediction and engineering of tailored impinging rates even on large surface areas based exclusively on (analytic) geometric modeling.[26] Depending on the source geometry it is possible to realize either highly uniform depositions or impinging rate gradients independently for all used precursors.

In ALD, a precursor adsorbs onto the active surface sites on the target substrate. Once all of the active sites are occupied, excess precursor molecules are purged out of the reaction chamber[7]. If the precursor is thermally stable at the deposition temperature, no further film growth reactions occur (**Figure 1.9**). The ALD reactions are self-limiting when it is operating ideally.

Many of the unique advantages of the ALD are due to control of layer thickness at the Ångstrom level. The self-limiting nature of the surface reactions also produces nonstatistical deposition because the randomness of the precursor flux is removed as an important factor. In principle, the discrete cycles of ALD can be used to deposit different layers. There have been some reports of this, especially in ZAZ dielectrics[27]. The precursors used in an ALD process should have certain qualities so as to achieve self-limiting growth. These are:

- Volatile - For efficient transportation, a limit of 0.1 Torr at the applicable maximum source temperature. The source should be preferably in liquid or gaseous state[28].
- Stable against Self-Decomposition - The self-limiting film growth via the surface exchange reactions is achievable only under conditions

where the precursors do not decompose on their own[28].

- Undergo Aggressive and Complete Growth Reactions with surface species - Thermodynamically the ALD reactions should be feasible.
- No Side-Reactions - There should not be any alternative reactions as this might lead to impurities.
- No Dissolution to the film or the substrate - The dissolution of the film onto the surface might be harmful. This can be seen in the case of Cu onto the Si surface. The copper brings down the band gap of Si[29].
- Un-reactive byproducts - Reactive byproducts may cause corrosion problems in the reactor or in the exhaust[30].
- Practical Requirements like the ease of synthesis, level of impurities, safe handling and commercial availability also matters.

However, all these requirements cannot be completely fulfilled simultaneously and often the last ones can be sacrificed while developing a new ALD precursor[28].

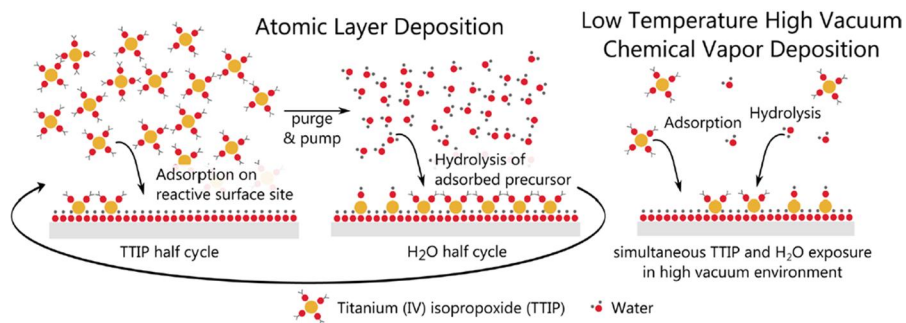


Figure 1.8. Schematic representation of the titania deposition process in ALD and low temperature high-vacuum chemical vapor deposition (HV-CVD). (a) In ALD a substrate is exposed sequentially to a precursor and a reactive partner while the substrate is kept below the pyrolytic decomposition threshold. A parallel exposure without reaction between the precursor and reactive partner in the gas phase is only possible if high vacuum environment is used as shown in (b). Under these conditions the growth occurs simultaneously and continuously, and higher growth rates are achievable.[31]

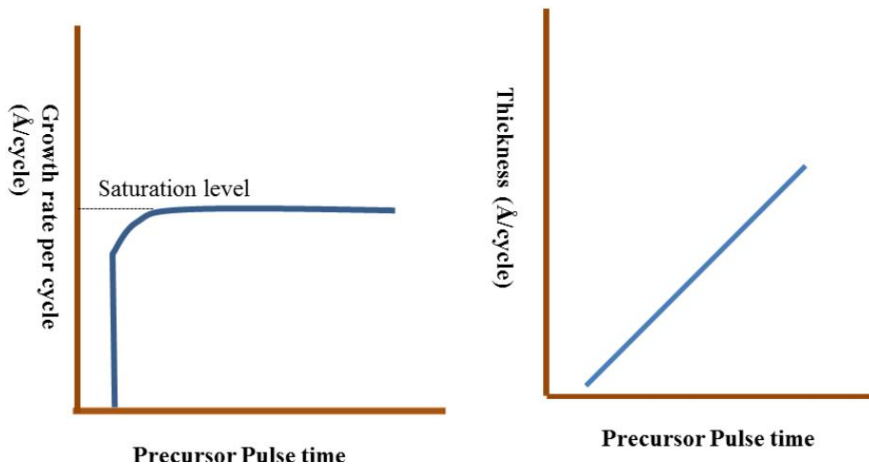


Figure 1.9. ALD saturation curve (left) vs CVD growth curve (right).[32]

1.5. Overview of reaction mechanism for various materials by ALD simulation

To design, analyze or improve an ALD process in a rational way therefore requires knowledge of the underlying chemical mechanism. A remarkable level of detail about the mechanism can be obtained from characterization under typical process conditions in situ to the ALD reactor using techniques such as quadrupole mass spectrometry, quartz crystal microbalance, infrared spectrometry[9], and synchrotron X-ray methods. Atomic-scale modeling using density functional theory (DFT) provides a complementary view, which is the focus of this report.

In principle, the kinetics of every conceivable growth reaction and side reaction for a given system of substrate and reagents should be evaluated and compared. Clearly, this is rarely possible, but fortunately there are shortcuts. Comparing the activation energies of selected key reaction steps may be sufficient to answer specific questions about a process, and this is the approach taken in most of the papers reported below. The common approach for ALD modeling is to use DFT to calculate the pathways for precursor adsorption, ligand migration and by-product formation on the surface, yielding reaction energies and activation energies for each step and indicating whether the reaction is thermodynamically or kinetically favorable at the temperature of interest (if the effect of entropy is included). Surfaces may be modeled using either periodic slabs or finite clusters. Empirical corrections of the van der Waals interactions are included in some studies.[33-35]

An even simpler approach is to compute the overall thermodynamics of the ALD reaction with DFT. Though apparently ignoring kinetics, this can

give valuable insight because, within a class of similar reactions, reactions that are more exothermic also have lower activation energies. In addition, low-temperature ALD processes must be driven forward by favorable energetics ($\Delta E < 0$), whereas high-temperature CVD processes are often driven by entropy ($\Delta S > 0$).

1.5.1. Modeling the ALD of oxide materials: HfO₂

Hafnium oxide (HfO₂) shows a band gap of approximately 6 eV and a high dielectric constant in thin film form of 25 which makes it an important high-k material. In the ongoing miniaturization of electronic devices, nanometer-thin films of hafnium oxide are replacing silicon oxide as the gate insulator in field effect transistors.[36] The hafnium oxide thin films are fabricated using atomic layer deposition (ALD).[7] This section unveils the atomic scale reactions of ALD for hafnium oxide thin films.

In ALD of hafnium oxide, HfCl₄ and water are the most frequently used precursor combination.[37] However, a major difficulty with the HfCl₄ precursor is chlorine contamination in the thin films. The contamination decreases with increasing substrate temperature. However, higher temperature means drop in coverage of reactive OH fragments as H₂O dissociates and consequently drop in growth rate per cycle. Therefore, an alternative precursor chemistry is required that exhibits suitable thermal stability, conformal ALD growth, and low levels of impurities at low temperature. Hafnium alkylamide precursors, like Hf(NEtMe)₄, Hf(NEt₂)₄, and Hf(NMe₂)₄ (Et = C₂H₅, Me = CH₃), are interesting alternatives together

with water leading to smooth and conformal thin films.[38] These precursors operate at relatively low temperature (~ 300 °C). While there is discussion about the stability of alkylamide precursors as a function of temperature, this is out of the scope of this section, where we consider only “ideal” ALD reactions. For such ideal reactions, we expect that the three commonly used amides listed above will behave similarly and so carry out calculations on just one of them, $\text{Hf}(\text{NMe}_2)_4$.

Calculations using a periodic slab are carried out on a HfO_2 surface subjected to $\text{Hf}(\text{NMe}_2)_4$ and H_2O pulses. In this model, the Lewis acid-base reactions of precursor adsorption and byproduct elimination are described. The effect of bridging O, bare O, and OH as adsorption sites are considered. Under-coordinated oxygen is expected to have an important role during densification of precursor fragments. Densification is defined as the increase in density due to improved Hf-O packing, associated with an increase in coordination numbers of Hf and O from their molecular values (4 and 2, respectively) toward bulk solid values (7 and 4).[39] Moreover, H-transfer from sites adjacent to the adsorbed precursor is considered so as to see how those transfers change the reaction path in ALD.

They used DFT slab models to investigate the ALD reactions for growth of HfO_2 from $\text{Hf}(\text{NMe}_2)_4$ and H_2O . They include all steps, from the early stage of adsorption of each ALD precursor to the densification of multiple atoms into bulk-like HfO_2 layers. The resulting reactions, which explain the fundamental chemistry of ALD at low temperatures (below 500 K), are outlined below.

Adsorption. Chemisorption of precursors is only possible at surface sites of sufficient Lewis activity, namely, terminal O and OH for $\text{Hf}(\text{NMe}_2)_4$

and $(\text{Hf}(\text{NMe}_2))_x$ ($x \geq 2$) cluster (e.g., dimers) for H_2O . Saturated surfaces do not have these sites and so resist further adsorption. This explains the self-limiting reactions that distinguish ALD from other techniques.

Multiple Proton Diffusion. We propose the diffusion of multiple protons to the amide ligands of the Hf precursor before desorption of protonated ligands takes place. The activation energy calculations show that repeated proton diffusion from the surface to the amide ligand and rotation of the protonated amine is more energetically accessible than the simple elimination of the amine in the initial stage. Due to multiple proton diffusion to the fragments, the dative bonds between Hf and N are weakened. This reduction in bond strength facilitates the desorption of fragments from the precursor. The resulting activation energies for protonation and desorption of ligands are low enough that these reactions can take place in low temperature ALD. Multiple proton diffusion is seen in all the stages of ligand elimination as shown in **Figure 1.10(a)**.

Densification. Loss of a proton from oxygen frees it up for bonding to Hf of the precursor. Protonation of ligands, and especially desorption of ligands, frees up Hf for bonding to surface oxygen. Decomposition of H_2O at the surface also increases the coordination of Hf and O. These effects are termed “densification”, as they bring Hf-O packing closer to the bulk scenario. Densification is hence accompanied by substantial energy gain, and this can be the driving force that facilitates ligand eliminations at the surface and vacancy filling in subsurface layers. Densification thus accounts for some of the important characteristics of ALD, such as conformal growth.

Saturated Surfaces. During the early stage of the metal pulse, due to the saturation of the surface by remaining fragments HfX , adsorption of

further metal precursor stops. The presence of these fragments prevents further chemisorption of HfX_4 , since this requires the creation of a strong dative bond between Hf and O. A separate effect is depletion of coreagent (protons) at the surface as HX desorbs. Clearly, no further elimination of HX is possible once protons are exhausted. If the surface can store a higher population of coreagent, then a higher growth rate is expected.[40] Next, during the H_2O pulse, Hf exchanges its remaining ligands with OH groups as shown in **Figure 1.10(b)**. The exchange occurs due to the decomposition of adsorbed H_2O molecules in clusters of HfX. Simultaneously, low coordinated oxygen atoms appear at the surface, which are reactive sites for the next metal pulse. With saturation of the surface by OH groups, H_2O molecules begin to appear. These molecules are loosely bonded to the surface and readily desorb, reducing the growth rate, especially at high temperatures.

It can thus be seen that a wide variety of reactions can take place simultaneously on the surface during ALD. Competition between the elimination reactions and proton diffusion reactions at different ALD temperatures and their influence on the conformality of the film are interesting issues that we are currently investigating by incorporating these DFT data into kinetic Monte Carlo modeling.

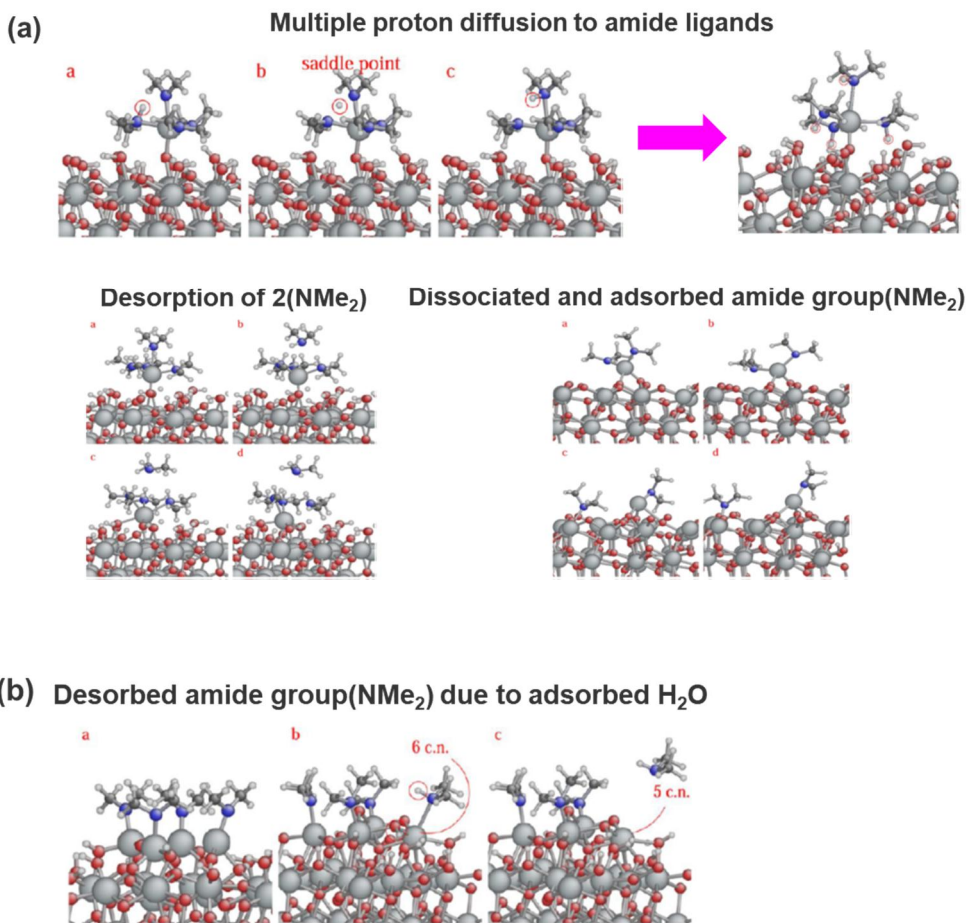


Figure 1.10. Snapshots are from ab initio MD calculation, starting at $T = 500$ K and running for 0.4 ps. (a) First half reaction of HfO₂ ALD. (b) second half reaction of HfO₂ ALD. [41]

1.5.2. Modeling the ALD of Si-based materials: SiO₂ & SiN_x

Si-based materials are very important and widely used in the electronics industry and an overview of theoretical modeling of SiO₂ and Si₃N₄ thin film growth by ALD is given in this section. SiO₂ is the most-frequently used dielectric in electronics. SiO₂ films are chemically inert, scratch resistant, hard and have high optical transmittance.[42] They therefore have many different applications such as sidewall spacers in fin field-effect transistors,[43] hard masks in self-aligned double patterning[44] and gap fill oxides for shallow trench isolation. Amorphous Si₃N₄ thin films are widely used as passivation layers, masking layers to prevent oxidation in underlying materials and as a final protection layer due to their hardness and radiation resistance.[42, 45, 46] There is great interest in developing new ALD processes for SiC and elemental Si itself.

Traditionally, thin films are fabricated using plasma-enhanced CVD or low-pressure CVD. Plasma-enhanced CVD is used to fabricate thin films at low temperature (<400 °C), while low pressure CVD is used to fabricate very conformal films. ALD is the technique that provides both features, depositing highly conformal Si-based thin films at low temperatures on high-aspect ratio structures. Using plasma-enhanced ALD (PEALD) can be a solution for reducing the temperature of the ALD process, albeit sometimes at the cost of poorer conformality.

Of specific interest is the experimental observation that the required silicon precursor exposure is significantly (>100 ×) higher for Si₃N₄ than for SiO₂. **Figure 1.11(a)** compares the relative reactivity for simple chloro-silane

precursors (e.g., DCS, HCDS, etc.), whereas similar data (not shown) has been obtained using amino-silane precursors (e.g., BTBAS, BDEAS, etc.). Precursor exposure was varied by changing the exposure time, the exposure partial pressure, or both. Deposition rate was determined by measurement of the thickness after deposition and dividing by the number of ALD cycles performed. The very long precursor exposure for deposition of silicon nitride makes this process economically unviable, due to both the excessive throughput time per film deposited and the unacceptably high volume of silicon precursors consumed. It is the goal of this work to explain the difference in deposition efficiency for a given exposure between SiO₂ and Si₃N₄ and to examine the effect of different silicon precursor on deposition efficiency.

Choosing the right precursor for an ALD process is one of the crucial steps that determine the viability of the process and the quality of the grown film. The precursor first undergoes dissociative chemisorption on the surface, leaving a Si atom attached to the surface and releasing by-products into the gas phase. Here there is a significant difference to the ALD of metal oxides and nitrides: an energetic barrier towards the breaking of Si-ligand bonds must usually be overcome before Si can form a new bond to the surface and chemisorb in **Figure 1.11(b)**. Ligands may be simultaneously protonated to form by-products. After purging out the Si precursor, the appropriate co-reagent is pulsed into the reactor. H₂O or O₂ plasma is used for SiO₂ in thermal ALD or PEALD respectively. NH₃ or a nitrogen containing plasma (N₂/H₂ or NH₃) is used for thermal ALD or PEALD of Si₃N₄.

Though simple thermodynamic models did correctly predict the

difference in ALD reactivity between silicon oxides and silicon nitrides they were ineffective in predicting the trends in reactivity between individual precursors. Calculations of the reaction pathway using small gas-phase molecules as models for surface groups were vital in developing a reaction mechanism for adsorption of the precursors and highlighted the importance of the orientation of chemical groups to each other. The significance of this difference in approach of the precursors toward the surface groups becomes apparent when reactivity with the larger cluster models is considered. For the OH-covered surface, little interaction is observed between the precursor and surrounding surface, but for the NH₂ covered surface, the side-on approach of the precursor causes the precursor groups to be oriented toward the surface. This has a substantial effect on the strength of the H-bonding between precursor and surface (“bound reactants”) and thus on the lifetime of the adsorbed state and the probability of further reaction before desorption. Their relative adsorption energetics are therefore used to estimate the ALD kinetics and exposure required. With regard to the silicon dioxide surface model, all the amino-silane precursors considered in this work were determined to have reasonably strongly bound reactants (adsorption energies between -32 and -65 kJ/mol) and therefore a reasonable ALD growth rate is predicted. The steric bulk of the amine functional groups attached to the precursors was found to have a greater effect on ALD growth of silicon nitride as shown in **Figure 1.11(c-d)**.

For the precursors where one or more smaller R groups were attached to the amine functional groups (e.g., SiH₂(NH₂)₂, $\Delta E[\text{BR}] = -28.2$ kJ/mol), more stable bound reactants structures were found than those with larger R groups (e.g., BDEAS, $\Delta E[\text{BR}] = -5.9$ kJ/mol). DFT calculations for the

bound reactants of the larger SiH_2DMA_2 and BDEAS precursors yielded the lowest adsorption energies -7.5 and -5.8 kJ/mol. Despite the same number of atoms as BDEAS and a large t-butyl group attached to one position of the amine functional groups, adsorption of BTBAS (-21.4 kJ/mol) was determined to be significantly more exothermic than that of BDEAS (-5.8 kJ/mol). In fact, BTBAS adsorbs as easily as the model precursor $\text{SiH}_2(\text{NH}_2)_2$ (-28.8 kJ/mol), where the presence of the small hydrogen on the amine functional group allows the precursors to form bound reactant structures with reduced steric interactions with the surrounding surface compared to larger alkyl groups.

The mechanism presented in this work for the adsorption of silicon precursors via functional group elimination predicts hydrogen atoms to be present both on the surface and embedded within the growing silicon nitride film. By contrast, the same mechanism predicts that hydrogen is only present on the surface of silicon oxide film. In the experimental FTIR absorption spectra, vibrational bands associated with NH bonds in silicon nitride are indeed detected, in contrast with a lack of OH vibrational bands in silicon oxide. This helps validate the proposed growth mechanism and theoretical approach. Due to the relative unreactivity of NH groups toward functional group elimination, the plasma assisted ALD silicon nitride is much slower compared to that of silicon oxide systems and requires longer precursor exposure. Targeted reduction in precursor bulk may improve the situation, but the main reason is the inflexible orientation of amine groups at the surface, which is an intrinsic property of the silicon nitride material being deposited.

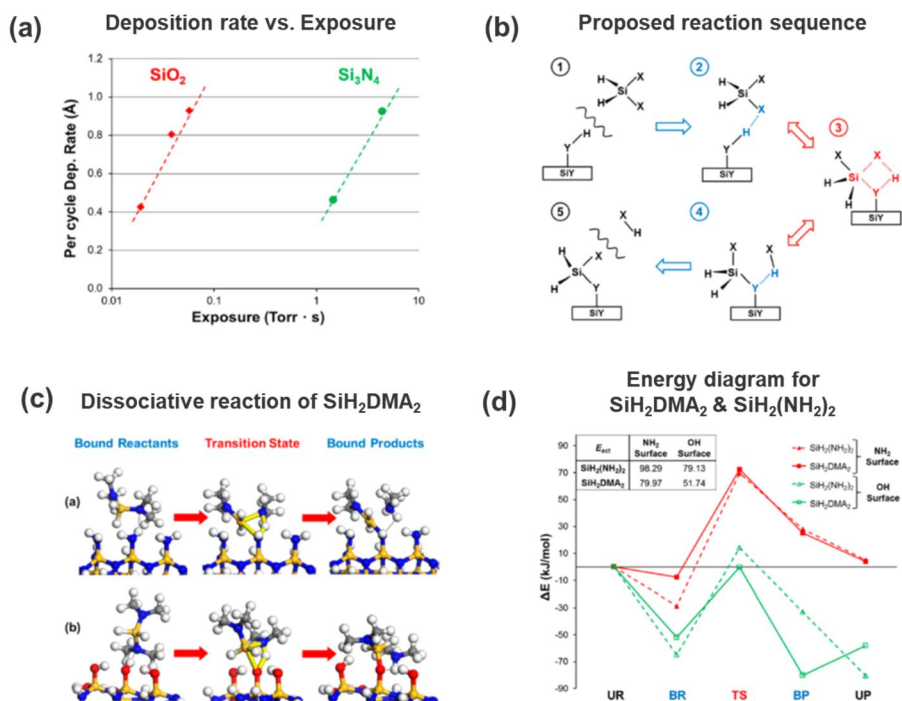


Figure 1.11. Highlighted figures were organized. (a) Deposition rate versus exposure of SiO₂ (red diamonds) and Si₃N₄ (green circles) films deposited from chloro-silane precursors by ALD at 450 °C with less than 2% absolute variation on per cycle deposition rate. (b) Proposed mechanistic steps for reactive chemisorption of SiH₂X₂ precursor and desorption of functional group X via proton transfer from a Si–Y–H functionalized surface (Y = O, NH, or N). Structure 1 depicts the initial unbound reactants (UR) step; structure 2, the bound reactants (BR); structure 3, the transition state (TS); structure 4, the bound product (BP) step and structure 5, the final unbound products (UP). (c) BP86/SV(P) optimized geometries of bound reactants, transition state, and bound products structures for SiH₂DMA₂ with (c-a) (Si₃N₄)₄(NH₃)₁₂ as a model for silicon nitride growth and (c-b)

$(\text{Si}_3\text{N}_4)_4(\text{H}_2\text{O})_{12}$ as a model for silicon oxide growth. (d) Energetics for the bound reactants (BR), transition state (TS), bound products (BP), and unbound products (UP) relative to the unbound reactants (UR) for the reaction of $\text{SiH}_2(\text{NH}_2)_2$ (triangles, dashed lines), SiH_2DMA_2 (squares, solid lines) with the cluster models $(\text{Si}_3\text{N}_4)_4(\text{NH}_3)_{12}$ (red) and $(\text{Si}_3\text{N}_4)_4(\text{H}_2\text{O})_{12}$ (green).[47]

1.5.3. Modeling the ALD of metals: Cu

Many copper organometallic compounds are used with H₂ or N₂ plasma in copper ALD experiments.[48, 49] However, these processes lead to impurities and discontinuous films either because of the higher temperature requirement or because of the strong reducing or oxidizing nature of the coreagents.[50-52] Significant progress was made by Lee et al. in developing low temperature ALD of copper metal using the reaction of copper dimethylamino-2-propoxide [Cu(dmap)₂] and diethylzinc [Et₂Zn] at 100-120 °C.[52] Although subsequent work reported that the parasitic CVD reaction of Et₂Zn may lead to Zn incorporation into the copper thin film, the work by Lee et al. has important implications on the coreagent strategy which was traditionally limited to the use of molecular or plasma H₂. The reaction of Cu(dmap)₂ and Et₂Zn was previously used to synthesize Cu/Zn alloy nanocolloids using thermolysis.[53] Vidjayacoumar et al. investigated ALD reactions of eight different copper(II) complexes separately with AlMe₃, BEt₃, and Et₂Zn in order to identify the most promising combination of the copper precursor and coreagent.[54] The reductive properties of various metallocenes along with different copper precursors were investigated with density functional theory (DFT) and solution phase chemistry to evaluate the use of metallocene compounds as reducing agents for Cu ALD.[55]

Cu(dmap)₂ has been a popular choice for other Cu ALD processes. For example, Knisley et al. reported a low temperature three-step ALD process using Cu(dmap)₂, formic acid (HCO₂H), and hydrazine (N₂H₄) at 120 °C and indicated that their method can avoid undesired elements in the precursors and affords high purity low resistivity copper metal. Kalutarage et

al. compared two-step and three-step processes using the ALD reaction of $\text{Cu}(\text{dmap})_2$ with $\text{BH}_3(\text{NHMe}_2)$ and separately with $\text{BH}_3(\text{NHMe}_2)$ and HCO_2H . [56] They showed that the two-step process requires a Cu seed layer and affords a growth rate of about 0.13 Å/cycle within the 130-160 °C ALD window. The three-step process does not need a Cu seed layer for growth and affords a growth rate of 0.20 Å/cycle within the 135-165 °C ALD window. Guo et al. explored an ALD process for depositing copper thin film on silicon wafers and glass slides at 50 °C using copper(I)-N,N'-diisopropylacetamidinate precursor and H_2 plasma. [57] The focus in many of those experimental works is on the deposition and characterization of copper thin films, with less elaboration of the self-terminating surface reactions that are important requirement for an ALD process. Computational studies such as electronic structure calculations can be an efficient way to investigate the surface reactions during ALD and provide useful information to develop better processes. [58] For instance, developing a model for island formation will require knowledge of the kinetics of the underlying deposition reactions.

They found that the chemisorbed $\text{Cu}(\text{dmap})_2$ decomposes through breaking one or both Cu–O on Cu(111) during the $\text{Cu}(\text{dmap})_2$ pulse. The surface saturates with rather immobile dmap and $\text{Cu}(\text{dmap})$ fragments, which prevents multilayer adsorption of $\text{Cu}(\text{dmap})_2$ precursors, thus meeting the condition for ALD. The reaction of Et_2Zn with the dmap and $\text{Cu}(\text{dmap})$ fragments at the surface proceeds via two different reaction routes. The first route in **Figure 1.12(a-b)** starts with butane formation from the adsorbed Et_2Zn molecule, aided through the cooperative role of dmap ligands on the surface. This is followed by the diffusion and reordering of dmap ligands around the Zn atom to form the $\text{Zn}(\text{dmap})_2$ molecule, which finally desorbs.

In the second case as shown in **Figure 1.12(c-d)**, the dmap ligands diffuse and reorder around the Zn atom. Zn(dmap)_2 is formed and desorbs in the presence of ethyl groups, which again lower the barriers for these reactions. Subsequently, butane formation is found not to occur on the bare Cu(111) surface. Instead, the intermediate reaction product Cu(Et)_2 is formed from the diffusion of adatom Cu on the surface, and this facilitates butane formation and desorption.

In general, the butane formation and desorption steps are exothermic, while the ligand diffusion and reordering steps are endothermic, which may result in residual dmap ligands blocking surface sites at the end of the Et_2Zn pulse and in residual Zn being reduced and incorporated as an impurity. It is found that the formation and desorption of Et_2Zn and Zn(dmap)_2 byproducts are facilitated by the presence of nearby ligands (the “cooperative effect”).

In this transmetalation mechanism, the ALD growth rate is determined both by the saturating coverage of Et groups at the end of the Et_2Zn pulse (since each contributes one electron toward reduction of Cu) and by the saturating adsorption of Cu(dmap)_2 during the Cu pulse. Based on the rather slow rates of ligand diffusion that we computed, we suggest that saturation is reached before Et or dmap groups pack perfectly on the surface. We therefore estimate that Cu is deposited at approximately 0.18 Å/cycle, which agrees well with experiment.

They find that there is competition between alternative surface reactions, both leading to Cu deposition, and that which the reaction mechanism is followed depends on the coverage of the ligands on the surface. We found that the cooperative role of ligands and Cu adatoms is an important factor that lowers activation barriers. The method that we used in this study

and the ALD mechanisms that we obtained provide insight into the ALD of copper and other transition metals.

1.6. Literature survey of previous researches for W ALD

W ALD is the most successful case among elemental metal ALD processes. This is mainly due to the fact that W ALD is accomplished from the well-known good metal-containing precursor, WF_6 , and good reducing agents, silane or borane compound. The successful deposition of ALD-W was first reported by Klaus et al.[60] They used a sequential supply of WF_6 and disilane Si_2H_6 at the temperature of lower than $325^\circ C$, which is low enough for semiconductor device fabrication. Later, it was reported that the ALD-W films could be deposited by using diborane (B_2H_6) as a reducing agent of WF_6 at $300^\circ C$.[61] The ALD-W process using a very similar reducing agent to disilane, silane (SiH_4),[62] was also extensively investigated. Recently, the effect of B_2H_6 pretreatment on ALD-W film deposited using an alternating supply of WF_6 and SiH_4 was reported.[62] The results showed that the B_2H_6 pretreatment could enhance the nucleation of ALD-W on SiO_2 and also enhance the step coverage of ALD-W films at UHAR contact.

At first, Soo-Hyun Kim et al.,[63] investigated the properties of three kinds of ALD-W films (two SiH_4 -based ALD-W films and one B_2H_6 -based ALD-W film) as nucleation layers for W-plug process of 70 nm design-rule DRAM.

Although no F was detected in XPS analysis, in order to more sensitively detect F impurities SIMS depth profiling was performed as shown in **Fig. 1.13(a)**. F concentration was much lower in B_2H_6 -based ALD-W film ($\sim 1.2 \times 10^{17}/cm^3$) as compared to those of SiH_4 -based ALD-W films ($1 \sim 5.4 \times 10^{20}/cm^3$). This indicates that B_2H_6 pulsing is more effective in reducing WF_x absorbed on the surface and making pure metal W film.

To further determine the phase and microstructure, the films were analyzed using TEM. The plan-view TEM bright-field BF images of 20 nm thick ALD-W A film in **Figure 1.13(b)** showed that the film formed a polycrystalline structure with the grain size ranging from ~9-17 nm and not an amorphous one. Indexing of selected area diffraction pattern SADP showed a clear ring pattern of bcc α -W. Diffraction rings, which can be indexed as β -W (200) ($d = 2.52 \text{ \AA}$) and β -W (211) ($d = 2.08 \text{ \AA}$), respectively, were observed close to α -W (110) ($d = 2.238 \text{ \AA}$). The XTEM image of ALD-W (A) showed a crystalline microstructure with a relatively rough film surface. The TEM analysis of ALD-W (B) showed a very similar plan-view image to that of ALD-W (A). The sharp diffraction pattern from β -W phase matches well with the XRD results. However, the grain size slightly increased to ~11-21 nm. Slightly larger grains of ALD-W (B) than those of ALD-W (A) partly explain its relatively lower resistivity. Another reason why the ALD-W (B) showed a lower resistivity in spite of having the relatively larger amount of -W phase compared with ALD-W (A) is its lower roughness. The root-mean-square (rms) roughness at ~20 nm thickness was ~1 nm for ALD-W (B) and ~2 nm for ALD-W A, respectively. The XTEM image of ALD-W (B) showed the relatively lower surface roughness as compared to ALD-W (A).

Figure 1.13(b) shows the plan-view TEM BF images of 20 nm thick B_2H_6 -based ALD-W film ALD-W (C). A plan-view TEM image seems to be featureless, indicating that the film forms the amorphous structure. This was confirmed by the corresponding faint SADP. Thus, in TEM analysis, the amorphous nature of B_2H_6 -based ALD-W film has a clear advantage in terms of barrier performance to WF_6 diffusion occurring at the subsequent plug-fill

step compared to SiH₄-based ALD-W films. The XTEM image of 20 nm thick ALD-W (C) film showed very smooth surface topography as compared to those of ALD-W (A) and ALD-W (B).

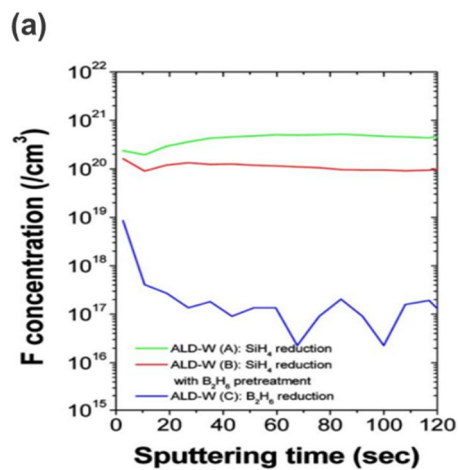
The formation of amorphous W film as a nucleation layer for W-plug process has many advantages such as superior diffusion barrier properties, less-sensitive thickness effect of film resistivity, and the large-size grains formation growing on it, leading to lowering the resistivity of the W-plug stack. The results demonstrated that the integration scheme with B₂H₆-based ALD-W film showed a much lower contact resistance at UHAR contact. The B₂H₆-based process also has advantages in terms of nucleation on SiO₂. The enhanced nucleation on SiO₂ by B₂H₆-based process provides a stable and low contact resistance with MOCVD-TiN as the barrier layer with limited step coverage. By the same argument, the B₂H₆ pretreatment prior to ALD-W formation using SiH₄ reduction contributed to the enhancement of the nucleation and assured stable and low contact resistance at the UHAR contact in this study.

At second, Guilei Wang et al.,[64] also investigated the properties of ALD-W films (SiH₄-based ALD-W films and B₂H₆-based ALD-W film). W films were grown in ALD chamber using two different precursors (SiH₄ and B₂H₆). The growth rate of W films using SiH₄ 0.67 nm/cycle is larger than that using B₂H₆ 0.31 nm/cycle. In **Figure 1.14(a)**, the plot of thickness vs. sheet resistance indicates that W film grown using B₂H₆ has lower resistivity compared to W film grown using SiH₄.

Diffraction spectrums shown in **Figure 1.14(b)** display that W film grown using SiH₄ is polycrystalline whereas W film grown using B₂H₆ is amorphous. The filling capability of ALD W films using SiH₄ or B₂H₆ is

tested on devices with 22 nm gate length as shown in **Figure 1.14(c)**. It can be seen that W filling using B_2H_6 is superior to that using SiH_4 since it shows void-free W filling. In order to verify if ALD W filling using B_2H_6 affects the equivalent oxide thickness (EOT) due to B diffusion into high-K dielectric, diodes with high-K dielectric & ALD W films using both SiH_4 and B_2H_6 were fabricated.

In conclusion, ALD W using SiH_4 and B_2H_6 were investigated. In contrast to ALD W using SiH_4 , ALD W using B_2H_6 shows lower growth rate, resistivity and better gap filling capability. The incorporation of B in ALD W films doesn't affect the C-V characteristics. Therefore, ALD W using B_2H_6 is a good gate filling metal which can be widely used in advanced devices.



(b)

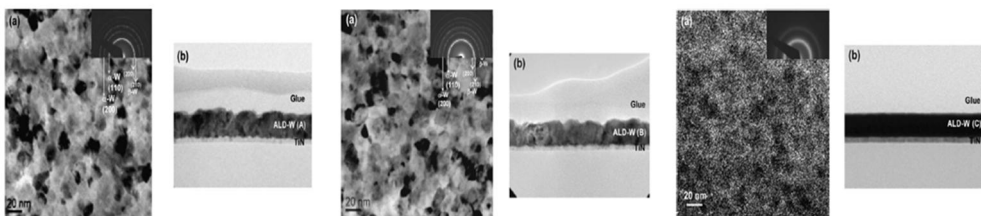


Figure 1.13. Highlighted figures were organized. (a) SIMS profile of fluorine in ALD W (b) TEM images of ALD W for sample A(left), B(center), and C(right).[63]

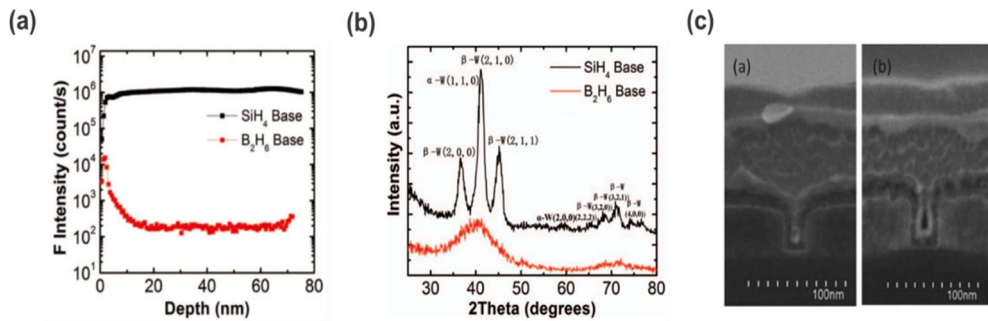


Figure 1.14. Highlighted figures were organized. (a) SIMS profile of fluorine in ALD W (b) XRD spectra in ALD W (c) SEM images of gap filling capability in ALD W.[64]

1.7. Technical issues of word-line W in VNAND

Recently, in order to keep a trend of increasing bit density and reducing bit cost of NAND flash memories, three-dimensional Bit-Cost Scalable (BiCS) flash technology has been proposed[65]. However, there are two major concerns on the BiCS flash. First of all, it is almost impossible to implement metal gate structure for BiCS flash because it is very difficult to etch metal/oxide multilayer simultaneously. We cannot utilize various advantages of metal gate SONOS cell structure, for example, faster erase speed, wider V_{th} margin, and better retention characteristics[66]. Another concern is GIDL erase of BiCS flash. An extensive circuit change may be necessary to apply negative bias on word line during erase operation. Area penalty and limited erase voltage are expected. **Figure 1.15(a) and (b)** show the cross-sectional SEM images of the fabricated TCAT flash cell array. The cell string has six-NAND cell transistors with SSL transistor at the top and the GSL transistor at the bottom. The SSL and GSL transistors are formed simultaneously with cell transistors.

In the fabrication process of memory devices, a void-free tungsten (W) gate process with good conformability is very important for improving the conductivity of the W gate, leading to enhancement of device performance. Despite much effort in improving ALD W processes, as memory devices become smaller and smaller, the limitation of conformality at ultrahigh aspect ratio (UHAR) contact can induce potential problems such as a seam or void in the final W-plug, leading to an increase in contact resistance.[67, 68] Further downscaling the memory devices necessitates the theoretical comprehension of the ALD W process due to the experimentally limited

observations on the sub-nanometer scale. Although a few experimental studies on ALD W have been investigated, there has been no theoretical report on the reactivity of B_2H_6 .

There are two technical issues of word-line W in **Figure 1.15(c)**:

Issue 1 - Formation of voids due to very deep trench in 128-layer VNAND

Issue 2 - Fluorine attack to bottom layers due to ultra-thin($\sim\text{\AA}$) and island-shaped TiN under W ALD using WF_6 precursor

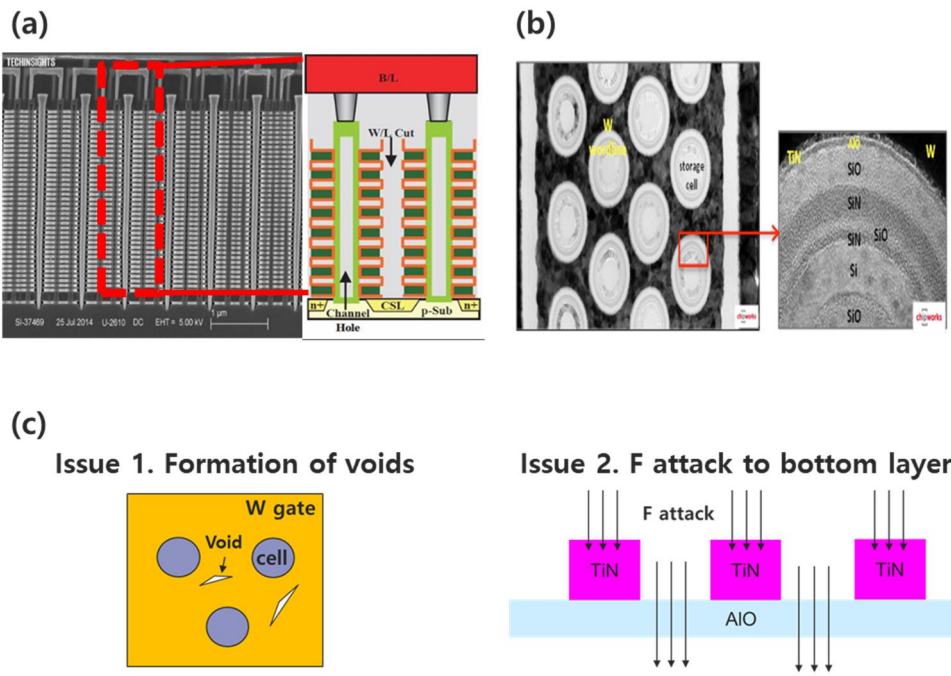


Figure 1.15. (a) Cross-section of Samsung 32-layer VNAND (b) Plan-view of Samsung 32-layer VNAND (c) two technical issues for voids and F attack.[69]

1.8. Objective of this research

As the size of the memory device becomes smaller and smaller, it becomes difficult to deposit W films having excellent step coverage and conformality due to a severe problem that a seam or void is formed in the process of filling the W metal gate. This problem is a primary obstacle of the development for future memory devices.[62] To treat this problem, theoretical comprehension of the ALD process for W deposition is required due to the experimentally limited observations on the sub-nanometer scale. Although a few experimental results on ALD W have been reported, there has been no theoretical report on the overall reaction mechanism for ALD W process.

Objective of this research can be summarized in **Figure 1.16** as follows:

1st study – B_2H_6 reactivity on different orientations of TiN in order to analysis on formation of void & F attack

2nd study – Effects of H_2 & N_2 treatment for B_2H_6 reaction on TiN in order to analysis on H_2 & N_2 effects

3rd study – Overall reaction mechanism for W ALD in order to analysis on W ALD reaction mechanism, role of B_2H_6 gas, proposal of new ALD process

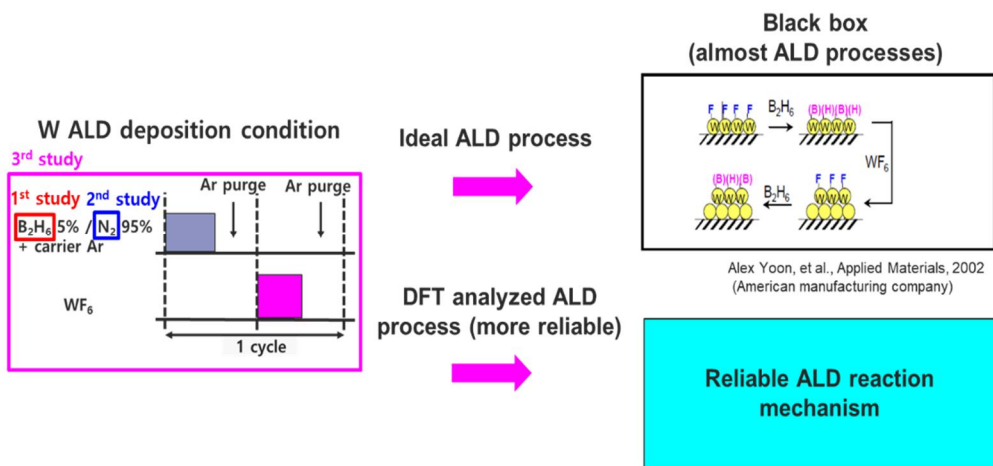


Figure 1.16. Schematics of our research goals.

1.9. Bibliography

- [1] G. E. Moore, "Cramming More Components Onto Integrated Circuits," *Proceedings of the IEEE*, vol. 86, no. 1, pp. 82-85, 1998.
- [2] R. Bennett. (2015). *100 Years of Moore's Law*. Available: <http://hightechforum.org/100-years-of-moores-law/>
- [3] S. Anthony. (2011). *Is 14nm the end of the road for silicon chips?* Available: <https://www.extremetech.com/computing/97469-is-14nm-the-end-of-the-road-for-silicon-lithography>
- [4] H. SINGH, "Overcoming challenges in 3D NAND volume manufacturing," vol. 5, no. 60,
- [5] Y. W. Park, "Flash Memory," in *IEDM short course*, 2015.
- [6] T. S. a. J. Antson, "Method for producing compound thin films," US Patent 4058, 1977.
- [7] R. L. Puurunen, "Surface chemistry of atomic layer deposition: A case study for the trimethylaluminum/water process," *Journal of Applied Physics*, vol. 97, no. 12, p. 121301, 2005.
- [8] R. L. Puurunen, "A Short History of Atomic Layer Deposition: Tuomo Suntola's Atomic Layer Epitaxy," *Chemical Vapor Deposition*, vol. 20, no. 10-11-12, pp. 332-344, 2014.
- [9] K. Knapas and M. Ritala, "In Situ Studies on Reaction Mechanisms in Atomic Layer Deposition," *Critical Reviews in Solid State and Materials Sciences*, vol. 38, no. 3, pp. 167-202, 2013/01/01 2013.
- [10] T. A. Finland. (2018). *Millennium Technology Prize for Tuomo Suntola*. Available: <https://taf.fi/2018/05/22/2018-millennium-technology-prize-for-tuomo-suntola-finnish-physicists-innovation-enables-manufacture-and-development-of-information-technology-products/>
- [11] M. L. T. Pakkanen, and V. Nevalainen, "Quantum chemical studies of the formation of zinc sulfide surface by the ALE technique," in *First symposium on Atomic Layer Epitaxy*, 1984, vol. 54: VTT Symposium.
- [12] S. M. George, "Atomic Layer Deposition: An Overview," *Chemical Reviews*, vol. 110, no. 1, pp. 111-131, Jan 2010.
- [13] K. J. Kanarik *et al.*, "Overview of atomic layer etching in the semiconductor industry," *Journal of Vacuum Science & Technology A*, vol. 33, no. 2, p. 020802, 2015.
- [14] J. A. Singh *et al.*, "Area-Selective Atomic Layer Deposition of Metal Oxides on Noble Metals through Catalytic Oxygen Activation,"

- Chemistry of Materials*, vol. 30, no. 3, pp. 663-670, 2018/02/13 2018.
- [15] B. J. O'Neill *et al.*, "Catalyst Design with Atomic Layer Deposition," *ACS Catalysis*, vol. 5, no. 3, pp. 1804-1825, 2015/03/06 2015.
- [16] M. B. E. Griffiths, P. J. Pallister, D. J. Mandia, and S. T. Barry, "Atomic Layer Deposition of Gold Metal," *Chemistry of Materials*, vol. 28, no. 1, pp. 44-46, 2016/01/12 2016.
- [17] J. Lu, J. W. Elam, and P. C. Stair, "Atomic layer deposition—Sequential self-limiting surface reactions for advanced catalyst “bottom-up” synthesis," *Surface Science Reports*, vol. 71, no. 2, pp. 410-472, 2016/06/01/ 2016.
- [18] K. L. Choy, "Chemical vapour deposition of coatings," *Progress in Materials Science*, vol. 48, no. 2, pp. 57-170, 2003/01/01/ 2003.
- [19] G. Malandrino, "Chemical Vapour Deposition. Precursors, Processes and Applications. Edited by Anthony C. Jones and Michael L. Hitchman," *Angewandte Chemie International Edition*, vol. 48, no. 41, pp. 7478-7479, 2009.
- [20] T. Suntola and J. Hyvarinen, "Atomic Layer Epitaxy," *Annual Review of Materials Science*, vol. 15, no. 1, pp. 177-195, 1985.
- [21] M. Leskelä and M. Ritala, "Atomic Layer Deposition Chemistry: Recent Developments and Future Challenges," *Angewandte Chemie International Edition*, vol. 42, no. 45, pp. 5548-5554, 2003.
- [22] D. C. Tommi Kääriäinen , Marja-Leena Kääriäinen , Arthur Sherman, *Atomic Layer Deposition: Principles, Characteristics, and Nanotechnology Applications*. Wiley, 2013.
- [23] T. Terasako, Y. Ishiko, K. Saeki, S. Yudate, and S. Shirakata, "Properties of ZnO epitaxial layers and polycrystalline films prepared by metalorganic molecular beam epitaxial apparatus using diethylzinc and water as precursors," *Journal of Crystal Growth*, vol. 298, pp. 481-485, 2007/01/01/ 2007.
- [24] E. Guzewicz *et al.*, "Extremely low temperature growth of ZnO by atomic layer deposition," *Journal of Applied Physics*, vol. 103, no. 3, p. 033515, 2008.
- [25] Y. Kuzminykh, A. Dabirian, M. Reinke, and P. Hoffmann, "High vacuum chemical vapour deposition of oxides.: A review of technique development and precursor selection," *Surface and Coatings Technology*, vol. 230, pp. 13-21, 2013/09/15/ 2013.
- [26] M. Reinke, Y. Kuzminykh, and P. Hoffmann, "Limitations of patterning thin films by shadow mask high vacuum chemical vapor

- deposition," *Thin Solid Films*, vol. 563, pp. 56-61, 2014/07/31/ 2014.
- [27] H. J. Cho *et al.*, "New TIT capacitor with ZrO₂/Al₂O₃/ZrO₂ dielectrics for 60 nm and below DRAMs," *Solid-State Electronics*, vol. 51, no. 11-12, pp. 1529-1533, 2007.
- [28] M. Ritala, & Leskelä, M., *Atomic Layer Deposition*. Handbook of Thin Films Materials: Deposition and Processing of Thin Films, 2002.
- [29] R. N. Hall and J. H. Racette, "Diffusion and Solubility of Copper in Extrinsic and Intrinsic Germanium, Silicon, and Gallium Arsenide," *Journal of Applied Physics*, vol. 35, no. 2, pp. 379-397, 1964.
- [30] A. Delabie *et al.*, "Scaling to sub-1 nm equivalent oxide thickness with hafnium oxide deposited by atomic layer deposition," *Journal of the Electrochemical Society*, vol. 153, no. 8, pp. F180-F187, 2006.
- [31] M. Reinke, Y. Kuzminykh, and P. Hoffmann, "Low Temperature Chemical Vapor Deposition Using Atomic Layer Deposition Chemistry," *Chemistry of Materials*, vol. 27, no. 5, pp. 1604-1611, 2015/03/10 2015.
- [32] G. Dey, "Atomic layer deposition of copper - study through density functional theory," Ph.D., University College Cork, 2014.
- [33] S. B. Baek, D. H. Kim, and Y. C. Kim, "Adsorption and surface reaction of bis-diethylaminosilane as a Si precursor on an OH-terminated Si (001) surface," *Applied Surface Science*, vol. 258, no. 17, pp. 6341-6344, Jun 15 2012.
- [34] Y.-C. Jeong, S.-B. Baek, D.-H. Kim, J.-S. Kim, and Y.-C. Kim, "Initial reaction of silicon precursors with a varying number of dimethylamino ligands on a hydroxyl-terminated silicon (001) surface," *Applied Surface Science*, vol. 280, pp. 207-211, 2013/09/01/ 2013.
- [35] Q. M. Phung, S. Vancoillie, G. Pourtois, J. Swerts, K. Pierloot, and A. Delabie, "Atomic Layer Deposition of Ruthenium on a Titanium Nitride Surface: A Density Functional Theory Study," *The Journal of Physical Chemistry C*, vol. 117, no. 38, pp. 19442-19453, 2013/09/26 2013.
- [36] E. O. C. Paul K. Hurley, Scott Monaghan, Rathnait Long, Aileen O'Mahony, Ian M. Povey, Karim Cherkaoui, John MacHale, Aidan Quinn, Guy Brammertz, Marc M. Heyns, Simon Newcomb, Valeri V. Afanas'ev, Arif Sonnet, Rohit Galatage, Naqi Jivani, Eric Vogel, Robert M. Wallace, and Martyn Pemble "Structural and Electrical Properties of HfO₂/n-In_xGa_{1-x}As structures (x: 0, 0.15, 0.3 and

- 0.53)," *Electrochemical Society Transactions*, vol. 25, pp. 113-127, 2009.
- [37] M. C. Annelies Delabie, Bert Brijs, David Brunco, Thierry Conard, Erik Sleenckx, Lars-Ake Ragnarsson, Sven Van Elshocht, Stefan De Gendt, and Marc Heyns "Growth Studies and Reaction Mechanism of the Atomic Layer Deposition of Hafnium Oxide," *Electrochemical Society Transactions*, vol. 1, pp. 433-446, 2006.
- [38] R. Haerle, E. Riedo, A. Pasquarello, and A. Baldereschi, *Sp²/sp³ hybridization ratio in amorphous carbon from C 1s core-level shifts: X-ray photoelectron spectroscopy and first-principles calculation*. 2002.
- [39] S. Olivier, J.-M. Duc  r  , C. Mastail, G. Landa, A. Est  ve, and M. D. Rouhani, "Insights into Crystalline Preorganization of Gas-Phase Precursors: Densification Mechanisms," *Chemistry of Materials*, vol. 20, no. 4, pp. 1555-1560, 2008/02/01 2008.
- [40] W. Weinreich *et al.*, "TEMAZ/O₃ atomic layer deposition process with doubled growth rate and optimized interface properties in metal–insulator–metal capacitors," *Journal of Vacuum Science & Technology A*, vol. 31, no. 1, p. 01A123, 2013.
- [41] M. Shirazi and S. D. Elliott, "Multiple Proton Diffusion and Film Densification in Atomic Layer Deposition Modeled by Density Functional Theory," *Chemistry of Materials*, vol. 25, no. 6, pp. 878-889, 2013/03/26 2013.
- [42] L. Huang *et al.*, "First-Principles Study of a Full Cycle of Atomic Layer Deposition of SiO₂ Thin Films with Di(sec-butylamino)silane and Ozone," *The Journal of Physical Chemistry C*, vol. 117, no. 38, pp. 19454-19463, 2013/09/26 2013.
- [43] K. Endo *et al.*, "Enhancement of FinFET performance using 25-nm-thin sidewall spacer grown by atomic layer deposition," *Solid-State Electronics*, vol. 74, pp. 13-18, 2012/08/01/ 2012.
- [44] J.-E. P. a. J.-H. K. a. J.-W. L. a. J.-h. Y. a. K.-S. C. a. S.-H. L. a. M.-H. P. a. N.-I. L. and Ho-Kyu Kang and Kwang-Pyuk Suh and Byoung-Ha Cho and Byoung-Chul Kim and Cheol-Ho Shin, "Mass-productive ultra-low temperature ALD SiO₂/sub 2/ process promising for sub-90 nm memory and logic devices " in *Digest. International Electron Devices Meeting*, 2002, pp. 229-232.
- [45] J. W. Klaus, A. W. Ott, A. C. Dillon, and S. M. George, "Atomic layer controlled growth of Si₃N₄ films using sequential surface reactions,"

- Surface Science*, vol. 418, no. 1, pp. L14-L19, 1998/11/27/ 1998.
- [46] C. Mui, Y. Widjaja, J. K. Kang, and C. B. Musgrave, "Surface reaction mechanisms for atomic layer deposition of silicon nitride," *Surface Science*, vol. 557, no. 1, pp. 159-170, 2004/05/20/ 2004.
- [47] C. A. Murray, S. D. Elliott, D. Hausmann, J. Henri, and A. LaVoie, "Effect of Reaction Mechanism on Precursor Exposure Time in Atomic Layer Deposition of Silicon Oxide and Silicon Nitride," *ACS Applied Materials & Interfaces*, vol. 6, no. 13, pp. 10534-10541, 2014/07/09 2014.
- [48] P. Mårtensson and J.-O. Carlsson, "Atomic Layer Epitaxy of Copper on Tantalum," *Chemical Vapor Deposition*, vol. 3, no. 1, pp. 45-50, 1997.
- [49] A. Niskanen, A. Rahtu, T. Sajavaara, K. Arstila, M. Ritala, and M. Leskela, "Radical-enhanced atomic layer deposition of metallic copper thin films," *Journal of the Electrochemical Society*, vol. 152, no. 1, pp. G25-G28, 2005.
- [50] D. J. Hagen *et al.*, "Plasma enhanced atomic layer deposition of copper: A comparison of precursors," *Surface and Coatings Technology*, vol. 230, pp. 3-12, 2013/09/15/ 2013.
- [51] B. Vidjayacoumar, D. J. H. Emslie, S. B. Clendenning, J. M. Blackwell, J. F. Britten, and A. Rheingold, "Investigation of AlMe₃, BEt₃, and ZnEt₂ as Co-Reagents for Low-Temperature Copper Metal ALD/Pulsed-CVD," *Chemistry of Materials*, vol. 22, no. 17, pp. 4844-4853, 2010/09/14 2010.
- [52] B. H. Lee *et al.*, "Low-Temperature Atomic Layer Deposition of Copper Metal Thin Films: Self-Limiting Surface Reaction of Copper Dimethylamino-2-propoxide with Diethylzinc," *Angewandte Chemie International Edition*, vol. 48, no. 25, pp. 4536-4539, 2009.
- [53] J. Hambrock, M. K. Schröter, A. Birkner, C. Wöll, and R. A. Fischer, "Nano-Brass: Bimetallic Copper/Zinc Colloids by a Nonaqueous Organometallic Route Using [Cu(OCH(Me)CH₂NMe₂)₂] and Et₂Zn as Precursors," *Chemistry of Materials*, vol. 15, no. 22, pp. 4217-4222, 2003/11/01 2003.
- [54] B. Vidjayacoumar, D. J. H. Emslie, J. M. Blackwell, S. B. Clendenning, and J. F. Britten, "Solution Reactions of a Bis(pyrrolylaldimate)copper(II) Complex with Peralkyl Zinc, Aluminum, and Boron Reagents: Investigation of the Pathways Responsible for Copper Metal Deposition," *Chemistry of Materials*,

- vol. 22, no. 17, pp. 4854-4866, 2010/09/14 2010.
- [55] G. Dey, J. S. Wrench, D. J. Hagen, L. Keeney, and S. D. Elliott, "Quantum chemical and solution phase evaluation of metallocenes as reducing agents for the prospective atomic layer deposition of copper," *Dalton Transactions*, 10.1039/C5DT00922G vol. 44, no. 22, pp. 10188-10199, 2015.
- [56] L. C. Kalutarage, S. B. Clendenning, and C. H. Winter, "Low-Temperature Atomic Layer Deposition of Copper Films Using Borane Dimethylamine as the Reducing Co-reagent," *Chemistry of Materials*, vol. 26, no. 12, pp. 3731-3738, 2014/06/24 2014.
- [57] Z. Guo *et al.*, "Low-Temperature Atomic Layer Deposition of High Purity, Smooth, Low Resistivity Copper Films by Using Amidinate Precursor and Hydrogen Plasma," *Chemistry of Materials*, vol. 27, no. 17, pp. 5988-5996, 2015/09/08 2015.
- [58] D. E. Simon, "Atomic-scale simulation of ALD chemistry," *Semiconductor Science and Technology*, vol. 27, no. 7, p. 074008, 2012.
- [59] Y. Maimaiti and S. D. Elliott, "Kinetics and Coverage Dependent Reaction Mechanisms of the Copper Atomic Layer Deposition from Copper Dimethylamino-2-propoxide and Diethylzinc," *Chemistry of Materials*, vol. 28, no. 17, pp. 6282-6295, 2016/09/13 2016.
- [60] J. W. Klaus, S. J. Ferro, and S. M. George, "Atomic layer deposition of tungsten using sequential surface chemistry with a sacrificial stripping reaction," *Thin Solid Films*, vol. 360, no. 1-2, pp. 145-153, Feb 1 2000.
- [61] H. C. M. Yang, A. Yoon, H. Fang, A. Zhang, C. Knepler, R. Jackson, J. S. Byun, A. Mak, M. Eizenberg, M. Xi, M. Kori, and A. K. Sinha, "'Atomic Layer Deposition of Tungsten Film from WF₆/B₂H₆: Nucleation Layer for Advanced Semiconductor Devices," in *Conference Proceedings ULSI XVII*, 2002, pp. 655-660: Materials Research Society.
- [62] S. H. Kim *et al.*, "Characterizations of pulsed chemical vapor deposited-tungsten thin films for ultrahigh aspect ratio W-plug process," *Journal of the Electrochemical Society*, vol. 152, no. 6, pp. C408-C417, 2005.
- [63] S. H. Kim, N. Kwak, J. Kim, and H. Sohn, "A comparative study of the atomic-layer-deposited tungsten thin films as nucleation layers for

- W-plug deposition," *Journal of the Electrochemical Society*, vol. 153, no. 10, pp. G887-G893, 2006.
- [64] G. L. Wang *et al.*, "Application of Atomic Layer Deposition Tungsten (ALD W) as Gate Filling Metal for 22 nm and Beyond Nodes CMOS Technology," *Ecs Journal of Solid State Science and Technology*, vol. 3, no. 4, pp. P82-P85, 2014.
- [65] M. K. H. Tanaka, K. Yahashi, M. Oomura, R. Katsumata, M. Kito, Y. Fukuzumi, M. Sato, Y. Nagata, Y. Matsuoka, Y. Iwata, H. Aochi, and A. Nitayama, "Bit cost scalable technology with punch and plug process for ultra high density flash memory," in *VLSI Symp. Tech. Dig.*, 2007, pp. 14-15.
- [66] K. I. C. Chang Hyun Lee, Myoung Kwan Cho, Yun Heub Song, Kyu Charn Park, Kinam Kim, "A novel SONOS structure of SiO₂/SiN/Al₂O₃ with TaN metal gate for multi-giga bit flash memories," in *IEDM Tech. Dig.*, 2003, pp. 613-616.
- [67] S. H. Kim, J. T. Kim, N. Kwak, J. Kim, T. S. Yoon, and H. Sohn, "Effects of phase of underlying W film on chemical vapor deposited-W film growth and applications to contact-plug and bit line processes for memory devices," *Journal of Vacuum Science & Technology B*, vol. 25, no. 5, pp. 1574-1580, Sep-Oct 2007.
- [68] T. Omstead, G. C. D' Couto, S. H. Lee, P. Wongsenakaum, J. Collins, and K. Levy, "Filling high-AR structures using pulsed nucleation layer deposition," *Solid State Technology*, vol. 45, no. 9, pp. 51-+, Sep 2002.
- [69] J. Jang *et al.*, "Vertical cell array using TCAT(Terabit Cell Array Transistor) technology for ultra high density NAND flash memory," in *2009 Symposium on VLSI Technology*, 2006, pp. 192-193.

Chapter 2. Theoretical background

Density functional theory (DFT) is an extremely powerful tool for studying various problems in physics, chemistry and material science. It is a computational scheme to efficiently solve the Schrödinger equation for complex many-body systems from first principles. This chapter outlines the basic concepts of DFT as the entire work in this thesis is based on calculations using DFT.

2.1. Density functional theory

2.1.1. The Many-body problem

The basis for all quantum mechanical calculations of the electronic structure of a material is the time-independent Schrödinger equation,

$$H\psi(r, R) = E\psi(r, R) \quad (2.1)$$

where H is the Hamiltonian operator, E is the energy eigenvalue and ψ is the wave function. r and R list all the coordinates of the electrons and nuclei, respectively. Using atomic units (i.e. $m_e = \hbar = e = 1$), a nonrelativistic system of electrons and nuclei can be described with a Hamiltonian[70],

$$\begin{aligned}
H = & -\frac{1}{2} \sum_i \nabla_i^2 - \sum_I \frac{\hbar^2}{2M_I} \nabla_I^2 + \frac{1}{2} \sum_{i \neq j} \frac{e^2}{|\mathbf{r}_i - \mathbf{r}_j|} + \frac{1}{2} \sum_{I \neq J} \frac{Z_I Z_J e^2}{|\mathbf{R}_I - \mathbf{R}_J|} \\
& - \sum_{i,I} \frac{Z_I e^2}{|\mathbf{r}_i - \mathbf{R}_I|}
\end{aligned} \tag{2.2}$$

where electrons are denoted by lower case subscripts and where nuclei, with charge Z_I and mass M_I , are denoted by upper case subscripts. The first and second terms denote the kinetic energies of electrons (T_e) and nuclei (T_n), respectively. The last three terms depict the electron-electron (V_{ee}), nuclei-nuclei (V_{nn}) and electron-nuclei (V_{en}) interactions, respectively. For convenience, Equation (2.2) can be rewritten,

$$H = T_e + T_n + V_{ee} + V_{nn} + V_{en} \tag{2.3}$$

Solving the Schrödinger equation analytically for more than a few particles is not feasible, but it can be solved with approximate methods. The first approximation to reduce the complexity is to assume independence of the nuclear and electron wave functions and then treat the slow-moving nuclei as classical particles. This is the Born-Oppenheimer approximation.[71] In the following section we introduce the theoretical basis of DFT.

2.1.2. The Hohenberg-Kohn theorems

The theorems initially formulated by Hohenberg and Kohn[72] constitute the theoretical basis of DFT. The first Hohenberg-Kohn theorem legitimizes the use of electron density $n(\mathbf{r})$ as the basic variable. It states:

Theorem I (Uniqueness): For any system of interacting particles in an external potential $V_{\text{ext}}(\mathbf{r})$, the potential $V_{\text{ext}}(\mathbf{r})$ is determined uniquely, except for a constant, by the ground state particle density $n_0(\mathbf{r})$.

An alternative explanation of this theorem: all the properties of the system are completely determined given only the ground state density $n_0(\mathbf{r})$. For example, the kinetic energy of the electrons T_e , etc, is uniquely determined if $n(\mathbf{r})$ is specified.

Theorem II (Uniqueness): A universal functional for the energy $E[n]$ in terms of the density $n(\mathbf{r})$ can be defined, valid for any external potential $V_{\text{ext}}(\mathbf{r})$. For any particular $V_{\text{ext}}(\mathbf{r})$, the exact ground state energy of the system is the global minimum value of this functional, and the density $n(\mathbf{r})$ that minimizes the functional is the exact ground state density $n_0(\mathbf{r})$.

According to theorem II, all the properties including the total energy can be viewed as functionals of the density,

$$\begin{aligned} E_{HK}[n] &= T[n] + E_{\text{int}}[n] + \int d^3r V_{\text{ext}}(\mathbf{r})n(\mathbf{r}) + E_{II} \\ &= F_{HK}[n(\mathbf{r})] + \int d^3r V_{\text{ext}}(\mathbf{r})n(\mathbf{r}) + E_{II} \end{aligned} \quad (2.4)$$

where E_{II} is the interaction energy of the nuclei. The functional $F_{HK}[n]$

includes all internal energies and kinetic energies of the interacting electron

$$F_{HK}[n(\mathbf{r})] = T[n] + E_{\text{int}}[n] \quad (2.5)$$

system,

If the functional $F_{HK}[n(\mathbf{r})]$ was known, then it would be possible to find the exact ground state density and energy by minimizing the total energy of the system in equation (2.4).

2.1.3. The Kohn-Sham equation

The basic idea of the Kohn–Sham approach is to replace the many-particle problem with a system of non-interacting particles which has the same ground state density $n(\mathbf{r})$ as the original many-particle system.[73] According to the Kohn-Sham approach, the Hohenberg-Kohn expression for the ground state energy functional (2.4) can be rewritten as

$$E_{KS} = T_s[n] + \int dr V_{\text{ext}}(r)n(r) + \frac{1}{2} \int d^3r d^3r' \frac{n(r)n(r')}{|\mathbf{r} - \mathbf{r}'|} + E_{II} + E_{xc}[n] \quad (2.6)$$

where $T_s[n]$ is non-interacting particle kinetic energy. The third term is the Hartree energy and $E_{xc}[n]$ is the exchange and correlation energy.

Performing variation of the energy in (2.6),

$$\delta E[n] = 0 \quad (2.7)$$

gives,

$$\frac{\delta E_{KS}}{\delta n(\mathbf{r})} = V_{\text{ext}} + \frac{1}{2} \int d^3 r' \frac{n(\mathbf{r}')}{|\mathbf{r} - \mathbf{r}'|} + \frac{\delta T_s[n]}{\delta n(\mathbf{r})} + \frac{\delta E_{xc}[n]}{\delta n(\mathbf{r})} \quad (2.8)$$

Defining the effective potential V_{eff} in the above equation,

$$V_{\text{eff}} = V_{\text{ext}} + \frac{1}{2} \int d^3 r' \frac{n(\mathbf{r}')}{|\mathbf{r} - \mathbf{r}'|} + \frac{\delta E_{xc}[n]}{\delta n(\mathbf{r})} \quad (2.9)$$

yields a set of Schrödinger-like equations, also called the Kohn-Sham equation.

$$H_{\text{eff}}\psi_i(\mathbf{r}) = \left[-\frac{1}{2}\nabla^2 + V_{\text{eff}} \right] \psi_i(\mathbf{r}) = \epsilon_i \psi_i(\mathbf{r}) \quad (2.10)$$

The ground state density is given by,

$$n(\mathbf{r}) = \sum_{i=1}^N |\psi_i(\mathbf{r})|^2 \quad (2.11)$$

where the sum is over the N lowest eigenstates of H_{eff} given in (2.10).

2.2. Approximation of exchange-correlation energy

One of the great challenges in electronic structure calculations is determining the exchange correlation energy E_{xc} because it needs to be approximated.[70] One such approach is the local density approximation (LDA),[74] in which E_{xc} is simply an integral over all space with E_{xc} assumed to be the same as in a homogeneous electron gas. The generalized gradient approximation (GGA)[75] considers functions that modify the behaviour at large gradients in such a way as to preserve desired properties. These methods have been widely used to describe many systems.

However, LDA or GGA methods fail to correctly describe systems like transition metal oxides and rare earth systems, where the electrons are strongly interacting. Introducing a strong intra-atomic interaction in a (screened) Hartree-Fock like manner, or as an on-site adjustment to the LDA or GGA can alleviate this problem. This may be done by including an orbital dependent Hubbard U term that is fitted so as to match a known property.[76]

2.3. Van der Waals (vdW) force

The vdW force is found to be crucial to accurately describe non-bonded interactions such as between molecules or at interfaces. In ALD modelling, we study the reactions of precursors, usually organometallic compounds, with solid surfaces, and thus vdW forces must be treated carefully. Unfortunately, the standard DFT with exchange-correlation functionals (local density approximation [LDA], Perdew-Burke-Ernzerhof [PBE]) does not include

nonlocal vdW interactions, and thus different approaches have been proposed in order to incorporate vdW forces in DFT calculation.[77]

One of the approaches is the addition of empirical, pairwise inter-atomic dispersion corrections of the form $-C_6r^{-6}$, commonly referred to as DFT plus dispersion (DFT-D).[78, 79] In the DFT-D3 method, the total energy is given by[80]

$$E_{DFT-D3} = E_{KS-DFT} - E_{disp} \quad (2.12)$$

Where E_{KS-DFT} is the usual self-consistent Kohn–Sham energy as obtained from the chosen DFT and E_{disp} is the dispersion correction as a sum of two- and three-body energies

$$E_{disp} = E^{(2)} + E^{(3)} \quad (2.13)$$

The most important two-body term is given by,

$$E^{(2)} = \sum_{AB} \sum_{n=6,8,10,\dots} s_n \frac{C_n^{AB}}{r_{AB}^n} f_{d,n}(r_{AB}) \quad (2.14)$$

here the first sum is over all atom pairs in the system, C_n^{AB} denotes the averaged (isotropic) n^{th} -order dispersion coefficient (orders $n = 6, 8, 10, \dots$) for atom pair AB, and r_{AB}^n is their inter-nuclear distance. Damping functions $f_{d,n}$ are used to determine the range of the dispersion correction. Where $s_{r,n}$ is the order-dependent scaling factor of the cutoff radii R_n^{AB} . [81]

$$f_{d,n}(r_{AB}) = \frac{1}{1 + 6 \left(r_{AB} / (s_{r,n} R_n^{AB}) \right)^{-\alpha_n}} \quad (2.15)$$

The long-range part of the interaction between three ground-state atoms can be obtained by applying the concept of short-range damping analogously as for the pairwise term,

$$E^{(3)} = \sum_{ABC} f_{d,3}(\bar{r}_{ABC}) E^{ABC} \quad (2.16)$$

where the sum is over all atom triples ABC in the system and geometrically averaged radii \bar{r}_{ABC} is used as a damping function. The triple-dipole dispersion term E^{ABC} is

$$E^{ABC} = \frac{C_9^{ABC} (3 \cos \theta_\alpha \cos \theta_b \cos \theta_c + 1)}{(r_{AB} r_{BC} r_{CA})^3} \quad (2.17)$$

Where θ_α , θ_b and θ_c are the internal angles of the triangle formed by r_{AB} , r_{BC} and r_{CA} and C_9^{ABC} is the triple-dipole constant which can be found in ref [80]. Another promising method to include the vdW interaction in DFT is the nonlocal vdW density functional (vdW-DF) by Langreth and Lundqvist and co-workers[82] which is implemented in the VASP code.[83, 84] In vdW-DF the non-local correlation is calculated in that the exchange-correlation energy takes the form

$$E_{xc} = E_x^{GGA} + E_c^{LDA} + E_c^{nl} \quad (2.18)$$

where E_x^{GGA} is the GGA exchange energy. E_c^{LDA} Accounts for the local correlation energy obtained within the local density approximation (LDA) and E_c^{nl} is the non- local correlation energy. E_c^{nl} is exact at long distances between separated fragments,

$$E_c^{nl} = \int_0^\infty \frac{du}{2\pi} \text{tr}[\ln(1 - V\bar{\chi}) - \ln \epsilon] \quad (2.19)$$

where $\bar{\chi}$ is the density response to a fully self-consistent potential with long-range, inter-fragment spectator contributions omitted. V is the inter-electronic Coulomb interaction, ϵ is an appropriately approximated dielectric function, and u is the imaginary frequency.

We use these and similar methods for treating the vdW interaction along with the pure DFT method to identify the role of vdW forces on precursor adsorption on TiN surfaces during ALD of W, which will be explained in more detail in Chapter 3-5.

2.4. Bader charge

Electronic charges in molecules and solids are not observables and, therefore, not defined by quantum chemical theory. Many different schemes to assign electronic charge distributed in space to a certain ion. An approach that

focused on charge density has been proposed by Bader.[85] In this approach, space is divided into regions by surfaces that run through minima in the charge density. More precisely, at a point on a dividing surface the gradient of the electron density has no component normal to the surface, which is called Bader regions.[86] Henkelman et al. proposed an algorithm to calculate the charges on atoms based on Bader's theory.[86, 87] In their algorithm, each point on a regular (x,y,z) grid is assigned to one of the regions by following a steepest ascent path on the grid.

2.5. Bibliography

- [1] M. R. M, *Electronic Structure: Basic Theory and Practical Methods*. Cambridge University Press, 2004.
- [2] A. M. a. A. P. Wills J, *Full-Potential Electronic Structure Method*. Springer, 2010.
- [3] P. Hohenberg and W. Kohn, "Inhomogeneous Electron Gas," *Physical Review*, vol. 136, no. 3B, pp. B864-B871, 11/09/ 1964.
- [4] W. Kohn and L. J. Sham, "Self-Consistent Equations Including Exchange and Correlation Effects," *Physical Review*, vol. 140, no. 4A, pp. A1133-A1138, 11/15/ 1965.
- [5] U. v. Barth and L. Hedin, "A local exchange-correlation potential for the spin polarized case. i," *Journal of Physics C: Solid State Physics*, vol. 5, no. 13, p. 1629, 1972.
- [6] J. P. Perdew, K. Burke, and M. Ernzerhof, "Generalized gradient approximation made simple," *Physical Review Letters*, vol. 77, no. 18, pp. 3865-3868, Oct 28 1996.
- [7] I. A. Vladimir, F. Aryasetiawan, and A. I. Lichtenstein, "First-principles calculations of the electronic structure and spectra of strongly correlated systems: the LDA + U method," *Journal of Physics: Condensed Matter*, vol. 9, no. 4, p. 767, 1997.
- [8] A. Tkatchenko, L. Romaner, O. T. Hofmann, E. Zojer, C. Ambrosch-Draxl, and M. Scheffler, "Van der Waals Interactions Between Organic Adsorbates and at Organic/Inorganic Interfaces," *MRS Bulletin*, vol. 35, no. 6, pp. 435-442, 2010.
- [9] S. Grimme, "Semiempirical GGA-type density functional constructed with a long-range dispersion correction," *Journal of Computational Chemistry*, vol. 27, no. 15, pp. 1787-1799, 2006.
- [10] S. Grimme, "Density functional theory with London dispersion corrections," *Wiley Interdisciplinary Reviews: Computational Molecular Science*, vol. 1, no. 2, pp. 211-228, 2011.
- [11] S. Grimme, J. Antony, S. Ehrlich, and H. Krieg, "A consistent and accurate ab initio parametrization of density functional dispersion correction (DFT-D) for the 94 elements H-Pu," *The Journal of Chemical Physics*, vol. 132, no. 15, p. 154104, 2010.
- [12] P. Jurečka, J. Černý, P. Hobza, and D. R. Salahub, "Density functional theory augmented with an empirical dispersion term. Interaction

- energies and geometries of 80 noncovalent complexes compared with ab initio quantum mechanics calculations," *Journal of Computational Chemistry*, vol. 28, no. 2, pp. 555-569, 2007.
- [13] M. Dion, H. Rydberg, E. Schröder, D. C. Langreth, and B. I. Lundqvist, "Van der Waals Density Functional for General Geometries," *Physical Review Letters*, vol. 92, no. 24, p. 246401, 06/16/ 2004.
- [14] K. Jiří, R. B. David, and M. Angelos, "Chemical accuracy for the van der Waals density functional," *Journal of Physics: Condensed Matter*, vol. 22, no. 2, p. 022201, 2010.
- [15] J. Klimeš, D. R. Bowler, and A. Michaelides, "Van der Waals density functionals applied to solids," *Physical Review B*, vol. 83, no. 19, p. 195131, 05/25/ 2011.
- [16] R. F. W. Bader, *Atoms in Molecules: A Quantum Theory*. Clarendon Press, 1994.
- [17] G. Henkelman, A. Arnaldsson, and H. Jónsson, "A fast and robust algorithm for Bader decomposition of charge density," *Computational Materials Science*, vol. 36, no. 3, pp. 354-360, 2006/06/01/ 2006.
- [18] E. Sanville, S. D. Kenny, R. Smith, and G. Henkelman, "Improved grid-based algorithm for Bader charge allocation," *Journal of Computational Chemistry*, vol. 28, no. 5, pp. 899-908, 2007.

Chapter 3. Dissociative reaction of B_2H_6 on TiN surfaces during atomic layer deposition

3.1. Introduction

As thin film deposition techniques have advanced following the Moore's Law for decades, increasingly smaller sizes and higher aspect ratios (AR) for improving the device performance have required highly uniform and conformal films.[1] Nitride materials, such as silicon nitride, titanium nitride, have been deposited using conventional deposition techniques such as plasma-enhanced chemical vapor deposition (PECVD)[2,3], and low-pressure chemical vapor deposition (LPCVD)[4,5]. However, the down-scaling of memory devices has required another deposition technique such as atomic layer deposition (ALD)[6-8] to resolve the step coverage issues of highly integrated devices. As a thin film deposition process, ALD is the most prevalent method due to the demand for excellent step coverage and conformality of deposited thin films. The ALD processes use well-controlled sequential surface reactions to obtain uniform and conformal films.[9,10]

Tungsten (W) is a good material for use as a metal gate with low resistivity in memory devices.[11] A thin film of W can be deposited using ALD by alternatively exposing W precursors such as WF_6 and reducing agents such as disilane (Si_2H_6) or diborane (B_2H_6). First, the successful deposition of W via ALD has been carried out using tungsten hexafluoride (WF_6) and Si_2H_6 in an ABAB... sequence. It was reported that the Si_2H_6 reactant could play only a sacrificial role to remove residual fluorine (F) from

the surface.[12] Later, the ALD W process using B_2H_6 and silane precursors was also intensively investigated.[12,13] Recently, the comparative study of ALD W using two different precursors, SiH_4 and B_2H_6 , was reported by Guilei Wang et al.[14] They concluded that ALD W films using B_2H_6 showed much lower residual F content and a lower resistivity than those using SiH_4 , and a better ALD W film as a gate filling metal could be obtained. These ALD W films have been typically utilized as nucleation layers for a metal gate in memory devices before the deposition of the bulk CVD-W film.[15-17]

Despite much effort in improving ALD W processes, as memory devices become smaller and smaller, the limitation of conformality at ultrahigh aspect ratio (UHAR) contact can induce potential problems such as a seam or void in the final W-plug, leading to an increase in contact resistance.[18,19] Further downscaling the memory devices necessitates the theoretical comprehension of the ALD W process due to the experimentally limited observations on the sub-nanometer scale. Although a few experimental studies on ALD W have been investigated, there has been no theoretical report on the reactivity of B_2H_6 .

In this study, we investigated the reactivity of B_2H_6 with three different TiN surfaces using first principles study based on density functional theory (DFT) calculation to explore the reaction mechanism of the underlying TiN layers during the B_2H_6 dosing process in the ALD W deposition because the underlying surfaces can have significant effects on the characteristics of the subsequent W nucleation layers.[15,20] TiN films have been widely used as a glue/barrier layer for subsequent W nucleation.[21] Although transition metal nitrides always have a problem of oxidation at elevated

temperatures[22], TiN film used in fabrication process of a memory device does not exposed to the oxidation W film is deposited right after deposition of TiN films in ALD process under vacuum system. Three different planes of TiN surfaces, TiN (001), Ti-terminated TiN (111), and N-terminated TiN (111) were taken into account because poly-crystalline TiN layers with (001) and (111) preferred orientations were mainly observed in deposition of TiN films as shown in **Figure 3.1**. [23-25] The decomposition reaction pathways and reaction energetics on three different TiN surfaces were investigated. It is expected that comparative analysis of the reaction mechanism of B_2H_6 with different TiN surfaces would give us insight into how important the underlying TiN surfaces could be for improving the quality of the subsequent W layer during the B_2H_6 dosing process in ALD W deposition.

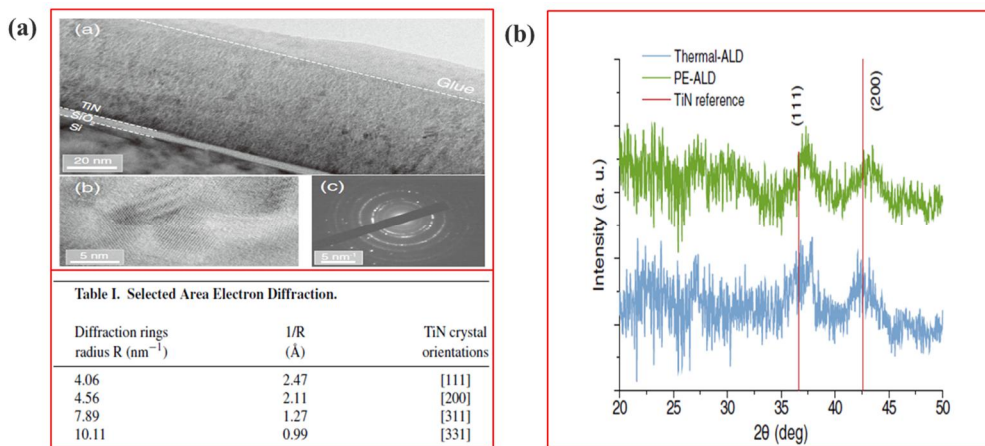


Figure 3.1. (a) TEM micrograph and selected area electron diffraction of a TiN film grown at 250 °C on Si/SiO₂ wafer. (b) X-ray diffractograms of polycrystalline TiN thin films grown either by thermal (a) or plasma-enhanced (b) ALD at T=250 and 200 °C, respectively (N=500 cycles). The vertical red lines indicate the TiN reference diffraction angle.[25]

3.2. Computational methods

In our theoretical results, all DFT calculations were performed using Vienna ab initio simulation package (VASP) program with the Perdew-Burke-Ernzerhof (PBE) functional in the generalized gradient approximation (GGA).[26,27] TiN (001) and TiN (111) surfaces with B1-NaCl structure were used as the reactive surfaces with the B_2H_6 precursor. The optimized lattice parameter of TiN was $a_0 = 4.21 \text{ \AA}$, which is in good agreement with the experimental value ($a_0 = 4.24 \text{ \AA}$).[28] For the TiN (001) surface, a 4-layer slab of (2 x 2) supercell was considered. For comparison, the TiN surfaces with Ti-terminated and N-terminated (111) orientations were considered with a 5-layer slab of (2 x 2) supercell. For all TiN surfaces, such as TiN (001), Ti-terminated TiN (111), and N-terminated TiN (111), vacuum gaps with values of 23.7 \AA , 25.4 \AA , and 25.6 \AA , respectively, in the z direction were included to avoid interactions between adjacent slabs as shown in **Figure 3.2**.

Valence orbitals were described by a plane-wave basis set with the cutoff energy of 400 eV. Electronic energies were calculated with a self-consistent-field (SCF) tolerance of 10^{-4} eV. Ultrasoft Vanderbilt-type pseudopotentials[29] were used to describe the interactions between ions and electrons. A $3 \times 3 \times 3$ Monkhorst k-point mesh for bulk TiN was chosen to ensure that the total energies converged within 1 meV per formula unit. The Brillouin zone for three different TiN surfaces was sampled with a $3 \times 3 \times 1$ Monkhorst-Pack k-point mesh. Geometry optimization was performed by minimizing the forces of all atoms to less than 0.02 eV/ \AA . In addition, we have calculated total energies for various configurations to determine the energy barrier for dissociative adsorption of B_2H_6 on the TiN surfaces.

To optimize adsorption structures, we considered three orientations and three positions of B₂H₆ on the three different TiN surfaces. The detailed structures of adsorption, transition, and reaction state of B₂H₆ on three different TiN surfaces can be explained as follows. The adsorption energy (E_{ads}) was calculated using

$$E_{\text{ads}} = E_{\text{tot,ads}} - (E_{\text{surf}} + E_{\text{pre}})$$

where E_{tot,ads}, E_{surf}, and E_{pre} are the total energy of the system after adsorption, and the energy of the surface only and the energy of the precursor only, respectively. The activation energy (E_a) was calculated using

$$E_a = E_{\text{tot,tran}} - E_{\text{tot,b.tr}}$$

where E_{tot,tran} and E_{tot,ads} are the total energy of the transition state and the total energy before transition, respectively. The reaction energy (E_{rxn}) was calculated using

$$E_{\text{rxn}} = E_{\text{tot,a.tr}} - E_{\text{tot,b.tr}}$$

where E_{tot,a.tr}, and E_{tot,b.tr} are the total energies of the system after transition and after transition, respectively.

We considered three orientations and three positions of B₂H₆ above the TiN (001), Ti-terminated TiN (111), and N-terminated (111) TiN surfaces as shown in **Figures 3.3-3.5**. As for the three orientations, first one is that the B-B bond of the precursor was vertical to the surface. Second one is that the B-B bond of one was horizontal to the surface with two hydrogen atoms facing towards the surface, and third one is that the B-B bond of one was horizontal to the surface with only one hydrogen is facing towards the surface. Also, three different positions were considered on the surface:

For TiN (001) surface, (1) Ti site, (2) Hollow site, (3) N site

For Ti-terminated TiN (111) surface, (1) Ti site (2) N site, (3) Hollow site

For N-terminated TiN (111) surface, (1) N site (2) Ti site, (3) Hollow site

The adsorption energies of B_2H_6 precursor calculated on three different TiN surfaces for each orientation and position were summarized in **Table 3.1-3.3**.

To calculate the transition state, the distance between the two dissociative atoms is slightly separated, and energy relaxation is performed with the constrained distance. The same procedures are carried out until the force between two dissociative atoms becomes almost zero at the saddle point of energy.

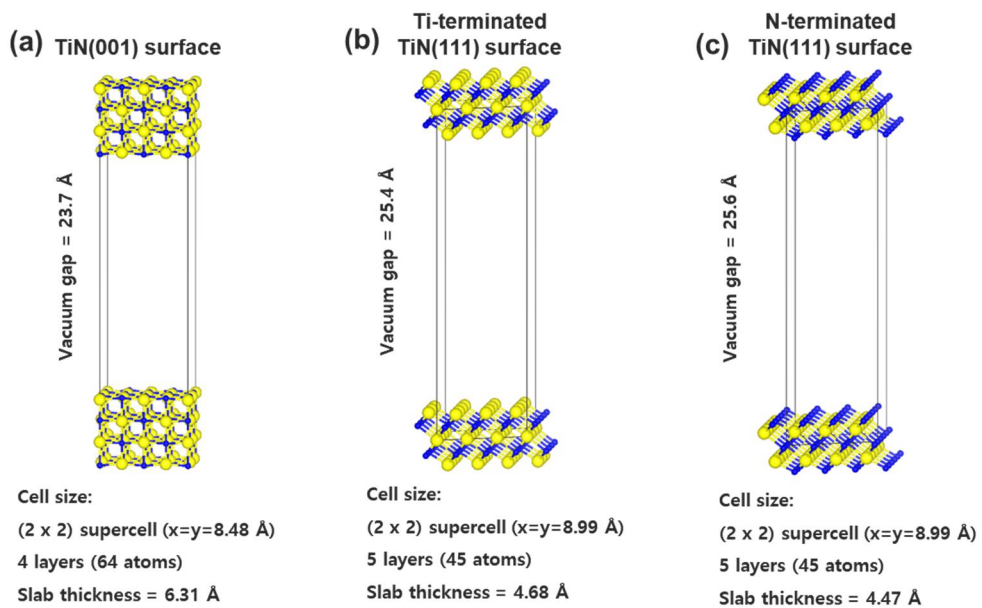


Figure 3.2. Slab model of (a) TiN(001) (b) Ti-terminated TiN(111) (c) N-terminated TiN(111) surfaces.

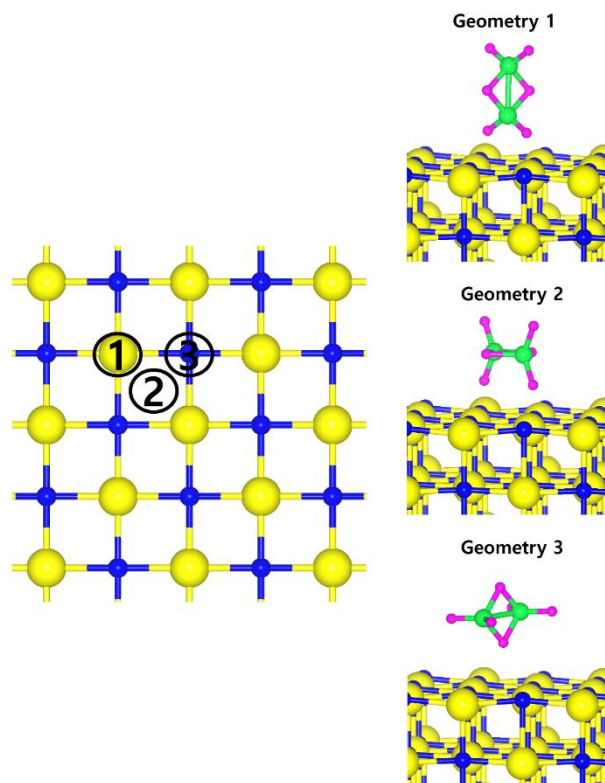


Figure 3.3. Three orientations and three positions of B_2H_6 on the TiN (001) surface.

Geometry	Position	E_{ads} (eV)
1	1	-0.0261
1	2	0.0554
1	3	0.0477
2	1	-0.0573
2	2	-0.0098
2	3	0.0449
3	1	-0.0057
3	2	-0.0077
3	3	-0.0624

Table 3.1. The adsorption energies of B_2H_6 calculated on the TiN (001) surface for each orientation and position.

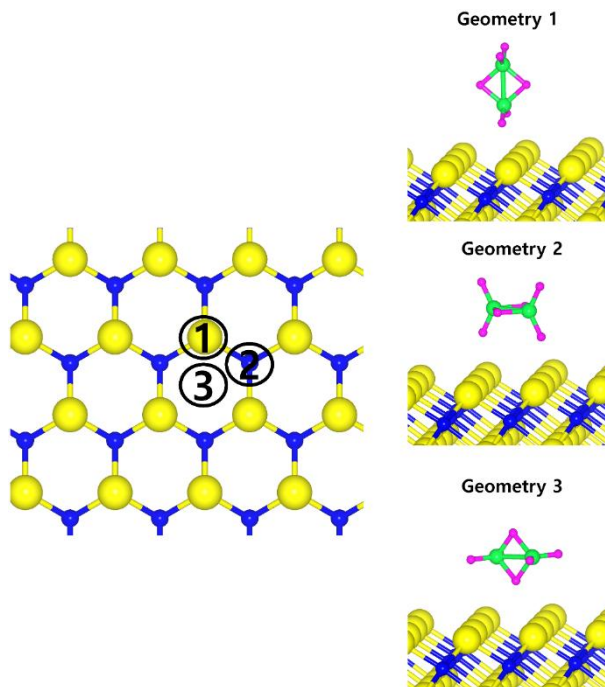


Figure 3.4. Three orientations and three positions of B_2H_6 on the Ti-terminated TiN (111) surface.

Geometry	Position	E_{ads} (eV)
1	1	-0.0112
1	2	0.0086
1	3	0.0113
2	1	-0.0366
2	2	0.0160
2	3	0.0200
3	1	0.2217
3	2	-2.3147
3	3	-4.46

Table 3.2. The adsorption energies of B_2H_6 calculated on the Ti-terminated TiN (111) surface for each orientation and position.

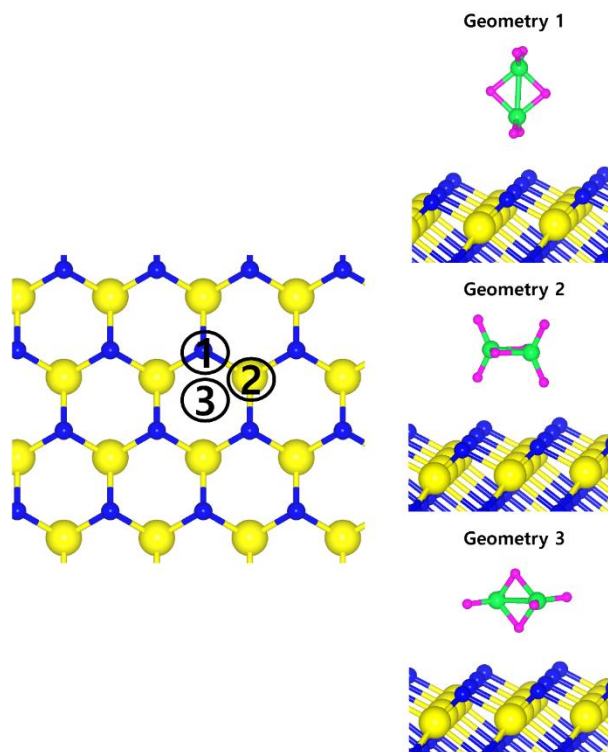


Figure 3.5. Three orientations and three positions of B_2H_6 on the N-terminated TiN (111) surface.

Geometry	Position	E ads (eV)
1	1	0.0108
1	2	-0.0162
1	3	-0.0146
2	1	-0.0202
2	2	-0.0193
2	3	-0.0176
3	1	-0.0080
3	2	-0.0113
3	3	-0.0259

Table 3.3. The adsorption energies of B_2H_6 calculated on the N-terminated TiN (111) surface for each orientation and position.

3.3. Results and discussion

3.3.1. Dissociative reaction of B₂H₆ on TiN(001) surface

Figure 3.6 shows the optimized structures for the B₂H₆ reaction pathway of B-B dissociation on the TiN (001) surface. The optimized structure with the lowest adsorption energy of B₂H₆ on the surface is displayed in **Figure 3.6 (a)**. As shown in **Figure 3.6 (c)**, it was found that borane (BH₃) molecules dissociated from B₂H₆ favorably react with nitrogen atoms on the TiN (001) surface after B-B dissociation due to stronger B-N bonding nature than B-Ti bonding. As shown in **Figure 3.7**, the reaction energy is -1.89 eV, which means that the reaction is exothermic and energetically favorable. The activation energy from **Figure 3.6a-c** is 1.11 eV, and the transition state is shown in **Figure 3.6b** with no obvious surface reconstruction during the reaction. Generally, if any surface reconstruction is occurred during the reaction, activation and reaction energy can be smaller. However, no obvious surface reconstruction was not found for all surfaces used in this study.

To complete the overall reaction energetics of B₂H₆, the calculated energy diagram of B₂H₆ decomposition on the TiN (001) surface is displayed in **Figure 3.7**. The detailed structures of B₂H₆ during the overall reaction pathway on the TiN (001) surface for transition state calculations can be found in **Figure 3.8 and Table 3.4**. During the reaction of the B₂H₆ precursor on the TiN (001) surface, this calculation shows that the overall reaction process is endothermic, with a calculated overall reaction energy of 2.36 eV. These results indicate that the reaction is thermodynamically unfavorable. Furthermore, B₂H₆ dissociative chemisorption on TiN (001) is kinetically

difficult due to high activation energies that range from a minimum of 1.11 eV to a maximum of 1.83 eV. The low reactivity of B_2H_6 with the TiN (001) surface might be attributed to the presence of only one dangling bond per atom on the surface.

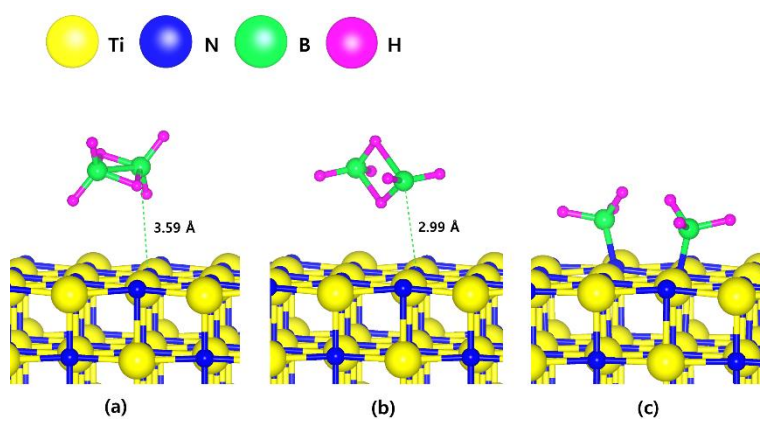


Figure 3.6. The optimized structures for (a) adsorption state, (b) transition state and (c) reaction state of a B_2H_6 on the TiN (001) surface.

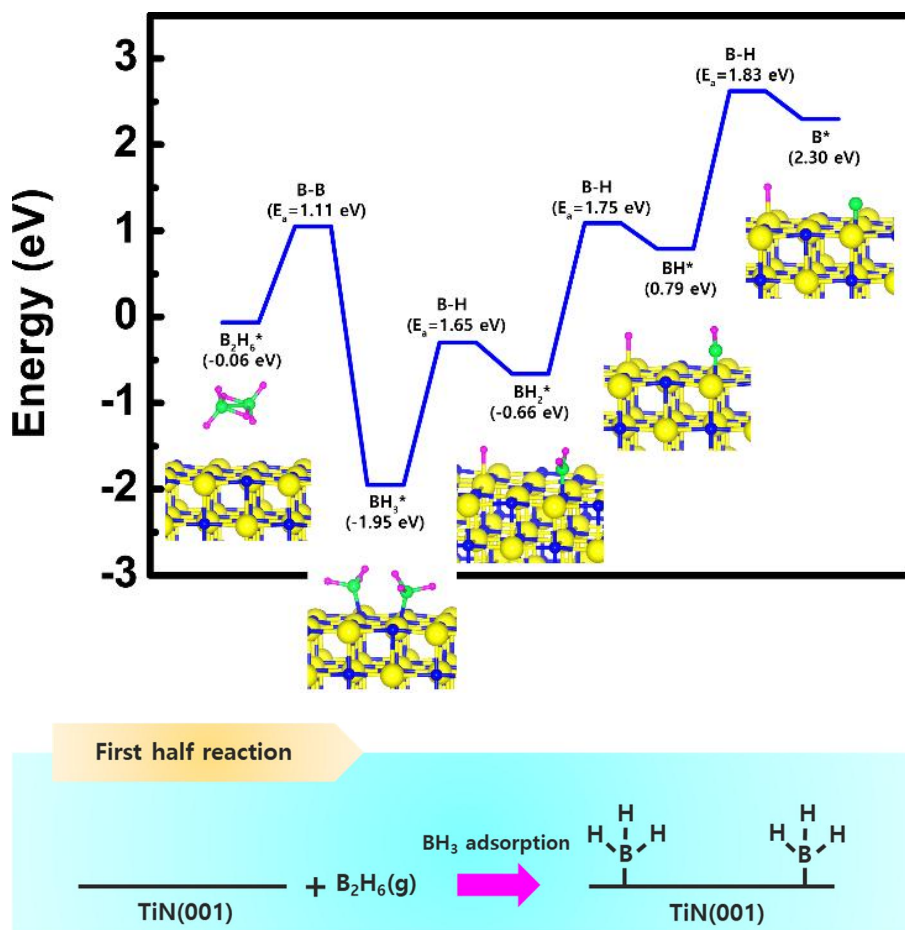


Figure 3.7. Calculated energy diagram of B_2H_6 decomposition on the TiN (001) surface.

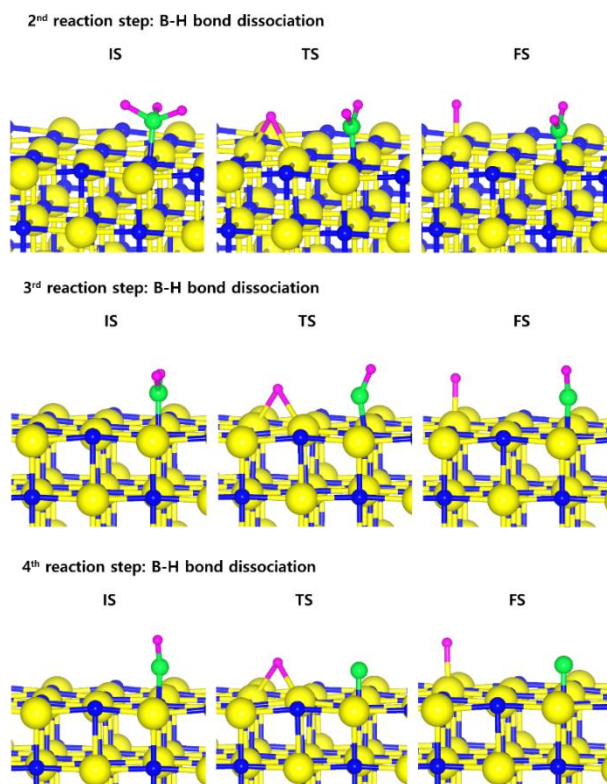


Figure 3.8. Calculated energy diagram of B_2H_6 decomposition on the TiN (001) surface.

Reaction step	Bond dissociation	E_a (eV)	E_{rxn} (eV)
step 1	B-B	1.11	-1.89
step 2	B-H	1.65	1.29
step 3	B-H	1.75	1.45
step 4	B-H	1.83	1.51

Table 3.4. Activation energies (E_a , eV) and reaction energies (E_{rxn} , eV) of B_2H_6 dissociation on the TiN (001) surface.

3.3.2. Dissociative reaction of B₂H₆ on Ti-terminated TiN(111) surface

The decomposition mechanism of B₂H₆ was also studied on the Ti-terminated TiN (111) surface to estimate the difference between TiN (001) and TiN (111) surfaces. The adsorption and reaction of B₂H₆ on the Ti-terminated TiN (111) surface are shown in **Figure 3.9 (a)** and **Figure 3.9 (c)** with the transition state shown in **Figure 3.9 (b)**. As shown in **Figure 3.9 (c)**, it was found that dissociated BH₃ molecules were adsorbed on the hollow site made by three Ti atoms. (Site number 3 in **Figure 3.4**). In **Figure 3.10**, the lowest adsorption energy of B₂H₆ on the Ti-terminated TiN surface is -4.46 eV, showing that the adsorption is energetically favorable. However, the reaction energy is 0.36 eV, indicating that the reaction is endothermic. The activation energy from **Figure 3.9 (a)-(c)** is 0.74 eV with the transition state in **Figure 3.9 (b)**, and no obvious surface reconstruction was found during the reaction. There are three more B-H bond breaking steps after a B-B bond breaking step, as shown in **Figure 3.11** and **Table 3.5**.

The entire energy diagram for the B₂H₆ decomposition on Ti-terminated TiN (111) is illustrated in **Figure 3.10**, which differs with the diagram for TiN (001) in **Figure 3.7**. It demonstrates that both B-B and B-H bond dissociation steps on the Ti-terminated TiN (111) surfaces are more facile than the TiN (001) surface due to smaller activation energies of dissociation on the Ti-terminated TiN (111) surface. Moreover, the overall reaction of B₂H₆ is exothermic, with an overall reaction energy of -0.88 eV. These results show that the reaction is energetically favorable. The high reactivity of B₂H₆ on the Ti-terminated TiN (111) surface may be because the

surface has triple dangling bonds per atom, which make the surface even more reactive than the TiN (001) surface. To be more specific, the number of dangling bonds on the Ti-terminated TiN (111) surface is more than that of the TiN (001), so that B₂H₆ dissociative reaction is more favorable on the former. This analysis is confirmed by higher adsorption of both B and H atoms on Ti-terminated TiN (111) surface than the TiN (001) surface as shown in **Table 3.7**. The aforementioned reasons, this surface can also reduce the energy barriers of the B₂H₆ decomposition as compared to the TiN (001) surface. The activation energies for dissociation of B₂H₆, BH₃, and BH₂ are 0.74, 0.07 and 0.61 eV, respectively, which are lower than that of BH (0.93 eV). This implies that the B-H bond dissociation of BH is the rate-determining step along the overall reaction.

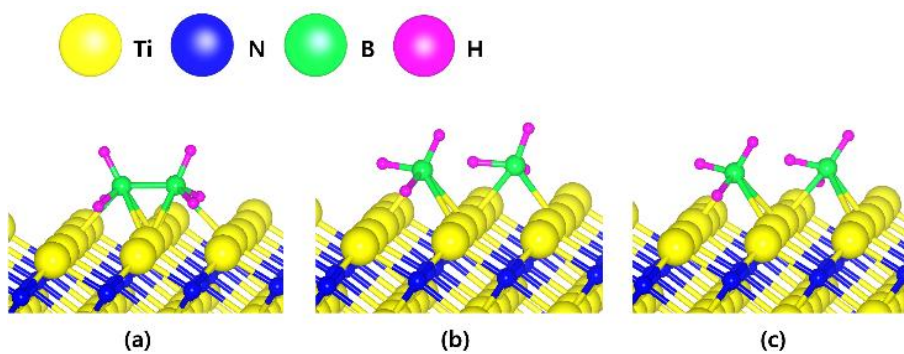


Figure 3.9. The optimized structures for (a) adsorption state, (b) transition state and (c) reaction state of a B_2H_6 on the Ti-terminated TiN (111) surface.

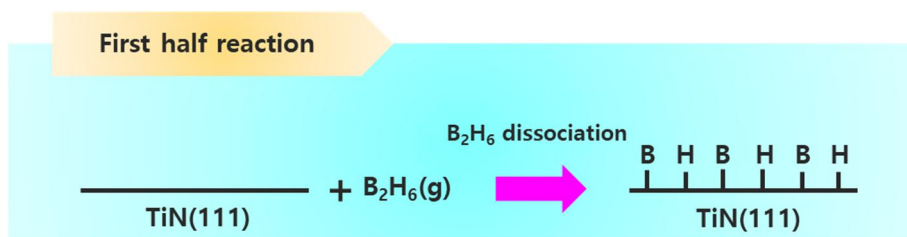
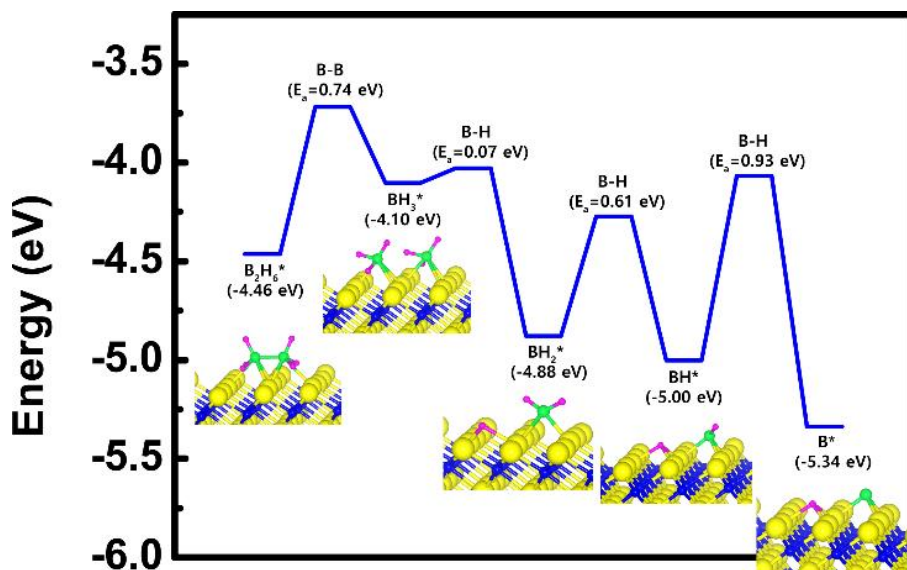


Figure 3.10. Calculated energy diagram of B_2H_6 decomposition on the Ti-terminated TiN (111) surface.

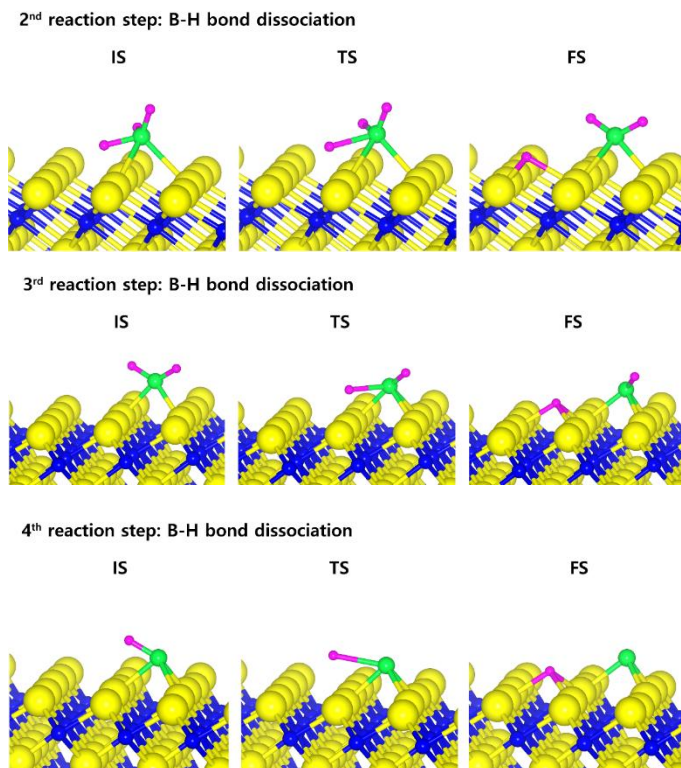


Figure 3.11. Initial (IS), transition (TS), and final (FS) states of intermediate reactions from the 2nd reaction step to the 4th reaction step for the Ti-terminated TiN (111) surface.

Reaction step	Bond dissociation	E_a (eV)	E_{rxn} (eV)
step 1	B-B	0.74	0.36
step 2	B-H	0.07	-0.78
step 3	B-H	0.61	-0.12
step 4	B-H	0.93	-0.34

Table 3.5. Activation energies (E_a , eV) and reaction energies (E_{rxn} , eV) of B_2H_6 dissociation on the Ti-terminated TiN (111) surface.

3.3.3. Dissociative reaction of B₂H₆ on N-terminated TiN(111) surface

The optimized structures for the adsorption, transition state and reaction of B₂H₆ on the N-terminated TiN (111) surface are depicted in **Figure 3.12**. **Figure 3.12 (c)** shows that both B-B and B-H bond dissociation occur simultaneously during the energy relaxation procedure of the reaction state. In addition, hydrogen molecule (H₂) desorption also occurs because two H atoms of B₂H₆ meet each other at the position away from preferentially adsorbed BH_x species with higher binding energy.

As a result, the remaining species with boron on the surface are BH and BH₂. The lowest energies for adsorption and reaction are -0.03 eV and -7.17 eV with a low energy barrier of 0.39 eV. No obvious surface reconstruction was found during the reaction. There are two more B-H bond breaking steps after the first bond breaking step, as depicted in **Figure 3.14** and **Table 3.6**. These results show that three sequential B-H bond breaking steps occur and leave the B atom bound to three N atoms as shown in **Figure 3.14**.

The mechanism of B₂H₆ decomposition was also studied on the N-terminated TiN (111) surface to estimate the differences with the previously described TiN surfaces. **Figure 3.13** shows the entire energy diagram for the B₂H₆ decomposition on N-terminated TiN (111). We found that both B-B and B-H bond breaking on the N-terminated TiN (111) surfaces were much more facile than those of both TiN (001) and Ti-terminated TiN (111) surfaces, as shown in **Figure 3.7** and **Figure 3.10**. This result is primarily because the binding energies of B and H atoms on the N-terminated TiN (111) surface are

the highest among the three different TiN surfaces, as shown in **Table 3.7**. Furthermore, the decomposition of B_2H_6 on the surface is energetically favorable due to the downhill reactions and B-H bond breaking with very small barrier. Rather than H atoms, B adatoms would be preferably supplied by B_2H_6 to form the first monolayer during the B_2H_6 dosing process in the ALD W deposition due to the much higher binding energy of B on the surface, as shown in **Table 3.7**. In the next ALD cycle, WF_6 precursor is commonly used for W deposition. A BF_3 desorption process would occur on the surface because boron adatoms would react with the F atoms of WF_6 , therefore, a uniform W film could be deposited. Our results indicate that a specific TiN surface, such as N-terminated TiN (111), plays an important role in improving the properties of the subsequent W nucleation layers during the W ALD process.

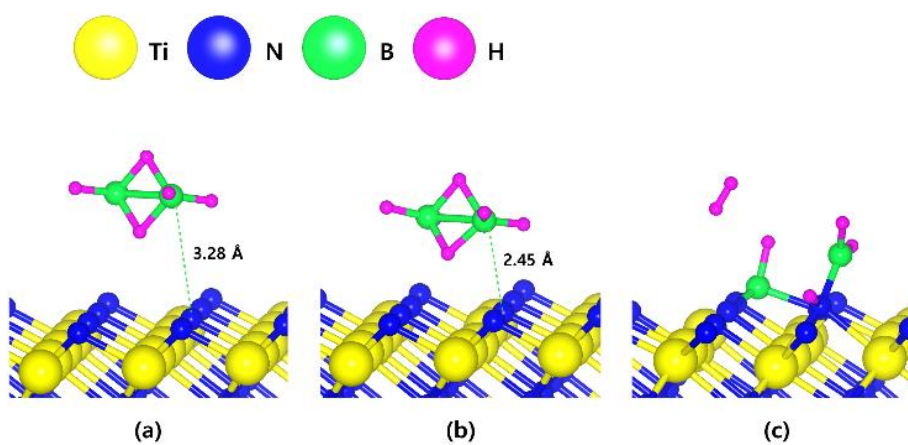


Figure 3.12. The optimized structures for (a) adsorption state, (b) transition state and (c) reaction state of a B_2H_6 on the N-terminated TiN (111) surface.

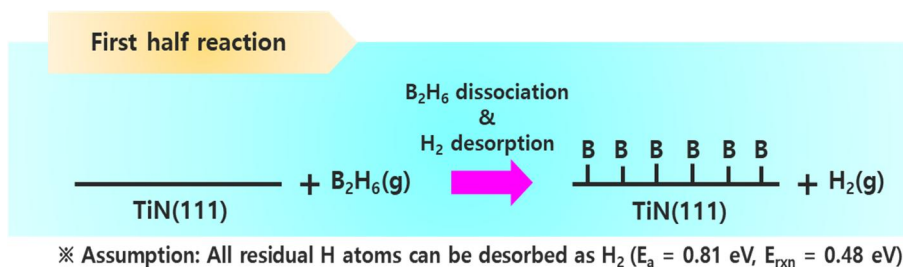
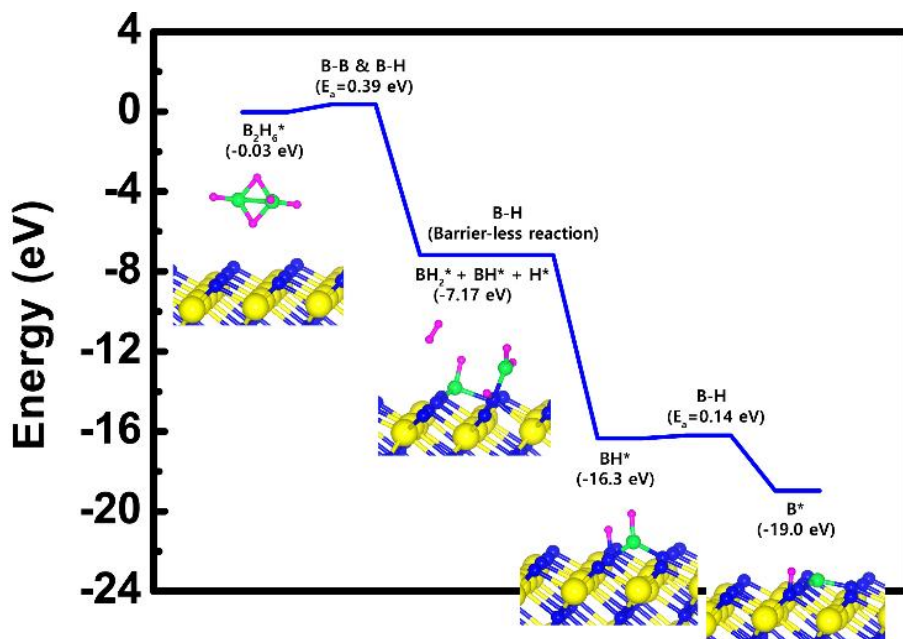


Figure 3.13. Calculated energy diagram of B_2H_6 decomposition on the N-terminated TiN (111) surface.

3.3.4. Discussions

According to the above results, the N-terminated TiN (111) surface is the most efficient in depositing boron-containing layer during the B_2H_6 dosing process in ALD W deposition. The TiN (001) surface is unfavorable to deposit W film due to residual BH_3 species on the surface and, corresponds to a reduction in the number of W sites that can be deposited. We suggest that the reason there are critical problems, such as a seam or void, in filling the W metal gate is the difference in deposition rate on three different TiN surfaces (N-terminated TiN (111) is the fastest and TiN (001) is the slowest). Thus, it is necessary to study the control of preferred orientation in TiN surfaces to enhance the W ALD process.

There are several models to explain texture evolution in cubic transition-metal nitrides. Oh and Je proposed that the orientation of polycrystalline TiN films should initially be (001) due to the lowest surface energy, and with increasing thickness, the (111) texture becomes favored due to the lower elastic modulus in the [111] direction.[23,24] The change of the texture in this model is driven by the film/substrate system minimizing the total free energy.

Takeshi Kaizuka et al.[31] later reported that a TiN film of (111) preferred orientation with conformal step coverage could be successfully obtained by pre-deposition of the Ti (001) layer before the CVD TiN film deposition. They said that TiN film with the (111) preferred orientation could be induced due to the lattice matching of the Ti film as shown in **Figure 3.15**. The combination of their results and our results provides insight into how to design the TiN surfaces to improve the properties of the W films during the

W ALD process. Furthermore, Yu You et al.[32] reported that using a laser implemented CVD, it is possible to deposit α -Al₂O₃ at somewhat low temperature as shown in **Figure 3.16**. For this reason, (104) preferred oriented α -3 with hexagonal facet may help to make TiN films (111) oriented.

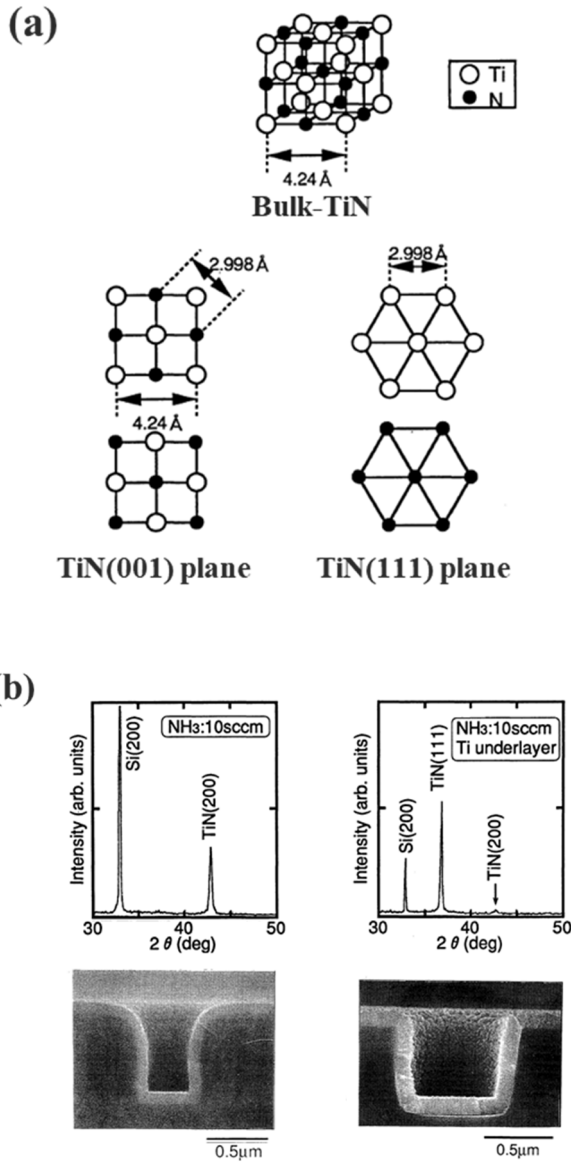


Figure 3.15. (a) Illustrations for modeling of atomic configurations of TiN(002) and TiN(111) (b) XRD patterns and cross-sectional SEM images of CVD TiN films.[31]

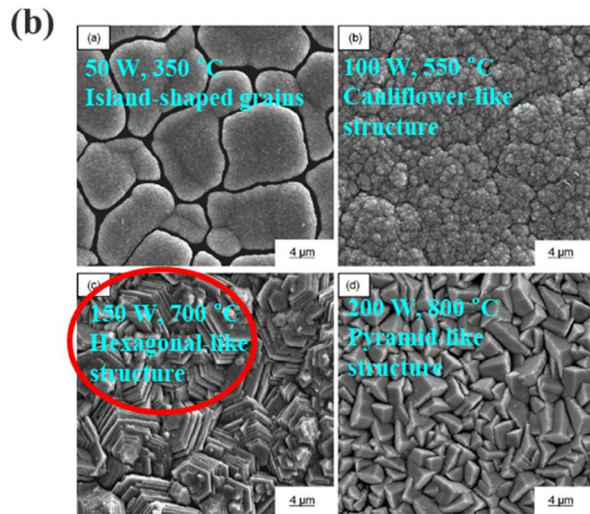
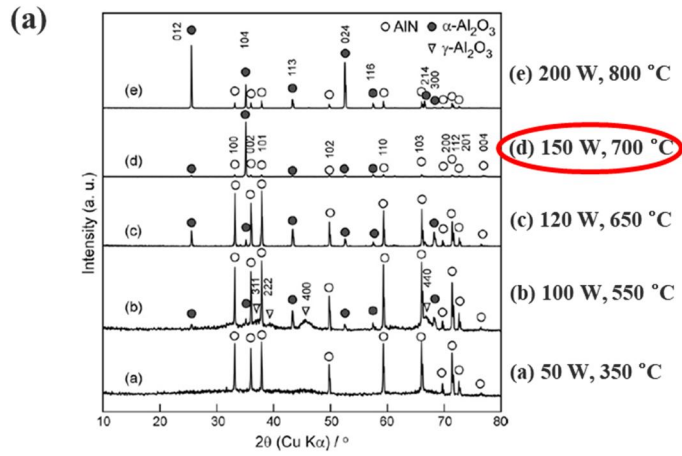


Figure 3.16. (a) XRD patterns of Al₂O₃ films (b) surface SEM images of Al₂O₃ films.[32]

3.4. Summary

We have studied B_2H_6 decomposition on three different TiN surfaces to understand the detailed reaction mechanisms of B_2H_6 during the B_2H_6 dosing process in ALD W deposition. This procedure is essential for depositing dense and conformal W films. In this study, we utilize density functional theory to evaluate the energetics of B_2H_6 decomposition for overall reactions. The overall reactions of the B_2H_6 with the Ti-terminated TiN (111) and N-terminated TiN (111) surfaces are energetically favorable, whereas the overall reaction for the TiN (001) is energetically unfavorable. These differences in energetics come from the difference in binding energies of B and H atoms among three different surfaces. N-terminated TiN (111) shows the lowest overall reaction energy compared with three different surfaces due to the highest binding energy of both B and H atoms with the surface, and corresponds to the most reactive surface. From the understanding of the influence of the TiN surfaces during the B_2H_6 dosing process, the control of the texture of TiN film is required for improvement of the W nucleation layers. These results imply that the understanding of the reactivity of the TiN surfaces gives us insight into improving the W ALD process for future memory devices.

3.5. Bibliography

- [1] S.-B. Baek, D.-H. Kim, and Y.-C. Kim, "Adsorption and surface reaction of bis-diethylaminosilane as a Si precursor on an OH-terminated Si (001) surface," *Applied Surface Science*, vol. 258, no. 17, pp. 6341-6344, 2012/06/15/ 2012.
- [2] N. Sharma, M. Hooda, and S. K. Sharma, "Synthesis and Characterization of LPCVD Polysilicon and Silicon Nitride Thin Films for MEMS Applications," *Journal of Materials*, vol. 2014, p. 8, 2014, Art. no. 954618.
- [3] B. C. Joshi, G. Eranna, D. P. Runthala, B. B. Dixit, O. P. Wadhawan, and P. D. Vyas, *LPCVD and PECVD silicon nitride for microelectronics technology*. 2000, pp. 303-309.
- [4] W. D. Huang *et al.*, "Low temperature PECVD SiNx films applied in OLED packaging," *Materials Science and Engineering B-Solid State Materials for Advanced Technology*, vol. 98, no. 3, pp. 248-254, Apr 15 2003.
- [5] A. El Amrani, A. Bekhtari, B. Mahmoudi, A. Lefgoum, and H. Menari, "Experimental study of the effect of process parameters on plasma-enhanced chemical vapour deposition of silicon nitride film," *Vacuum*, vol. 86, no. 4, pp. 386-390, 2011/11/11/ 2011.
- [6] W.-J. Lee, J.-C. Lee, C. Ook Park, Y.-S. Lee, S.-J. Shin, and S.-K. Rha, *A Comparative Study on the Si Precursors for the Atomic Layer Deposition of Silicon Nitride Thin Films*. 2004, pp. 1352-1355.
- [7] J. W. Klaus, A. W. Ott, A. C. Dillon, and S. M. George, "Atomic layer controlled growth of Si₃N₄ films using sequential surface reactions," *Surface Science*, vol. 418, no. 1, pp. L14-L19, 1998/11/27/ 1998.
- [8] C. A. Murray, S. D. Elliott, D. Hausmann, J. Henri, and A. LaVoie, "Effect of Reaction Mechanism on Precursor Exposure Time in Atomic Layer Deposition of Silicon Oxide and Silicon Nitride," *ACS Applied Materials & Interfaces*, vol. 6, no. 13, pp. 10534-10541, 2014/07/09 2014.
- [9] S. M. George, "Atomic Layer Deposition: An Overview," *Chemical Reviews*, vol. 110, no. 1, pp. 111-131, 2010/01/13 2010.
- [10] S.-J. Won, J. R. Kim, S. Suh, N.-I. Lee, C. S. Hwang, and H. J. Kim, "Effect of Catalyst Layer Density and Growth Temperature in Rapid Atomic Layer Deposition of Silica Using Tris(tert-pentoxy)silanol,"

- ACS Applied Materials & Interfaces*, vol. 3, no. 5, pp. 1633-1639, 2011/05/25 2011.
- [11] S. H. Kim, N. Kwak, J. Kim, and H. Sohn, "A comparative study of the atomic-layer-deposited tungsten thin films as nucleation layers for W-plug deposition," *Journal of the Electrochemical Society*, vol. 153, no. 10, pp. G887-G893, 2006.
- [12] J. W. Klaus, S. J. Ferro, and S. M. George, "Atomic layer deposition of tungsten using sequential surface chemistry with a sacrificial stripping reaction," *Thin Solid Films*, vol. 360, no. 1-2, pp. 145-153, Feb 1 2000.
- [13] T. Luoh, C. T. Su, T. H. Yang, K. C. Chen, and C. Y. Lu, "Advanced tungsten plug process for beyond nanometer technology," *Microelectronic Engineering*, vol. 85, no. 8, pp. 1739-1747, Aug 2008.
- [14] G. L. Wang *et al.*, "Application of Atomic Layer Deposition Tungsten (ALD W) as Gate Filling Metal for 22 nm and Beyond Nodes CMOS Technology," *Ecs Journal of Solid State Science and Technology*, vol. 3, no. 4, pp. P82-P85, 2014.
- [15] S. H. Kim, S. J. Yeom, N. Kwak, and H. Sohn, "Phase and microstructure of ALD-W films deposited using B₂H₆ and WF₆ and their effects on CVD-W growth," *Journal of the Electrochemical Society*, vol. 155, no. 2, pp. D148-D154, 2008.
- [16] S. Smith *et al.*, "Low resistivity tungsten for contact metallization," *Microelectronic Engineering*, vol. 82, no. 3-4, pp. 261-265, Dec 2005.
- [17] S. H. Kim, J. T. Kim, N. Kwak, J. Kim, T. S. Yoon, and H. Sohn, "Effects of phase of underlying W film on chemical vapor deposited-W film growth and applications to contact-plug and bit line processes for memory devices," *Journal of Vacuum Science & Technology B*, vol. 25, no. 5, pp. 1574-1580, Sep-Oct 2007.
- [18] T. Omstead, G. C. D' Couto, S. H. Lee, P. Wongsenakaum, J. Collins, and K. Levy, "Filling high-AR structures using pulsed nucleation layer deposition," *Solid State Technology*, vol. 45, no. 9, pp. 51-+, Sep 2002.
- [19] S. H. Kim *et al.*, "Characterizations of pulsed chemical vapor deposited-tungsten thin films for ultrahigh aspect ratio W-plug process," *Journal of the Electrochemical Society*, vol. 152, no. 6, pp. C408-C417, 2005.
- [20] G. Ramanath *et al.*, "Electromigration in epitaxial Cu (001) lines," in *AIP Conference Proceedings*, 2002, vol. 612, no. 1, pp. 10-20: AIP.

- [21] C. H. Kim, I. C. Rho, S. H. Kim, Y. S. Sohn, H. S. Kang, and H. J. Kim, "Improvement of Adhesion Performances of CVD-W Films Deposited on B₂H₆-Based ALD-W Nucleation Layer," *Electrochemical and Solid State Letters*, vol. 12, no. 3, pp. H80-H83, 2009.
- [22] U. Guler, A. V. Kildishev, A. Boltasseva, and V. M. Shalaev, "Plasmonics on the slope of enlightenment: the role of transition metal nitrides," *Faraday Discussions*, 10.1039/C4FD00208C vol. 178, no. 0, pp. 71-86, 2015.
- [23] U. C. Oh and J. H. Je, "Effects of Strain-Energy on the Preferred Orientation of Tin Thin-Films," *Journal of Applied Physics*, vol. 74, no. 3, pp. 1692-1696, Aug 1 1993.
- [24] J. H. Je, D. Y. Noh, H. K. Kim, and K. S. Liang, "Preferred orientation of TiN films studied by a real time synchrotron x-ray scattering," *Journal of Applied Physics*, vol. 81, no. 9, pp. 6126-6133, May 1 1997.
- [25] L. Assaud, K. Pitzschel, M. Hanbucken, and L. Santinacci, "Highly-Conformal TiN Thin Films Grown by Thermal and Plasma-Enhanced Atomic Layer Deposition," *Ecs Journal of Solid State Science and Technology*, vol. 3, no. 7, pp. P253-P258, 2014.
- [26] J. P. Perdew, K. Burke, and M. Ernzerhof, "Generalized gradient approximation made simple," *Physical Review Letters*, vol. 77, no. 18, pp. 3865-3868, Oct 28 1996.
- [27] G. Kresse and J. Furthmuller, "Efficient iterative schemes for ab initio total-energy calculations using a plane-wave basis set," *Physical Review B*, vol. 54, no. 16, pp. 11169-11186, Oct 15 1996.
- [28] N. Schonberg, "An X-Ray Investigation on Ternary Phases in the Ta-Ti-N, Ta-Cr-N, Ta-Mn-N, Ta-Fe-N, Ta-Co-N, Ta-Ni-N Systems," *Acta Chemica Scandinavica*, vol. 8, no. 2, pp. 213-220, 1954.
- [29] D. Vanderbilt, "Soft self-consistent pseudopotentials in a generalized eigenvalue formalism," *Physical Review B*, vol. 41, no. 11, pp. 7892-7895, 04/15/ 1990.
- [30] G. Henkelman and H. Jónsson, "Improved tangent estimate in the nudged elastic band method for finding minimum energy paths and saddle points," *The Journal of Chemical Physics*, vol. 113, no. 22, pp. 9978-9985, 2000.
- [31] T. Kaizuka, H. Shinriki, N. Takeyasu, and T. Ohta, "Conformal Chemical-Vapor-Deposition Tin(111) Film Formation as an

- Underlayer of Al for Highly Reliable Interconnects," *Japanese Journal of Applied Physics Part 1-Regular Papers Brief Communications & Review Papers*, vol. 33, no. 1b, pp. 470-474, Jan 1994.
- [32] Y. You, A. Ito, R. Tu, and T. Goto, "Low-temperature deposition of α -Al₂O₃ films by laser chemical vapor deposition using a diode laser," *Applied Surface Science*, vol. 256, no. 12, pp. 3906-3911, 2010/04/01/2010.

Chapter 4. Effects of H₂ and N₂ treatment for B₂H₆ dosing process on TiN surfaces during atomic layer deposition

4.1. Introduction

As the demand for miniaturized and highly integrated devices in the electronics industry increases, conformal film deposition techniques that can precisely control thickness at atomic scale are becoming very important[1,2]. Nitride materials, such as titanium nitride, silicon nitride, have been deposited using conventional deposition systems such as low-pressure chemical vapor deposition (LPCVD)[3,4], plasma-enhanced chemical vapor deposition (PECVD)[5,6]. Another deposition technique such as atomic layer deposition (ALD)[7-9] is the most prevalent technique for fabrication of new memory devices due to excellent step coverage and high conformality on extremely high aspect ratio structures. The ALD processes utilize well-controlled sequential surface reactions to achieve uniform and conformal films.[10,11]

As one of the indispensable materials in fabrication of future memory devices, tungsten (W) has been used in metal gate deposition process due to the capability of depositing lower resistive films than other candidate materials, which results in enhancement of device performance.[12,13] In the fabrication of memory devices, tungsten films have most widely been deposited using ALD process by alternatively

exposing W precursors such as tungsten hexafluoride (WF_6) and reducing agents such as diborane (B_2H_6) in an ABAB... sequence. In the ALD W processes, B_2H_6 dosing process plays a critical role in deposition of W films with low resistivity and in removal of residual fluorine (F) atoms on the surface.[14-16] However, since the aspect ratio increases as the size of the memory device becomes smaller, it becomes difficult to deposit a thin film having excellent step coverage and conformality due to a problem that a seam or void is formed in the process of filling the W metal gate. This problem is a major obstacle to the development of future memory devices.[17,18] To tackle this problem, the theoretical comprehension of the ALD W process is required due to the experimentally limited observations on the sub-nanometer scale. During the ALD W process, H_2 and N_2 molecules are used as both a purging gas at the purge time and a dilute gas (5% B_2H_6 + 95% H_2 or N_2) at the B_2H_6 dosing time as shown in **Figure 4.1**[15]. Although a few experimental results on ALD W have been reported, there has been no theoretical report on the effect of H_2 and N_2 treatment used in ALD W process.

In our previous study, we reported that these severe problems, such as seam or void, in filling the W metal gate for memory devices would be attributed to the difference of deposition rate of W film depending on the orientations of TiN surfaces by analyzing dissociation reaction of B_2H_6 on three different TiN surfaces using density functional theory (DFT)[19] calculation method. Since this previous study does not give information on the H_2 and N_2 treatment for B_2H_6 dosing process, we want to report how important the use of proper gas treatment could be for B_2H_6 bond dissociation.

Previous ab initio molecular dynamics (AIMD) simulation results

show that the presence of N vacancies catalyzes N_2 dissociative chemisorption on TiN (001) surface. N_2 dissociation is never observed at defect-free TiN (001) surface.[20] The phenomena were also observed for vanadium nitride (001) surface.[21] D. G. sangiovanni et al. demonstrated that Ti and N adatom diffusion mechanism on TiN (001) involving via direct hopping onto a lower layer and via push-out/exchange by classical molecular dynamics (CMD) and AIMD simulations at temperatures ranging from 1200 to 2400 K.[22-25] They also carried out Ti and N adatom migration pathways on TiN (111) surface and showed that Nad species are considerably more mobile than Tiad on TiN (111), contrary to their previous results on TiN (001) by CMD based on the modified embedded atom method (MEAM) at temperature ranging from 600 to 1800 K.[26] Similar study was also carried out by Yuan Ren et al. showing that diffusion energy of Ti adatom is greater than that of N adatom confirmed by first principles calculation.[27] C. Tholander et al. reported that Ti, Al, and N adatom mobilities on TiN (001), (011) and (111) surfaces, in general, are fastest on TiN (001), slower on (111), slowest on (011).[28]

In this study, we present first-principles study based on DFT calculation to investigate the effects of H_2 and N_2 treatment on TiN surfaces for B_2H_6 dosing process. In the first step, the decomposition processes of H_2 and N_2 treatment on the TiN surface were carefully analyzed. Then, in the second step, the decomposition processes of B_2H_6 molecules on the H_2 - and N_2 - treated TiN surfaces were analyzed to determine H_2 and N_2 treatment effects, respectively. From our calculated results in this study, the structure of TiN surfaces can be changed as the TiN surface is exposed to large amounts of H_2 or N_2 molecules during the B_2H_6 dosing process. As a result, the

changed structure of the TiN surfaces can have a significant impact on the ALD W process because the underlying surfaces can have significant effects on the characteristics of the subsequent W nucleation layers.[29,30] The TiN surfaces have been widely utilized as a glue/barrier layer for subsequent W nucleation.[31] Three different planes of TiN surfaces, TiN (001), Ti-terminated TiN (111), and N-terminated TiN (111) were taken into account because poly-crystalline TiN layers with (001) and (111) preferred orientations were mainly observed in deposition of TiN films.[32,33] The dissociative reaction pathways and reaction energetics of both H₂ and N₂ on three different TiN surfaces were investigated to explore the effect of H₂ and N₂ treatment for B₂H₆ dosing process. It is expected that the comparative analysis of both H₂ and N₂ would give us insight into how important the use of proper gas treatment could be for improving the quality of the subsequent W layer during the W ALD process. This study will help to understand how H₂ and N₂ treatment plays an important role in the B₂H₆ dissociation reaction and ultimately provide new important information for improving the W ALD process.

W ALD deposition process

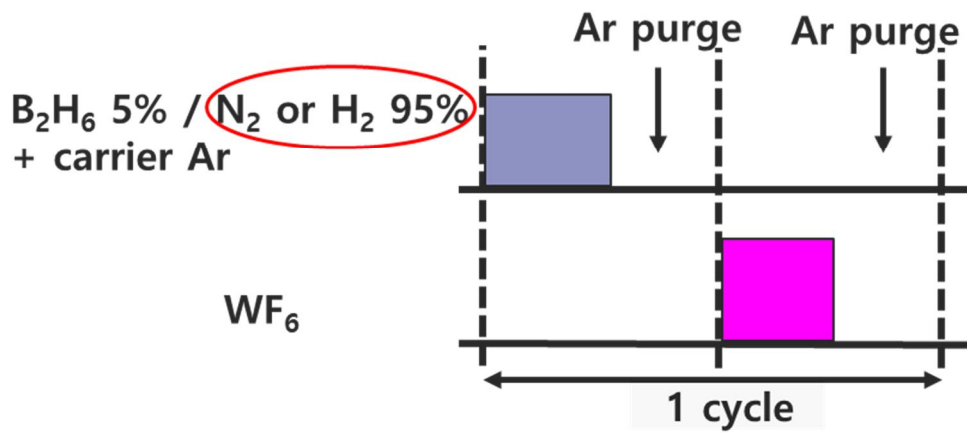


Figure 4.1. Schematic of W ALD deposition process.

4.2. Computational methods

In our theoretical results, all DFT calculations were performed using Vienna ab initio simulation package (VASP) program with the Perdew-Burke-Ernzerhof (PBE) functional in the generalized gradient approximation (GGA).[34,35] We used PBE-D2 functional with a correction to the conventional Kohn-Sham DFT energy to treat the vdW interactions for all TiN surface calculations.[36] Projector augmented wave (PAW) method were used to describe the interaction between valence electrons and ion cores.[37] TiN (001) and TiN (111) surfaces with B1-NaCl structure were used as the reactive surfaces with the B₂H₆ precursor. The optimized lattice parameter of TiN was $a_0 = 4.259 \text{ \AA}$, which overestimate somewhat the experimental value ($a_0 = 4.24 \text{ \AA}$)[38] since generally PBE functionals tend to overestimate the lattice parameters. With compared to our PBE based calculated lattice parameter, previous research papers for DFT calculations of TiN reported that an optimized lattice parameter of TiN using PBE functional is close to 4.254 \AA . [25,39] Another related paper using the Armiento Mattsson (AM05) approximation report yields to 4.220 \AA . [40] For the TiN (001) surface, a 4-layer slab of (2 x 2) supercell with 64 atoms was considered. For comparison, the TiN surfaces with Ti-terminated and N-terminated (111) orientations were considered with a 5-layer slab of (2 x 2) supercell with 45 atoms. For all TiN surfaces, such as TiN (001), Ti-terminated TiN (111), and N-terminated TiN (111), vacuum gaps with values of 23.7 \AA , 25.4 \AA , and 25.6 \AA , respectively, in the z direction were included to avoid interactions between adjacent slabs.

Valence orbitals were described by a plane-wave basis set with the cutoff energy of 400 eV. Electronic energies were calculated with a self-consistent-field (SCF) tolerance of 10^{-4} eV on the total energy. Ultrasoft Vanderbilt-type pseudopotentials[41] were used to describe the interactions between ions and electrons. A $3 \times 3 \times 3$ Monkhorst k-point mesh for bulk TiN was chosen. The Brillouin zone for three different TiN surfaces was sampled with a $3 \times 3 \times 1$ Monkhorst-Pack k-point mesh. Geometry optimization was performed by minimizing the forces of all atoms to less than 0.02 eV/Å with the total energy of the system converged to within 10^{-4} eV during self-consistent iterations. In addition, we have calculated total energies for various configurations to determine the energy barrier for dissociative adsorption of H₂ and N₂ on the TiN surfaces in the first step, and for one of B₂H₆ on H-covered TiN surfaces in the second step.

To optimize adsorption structures, we considered three orientations and three positions of B₂H₆ on the three different TiN surfaces. The detailed structures of adsorption, transition, and reaction state of B₂H₆ on three different TiN surfaces can be explained as follows. The adsorption energy (E_{ads}) was calculated using

$$E_{\text{ads}} = E_{\text{tot,ads}} - (E_{\text{surf}} + E_{\text{pre}})$$

where $E_{\text{tot,ads}}$, E_{surf} , and E_{pre} are the total energy of the system after adsorption, and the energy of the surface only and the energy of the precursor only, respectively. The activation energy (E_{a}) was calculated using

$$E_{\text{a}} = E_{\text{tot,tran}} - E_{\text{tot,b.tr}}$$

where $E_{\text{tot,tran}}$ and $E_{\text{tot,b.tr}}$ are the total energy of the transition state and the total energy before transition, respectively. The reaction energy (E_{rxn}) was calculated using

$$E_{\text{rxn}} = E_{\text{tot,a,tr}} - E_{\text{tot,b,tr}}$$

where $E_{\text{tot,a,tr}}$, and $E_{\text{tot,b,tr}}$ are the total energies of the system after transition and after transition, respectively.

We considered two orientations and three positions of H_2 and N_2 above the TiN (001), Ti-terminated TiN (111), and N-terminated (111) TiN surfaces as shown in **Figures 2-4**. As for the two orientations, first one is that those molecules were vertical to the surface. Second one is that those molecules were horizontal to the surface. Also, three different positions were considered on the surface:

For TiN (001) surface, (1) Ti site, (2) Hollow site, (3) N site

For Ti-terminated TiN (111) surface, (1) Ti site (2) N site, (3) Hollow site

For N-terminated TiN (111) surface, (1) N site (2) Ti site, (3) Hollow site

The adsorption energies of H_2 and N_2 calculated on three different TiN surfaces for each orientation and position were summarized in **Table 1-3**.

In case of geometry 2 in **Figures 2-4**, adsorption positions were selected when one molecule atom is adsorbed on the specific position since almost initial structures with geometry 2 after structural relaxation become final structures that one molecule atom is tilted to the adsorption position. Since final structures for both $\langle 001 \rangle$ and $\langle 110 \rangle$ directions after structural relaxation have almost similar results for both molecular orientations on the same position of TiN and adsorption energies, we chose the word “geometry 2” rather than $\langle 100 \rangle$ or $\langle 110 \rangle$ directions to avoid the use of duplicated values for adsorption energies.

We also checked three orientations and three positions of B_2H_6 above the H-covered Ti-terminated TiN (111), and H-covered N-terminated (111) TiN surfaces as shown in **Figures 5-6**. As for the three orientations, first one

is that the B-B bond of the precursor was vertical to the surface. Second one is that the B-B bond of one was horizontal to the surface with two hydrogen atoms facing towards the surface, and third one is that the B-B bond of one was horizontal to the surface with only one hydrogen is facing towards the surface. Also, three different positions were considered on the surface:

For H-covered Ti-terminated TiN (111) surface, (1) H site (2) Ti site, (3) N site

For H-covered N-terminated TiN (111) surface, (1) H site (2) Ti site, (3) Hollow site

The adsorption energies of B_2H_6 precursor calculated on two different TiN surfaces for each orientation and position were summarized in **Table 4-5**.

To calculate the transition state, the distance between the two dissociative atoms is slightly separated, and energy relaxation is performed with the constrained distance. The same procedures are carried out until the force between two dissociative atoms becomes almost zero at the saddle point of energy.

It is worth noting that PBE-D2 generally results in a well-known and physically understood estimation of the dissociative reactions of molecules on various surfaces. Various computational approaches can be utilized to correct the shortcomings of approximate DFT calculations, including GW corrections[42] or some exact Hartree Fock (HF) exchange in the modern hybrid density functional (B3LYP, PBE0, HSE, etc.)[43-45], which can lead to substantially improved band gaps; however, they are significantly computationally demanding. Since our all DFT calculations are addressed to

bond dissociative reactions of various molecules, we believe it is reasonable and quantitative to investigate the dissociative reactions of various molecules on TiN surfaces using the PBE-D2 theory here. In addition, PBE-D2 predictions have proven useful for prediction of the dissociative reactions of various molecules on different surfaces as shown by the numerous studies dissociation of different large molecules on Au (gold)[46], oxygen reduction reaction on Co(acetylacetonate)₂[47], water dissociation on mackinawite (FeS)[48,49], dissociative reaction of silicon precursor on Si[50].

To calculate the transition state, the distance between the two dissociative atoms is slightly separated, and energy relaxation is performed with the constrained distance. The same procedures are carried out until the force between two dissociative atoms becomes almost zero at the saddle point of energy. This procedure for calculation of transition state is required to find not only the accurate final state but also transition state especially in complicated system, such as B₂H₆ dissociation. During surface relaxation in our DFT calculations, no obvious surface reconstruction was found in different surfaces, such as TiN (001), Ti-terminated TiN (111), N-terminated TiN (111), which has been confirmed in other report[51].

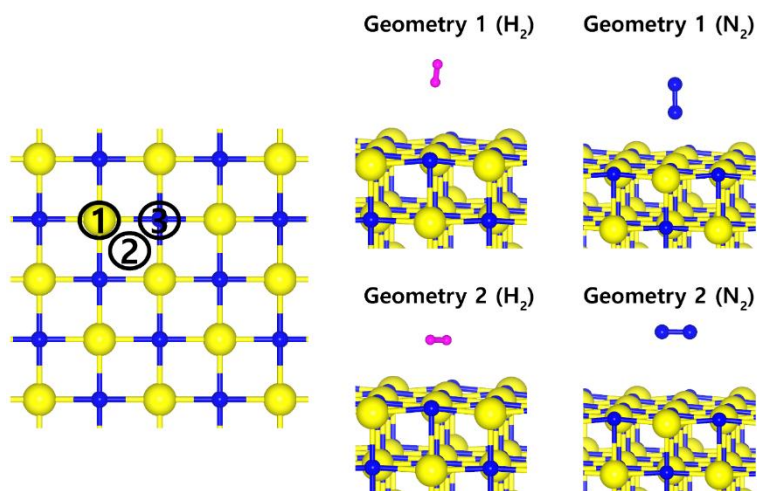


Figure 4.2. Two orientations and three positions of H_2 and N_2 on the TiN (001) surface. The yellow, blue, and pink spheres represent Ti, N, and H atoms, respectively.

(a) H_2

Geometry	Position	E ads (meV)
1	1	-6.59
1	2	-7.56
1	3	-19.94
2	1	-37.94
2	2	13.69
2	3	23.29

(b) N_2

Geometry	Position	E ads (meV)
1	1	22.44
1	2	47.77
1	3	-3.93
2	1	-10.56
2	2	1389.76
2	3	79.5

Table 4.1. The adsorption energies of H_2 and N_2 calculated on the TiN (001) surface for each orientation and position.

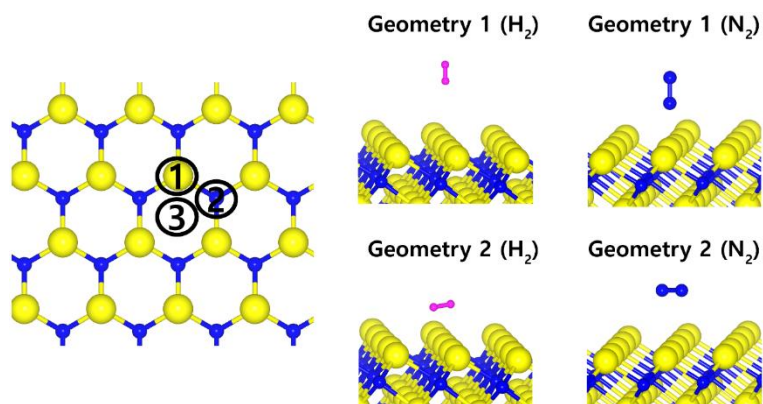


Figure 4.3. Two orientations and three positions of H_2 and N_2 on the Ti-terminated TiN (111) surface.

(a) H_2

Geometry	Position	E ads (meV)
1	1	14.99
1	2	13.01
1	3	11.92
2	1	-498.74
2	2	101.02
2	3	101.05

(b) N_2

Geometry	Position	E ads (meV)
1	1	-790.89
1	2	78.86
1	3	129.47
2	1	-3437.43
2	2	-3144.97
2	3	207.32

Table 4.2. The adsorption energies of H_2 and N_2 calculated on the Ti-terminated TiN (111) surface for each orientation and position.

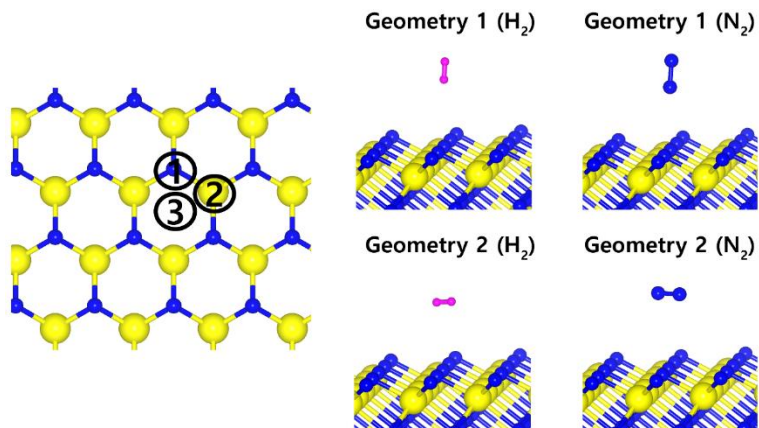


Figure 4.4. Two orientations and three positions of H_2 and N_2 on the N-terminated TiN (111) surface.

(a) H_2

Geometry	Position	E ads (meV)
1	1	-21.72
1	2	-19.21
1	3	-11.25
2	1	-31.82
2	2	-17.48
2	3	-20.29

(b) N_2

Geometry	Position	E ads (meV)
1	1	95.41
1	2	13.78
1	3	13.78
2	1	-11.63
2	2	17.95
2	3	12.39

Table 4.3. The adsorption energies of H_2 and N_2 calculated on the N-terminated TiN (111) surface for each orientation and position.

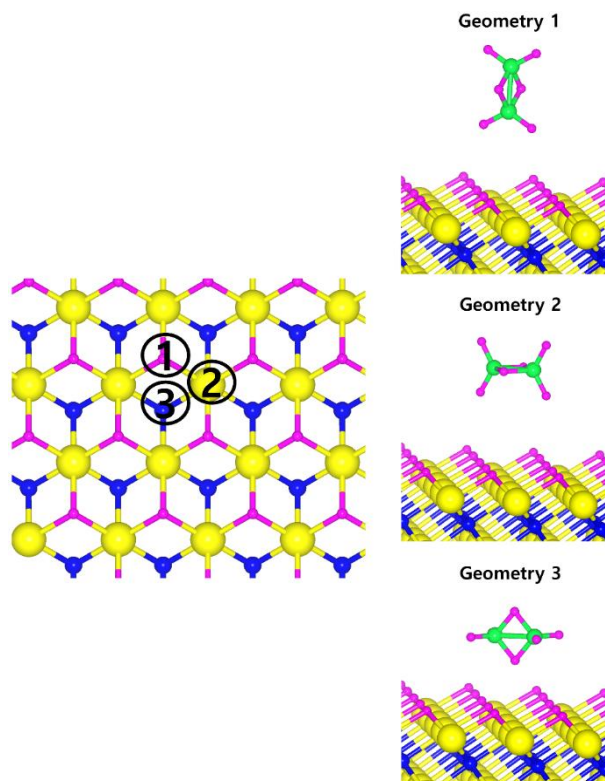


Figure 4.5. Three orientations and three positions of B_2H_6 on the H-covered Ti-terminated TiN (111) surface.

Geometry	Position	E ads (meV)
1	1	1.57
1	2	37.51
1	3	62.63
2	1	-26.76
2	2	-1.59
2	3	-22.21
3	1	94.97
3	2	45.1
3	3	-4.22

Table 4.4. The adsorption energies of B_2H_6 calculated on the H-covered Ti-terminated TiN (111) surface for each orientation and position.

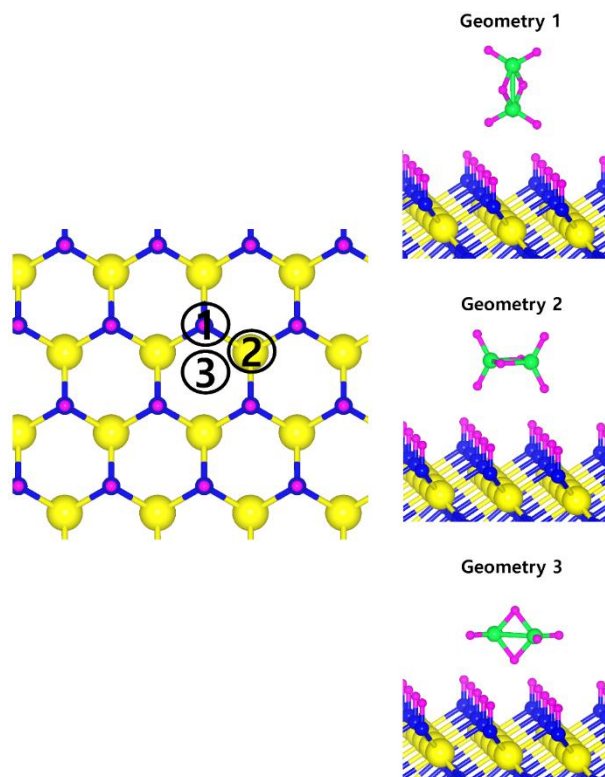


Figure 4.6. Three orientations and three positions of B_2H_6 on the H-covered N-terminated TiN (111) surface.

Geometry	Position	E ads (meV)
1	1	34.87
1	2	43.27
1	3	44.13
2	1	-13.20
2	2	-8.40
2	3	-7.19
3	1	40.13
3	2	10.13
3	3	9.21

Table 4.5. The adsorption energies of B_2H_6 calculated on the H-covered N-terminated TiN (111) surface for each orientation and position.

4.3. Results and discussion

4.3.1. Dissociative reaction of H₂ and N₂ on TiN(001) surface

The optimized structures of initial, transition, and final states for H₂ and N₂ dissociative chemisorption step on the TiN (001) surface are shown in **Figure 4.7 (a) and (b)**. The calculated energy diagram of H₂ and N₂ decomposition on the three different TiN surfaces is shown in **Figure 4.10**. The initial state (IS) in **Figure 4.7 (a)** present the optimized structure with the lowest adsorption energy of H₂ on the surface. The final state (FS) in **Figure 4.7 (a)** shows that dissociated H atoms from H₂ molecule react with titanium atoms of TiN (001) surface after H-H bond dissociation because binding energy on titanium site of the TiN (001) surface is 0.42 eV larger than one on nitrogen site in our calculated results. The reaction energy can be calculated as the energy difference between the initial state and the final state. As shown in **Figure 4.10**, the calculated reaction energy of H₂ on the TiN (001) surface is 1.04 eV, which shows that the reaction is endothermic and energetically unfavorable. The activation energy from initial state to final state is 1.68 eV with transition state in **Figure 4.10**. The N₂ dissociative chemisorption step on the TiN (001) surface is shown in **Figure 4.7 (b)**. It was found that reaction energy is 3.25 eV in **Figure 4.10**, which indicates that the reaction is thermodynamically endothermic and unfavorable. The activation energy from initial state to final state is 4.92 eV with transition state in **Figure 4.10**.

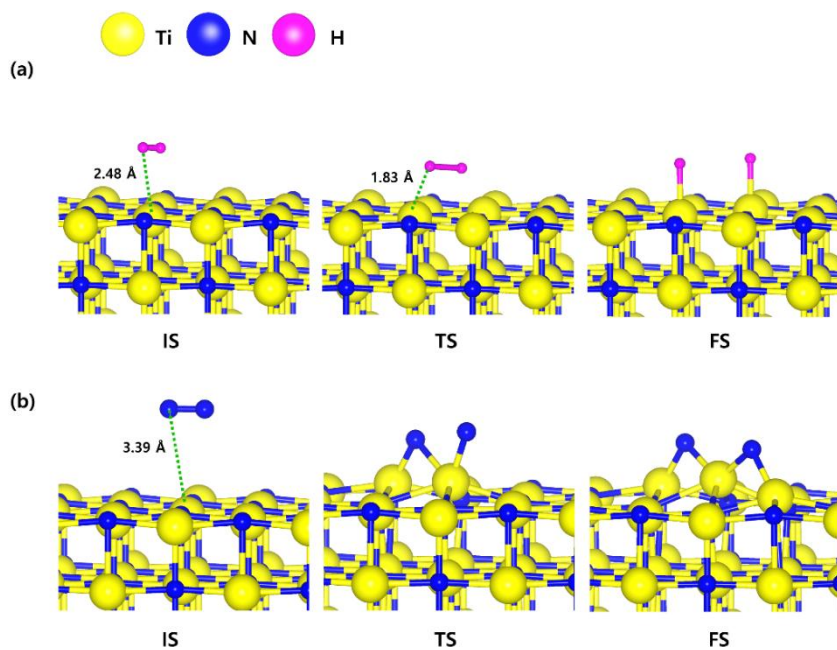


Figure 4.7. The optimized structures for (a) adsorption state, (b) transition state and (c) reaction state of a B_2H_6 on the TiN (001) surface.

4.3.2. Dissociative reaction of H₂ and N₂ on Ti-terminated TiN(111) surface

The decomposition mechanism of H₂ and N₂ was also studied on the Ti-terminated TiN (111) surface to estimate the difference between TiN (001) and TiN (111) surfaces. The optimized initial, transition, and final structures of H₂ and N₂ on the Ti-terminated TiN (111) surface are shown in **Figure 4.8**. It was found that dissociated H atoms and N atoms in final state were adsorbed on the hollow site made by three Ti atoms (Site number 3 in **Figure 3**). As shown in **Figure 4.8 (a)** and **Figure 4.10**, it was found that the reaction energy of H₂ is -2.10 eV, which indicates that the reaction is exothermic and energetically favorable. The activation energy from initial state to final state is 0.11 eV with the transition state in **Figure 4.10**, indicating that this reaction has small energy barrier. As shown in **Figure 4.8 (b)** and **Figure 4.10**, the adsorption energy of N₂ is -3.44 eV, showing that the adsorption is energetically favorable. The reaction energy of N₂ is -2.06 eV in **Figure 4.10**, which indicates that the reaction is exothermic. The activation energy from initial state to final state is 0.92 eV with the transition state in **Figure 4.10**. The energy diagram for the H₂ and N₂ decomposition on Ti-terminated TiN (111) differs from the TiN (001) as illustrated in **Figure 4.10**. It demonstrates that both H-H and N-N bond dissociation steps on the Ti-terminated TiN (111) surfaces are more facile than the TiN (001) surface due to smaller activation energies of dissociation on the Ti-terminated TiN (111) surface. Moreover, the reactions of both H₂ and N₂ are energetically favorable, with their reaction energies of -2.10 eV, -2.06 eV, respectively. The high reactivity of both molecules on the Ti-terminated TiN (111) surface is most likely to be

because the surface has triple dangling bonds per atom, which make the surface even more reactive than the TiN (001) surface. To be more specific, the number of dangling bonds on the Ti-terminated TiN (111) surface is more than that of the TiN (001), so that bond dissociation of both H₂ and N₂ is more favorable on the former. This analysis is confirmed by higher adsorption of both H and N atoms on Ti-terminated (111) surface than the TiN (001) surface as shown in **Table 6**. Due to the aforementioned reasons, this surface can also reduce the energy barriers of the H₂ and N₂ decomposition as compared to the TiN (001) surface.

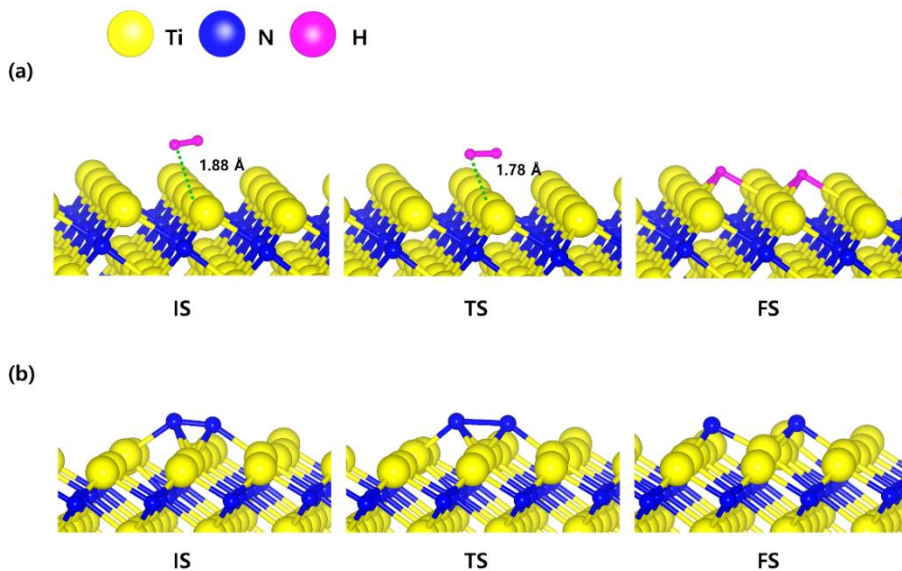


Figure 4.8. The optimized structures for (a) adsorption state, (b) transition state and (c) reaction state of a B_2H_6 on the Ti-terminated TiN (111) surface.

Surface	H	N
TiN (001)	2.93	5.79
Ti-terminated TiN (111)	4.61	11.0
N-terminated TiN (111)	5.73	Not bound

Table 4.6. Activation energies (E_a , eV) and reaction energies (E_{rxn} , eV) of B_2H_6 dissociation on the Ti-terminated TiN (111) surface.

4.3.3. Dissociative reaction of H₂ and N₂ on N-terminated TiN(111) surface

The optimized initial, transition, and final structures of H₂ and N₂ on the N-terminated TiN (111) surface are displayed in **Figure 4.9**. It was found that dissociated H atoms in final state were adsorbed on the hollow site made by three N atoms (Site number 3 in **Figure 4.4**). As shown in **Figure 4.9 (a)** and **Figure 4.10**, the reaction energy of H₂ is -4.66 eV, which indicates that the reaction is exothermic. The activation energy from initial state to final state is 0.26 eV with the transition state, indicating that this reaction requires low energy barrier. However, as for the N₂ in **Figure 4.9 (b)** and **Figure 4.10**, the reaction energy of N₂ is 1.24 eV, which indicates that the reaction is endothermic. In this case, N₂ molecule was not dissociated on the surface. The activation energy from initial state to final state is 1.45 eV with the transition state. We found that the H-H bond breaking on the N-terminated TiN (111) surfaces were much more facile than those of both TiN (001) and Ti-terminated TiN (111) surfaces, as shown in **Figure 4.10**. This result is primarily because the binding energy ($E_b = 5.73$ eV) of H atoms on the N-terminated TiN (111) surface is the highest among the three different TiN surfaces, as shown in **Table 4.7**. Furthermore, the decomposition of H₂ on the N-terminated TiN (111) surface is energetically favorable due to the downhill reaction and small energy barrier for H-H bond breaking. However, N-terminated TiN (111) surface was not advantageous for breaking the N-N bond because N₂ was not dissociated on the N-terminated TiN (111) surface. Although N₂ molecule has a larger bond dissociation energy (Edissociation = 9.45 eV)[52] than H₂ (Edissociation = 4.36 eV)[52] due to triple bonding

nature of N_2 , this N_2 molecule could be dissociated on Ti-terminated TiN (111) surface. We suggest that this phenomenon is attributed to a large binding energy ($E_b = 11.0$ eV) of N atom on the Ti-terminated TiN (111) surface, as depicted in **Table 4.7**.

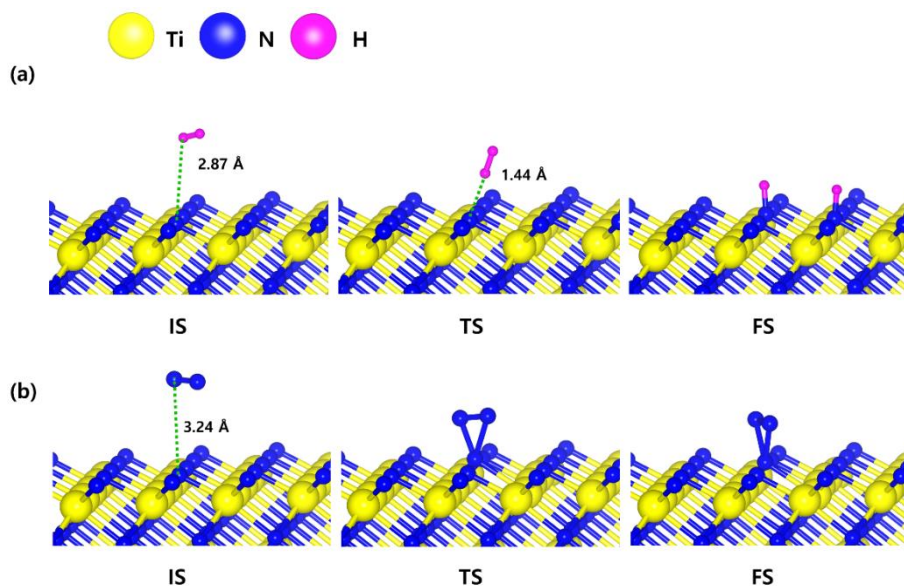


Figure 4.9. The optimized initial, transition, final structures of the dissociative chemisorption step for (a) H₂ and (b) N₂ on the N-terminated TiN (111) surface.

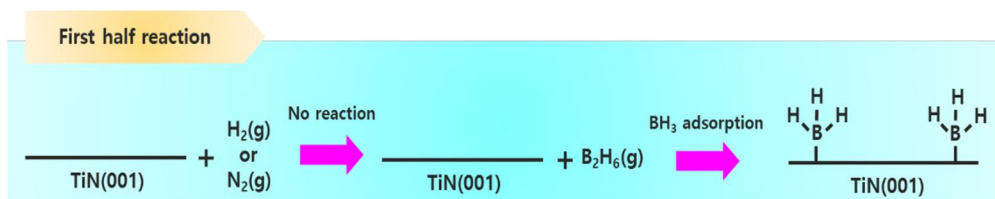
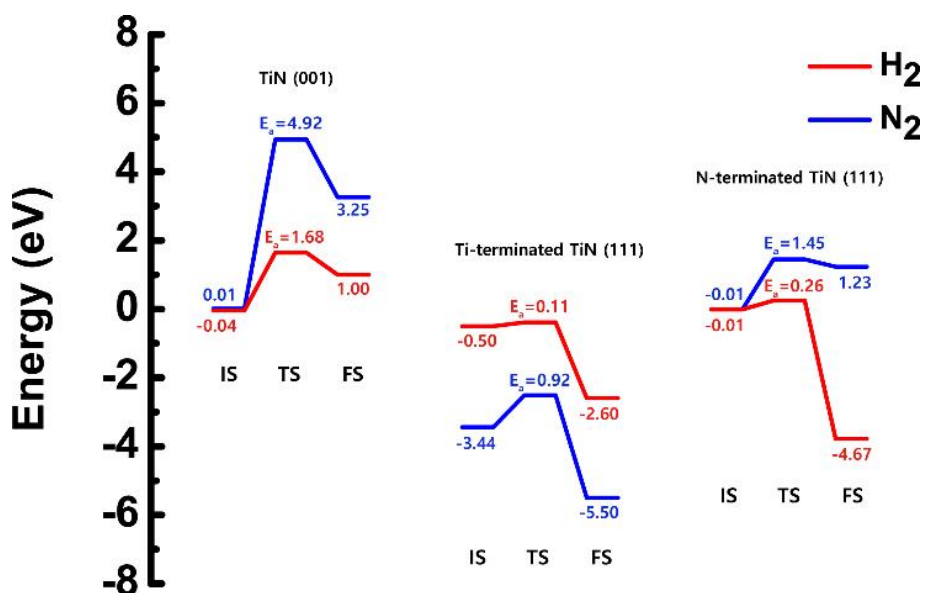


Figure 4.10. Calculated energy diagram(upper) of H₂ and N₂ decomposition on the TiN (001), the Ti-terminated TiN (111), and N-terminated TiN (111) surface. First half reaction for TiN (001) surface(below) is drawn.

4.3.4. Effects of N₂ treatment on TiN surfaces during ALD process

Aforementioned in Section 4.3.1, the TiN (001) surface is difficult to decompose both H₂ and N₂ because those reactions in **Figure 4.10** are energetically unfavourable. However, since Ti-terminated TiN (111) can decompose H₂ and N₂ as shown **Figure 4.10**, H-covered Ti-terminated TiN (111) and N-terminated TiN (111) surfaces can be made. In the case of N terminated TiN (111), N-N bond dissociation is not possible, but H-H bond dissociation is possible, so that H-covered N-terminated TiN (111) surface can be made. **Figure 4.8 (b)** and **Figure 4.10** show that N₂ treatment on Ti-terminated TiN (111) surface is more likely to make the surface to be N-terminated TiN (111) surface, which results in making a lot of N-terminated TiN (111) surfaces under ALD process. Our previous study[19] have shown that the N-terminated TiN (111) surface among three TiN surfaces is the best surface for the B₂H₆ decomposition reaction. The combination of our previous study[19] and this study provides new information of the effect of N₂ treatment, which plays a role of a catalyst to decompose B₂H₆. Since both results of our previous study and this study explain the effect of N₂ treatment enough well, we have focused on investigation of the H₂ effect in this study. The decomposition processes of B₂H₆ on both H covered Ti-terminated TiN (111) and H-covered N-terminated TiN (111) surface were analyzed in detail to investigate the effect of H₂ treatment. For the TiN (001) surface, the H-covered TiN (001) surface is excluded from the text because the H-covered TiN (001) surface is energetically unstable and H atoms on the surface are desorbed as H₂.

4.3.5. Dissociative reaction of B₂H₆ on H-covered Ti-terminated TiN(111) surface

Based on the results shown in Section 4.3.2, when the Ti-terminated TiN (111) surface is subjected to H₂ treatment, the H₂ molecule can be easily decomposed because of the low energy barrier for H₂ bond dissociation on the surface, and thus H-covered Ti-terminated TiN (111) surface can be made.

Figure 4.11 shows the decomposition reaction mechanism of B₂H₆ molecules when H-covered Ti-terminated TiN (111) surface is formed after H₂ treatment.

Figure 4.11 (a) shows the first reaction step that the H atoms of the B₂H₆ molecule adsorbed on the TiN surface react with the H atoms on the TiN surface, desorbing H₂, and remaining B₂H₅ bound to the surface. It was found that dissociated B₂H₅ molecule is adsorbed on the hollow site made by three Ti atoms (Site number 4 in **Figure 4.5**). The reaction energy is 0.77 eV in **Figure 4.12**, indicating that the reaction is endothermic. The activation energy is 1.24 eV with the transition state in **Figure 4.12**. **Figure 4.11 (b)** shows the second reaction step that the H atom of the B₂H₅ molecule adsorbed on the surface react with the H atom of the TiN surface to be desorbed into H₂. As for the second reaction step, it shows that the reaction energy is -0.11 eV with an activation energy of 1.33 eV in **Figure 4.12**.

To complete the overall reaction energetics of B₂H₆ for the optimized reaction path, the calculated energy diagram of B₂H₆ decomposition on the H-covered Ti-terminated TiN (111) surface is displayed in **Figure 4.12**. The detailed structures of B₂H₆ during the overall reaction pathway on the surface for transition state calculations can be found in **Figure 4.13 and Table 4.8**. During the reaction of the B₂H₆ precursor, this calculation shows that the

overall reaction process is endothermic, with a calculated overall reaction energy of 4.92 eV in **Table 4.7**. This result indicates that B₂H₆ dissociative chemisorption on H-covered Ti- terminated TiN (111) is energetically unfavourable due to the uphill reactions and high activation energies that range from a minimum of 0.66 eV to a maximum of 2.49 eV in **Table 4.7**. This implies that the low reactivity of B₂H₆ with the surface is attributed to the presence of H-covered surface with compared to our previous results[19], as shown in **Table 4.7**, reporting that dissociative reaction of B₂H₆ is energetically favorable on Ti-terminated TiN (111) surface. As a result, an effect of the H₂ treatment on the surface is to passivate the TiN surface to prevent it from reacting with the B₂H₆ molecule.

Surface	Bond dissociation	$E_{a, \text{minimum}}$ (eV)	$E_{a, \text{maximum}}$ (eV)	$E_{\text{rxn, overall}}$ (eV)	Note
H-covered Ti-terminated TiN (111)	B-B & B-H	0.66	2.49	4.92	This study
H-covered N-terminated TiN (111)	B-B & B-H	0.40	1.65	1.26	This study
Ti-terminated TiN (111)	B-B & B-H	0.07	0.93	-0.88	Our previous study[19]
N-terminated TiN (111)	B-B & B-H	Barrier-less	0.39	-19.0	Our previous study[19]

Table 4.7. Comparison of minimum and maximum activation energies ($E_{a, \text{minimum}}$, $E_{a, \text{maximum}}$, eV) and overall reaction energies ($E_{\text{rxn, overall}}$, eV) of B_2H_6 bond dissociation on the H-covered TiN and the TiN surfaces.

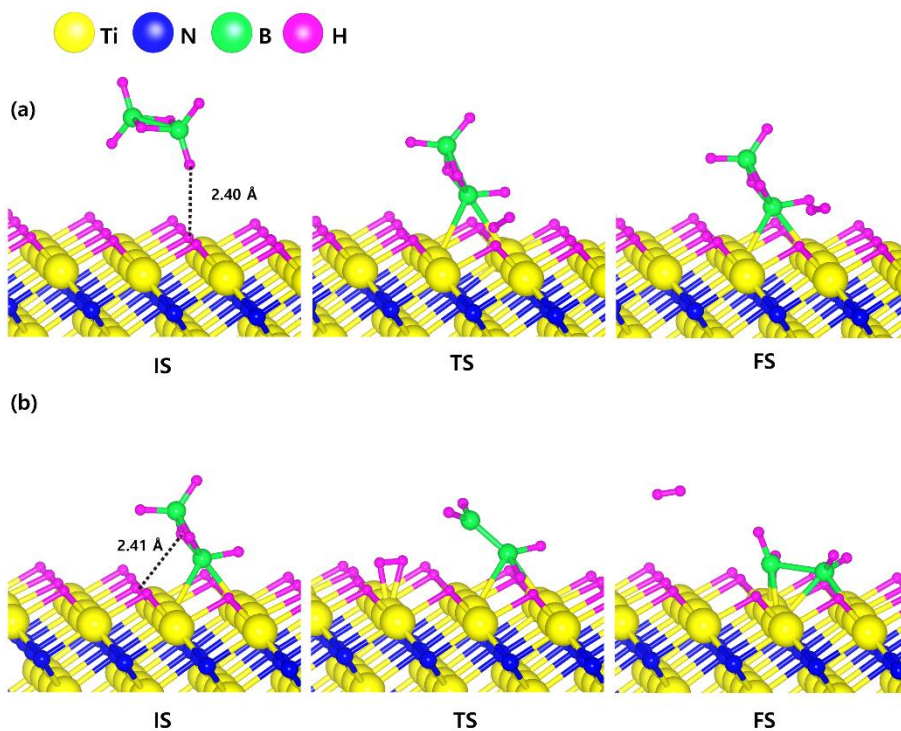


Figure 4.11. Dissociative chemisorption of B_2H_6 on the H-covered Ti-terminated TiN (111) surface: (a) the first reaction step (b) the second reaction step.

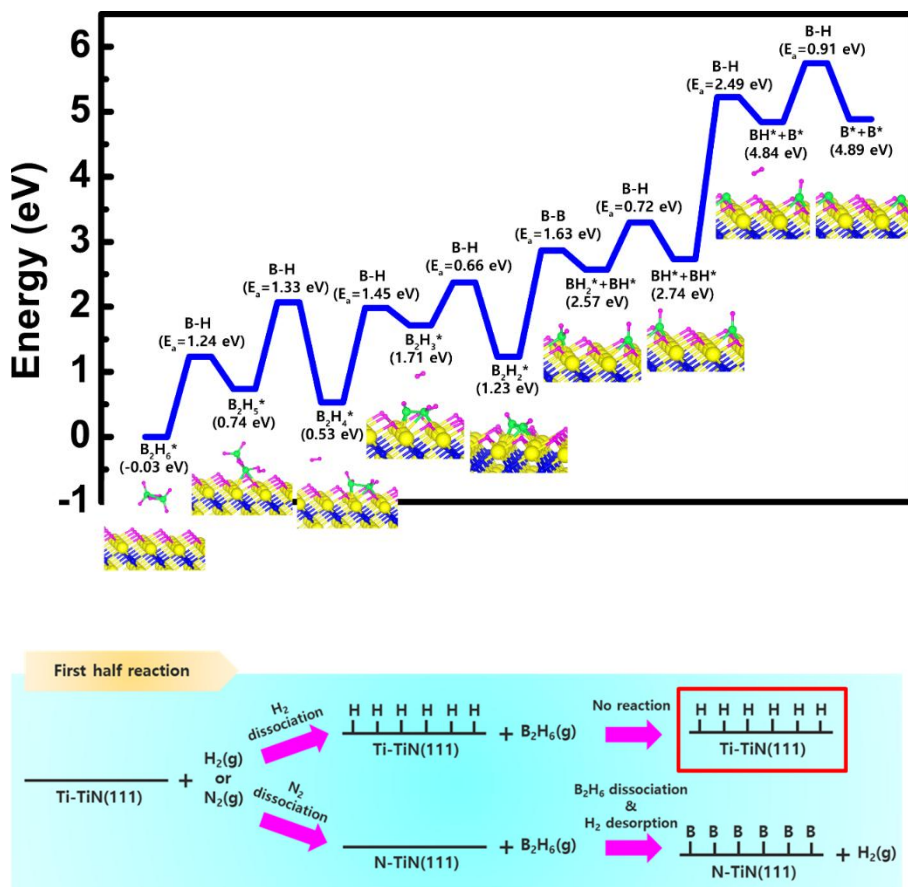
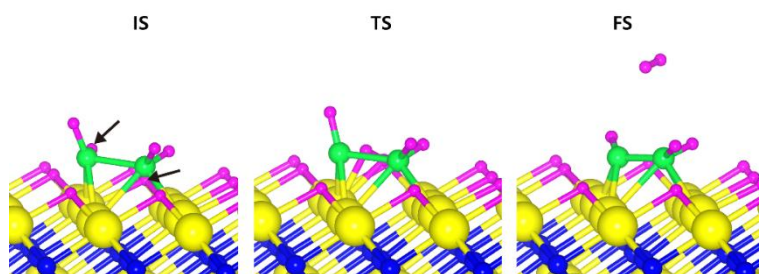
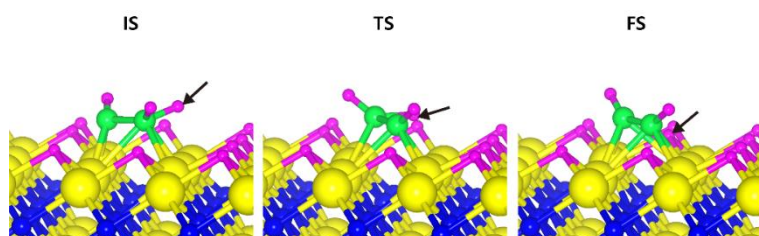


Figure 4.12. Calculated energy diagram of B_2H_6 decomposition on the H-covered N-terminated TiN (111) surface

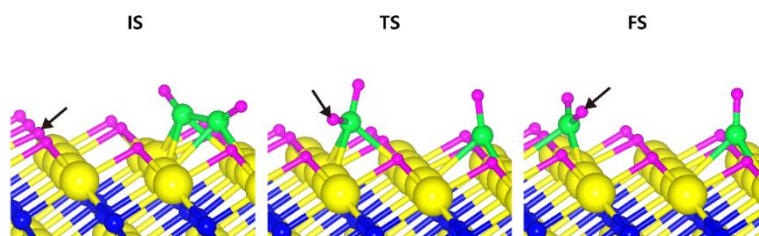
3rd reaction step : B-H bond dissociation



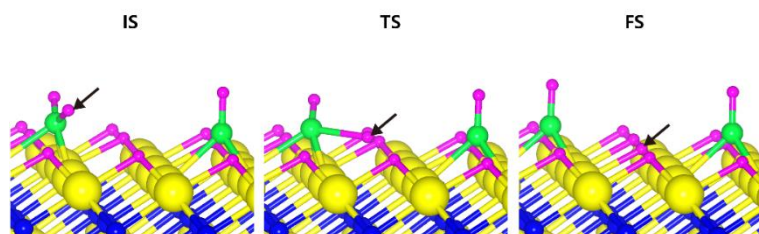
4th reaction step : B-H bond dissociation



5th reaction step : B-B bond dissociation



6th reaction step : B-H bond dissociation



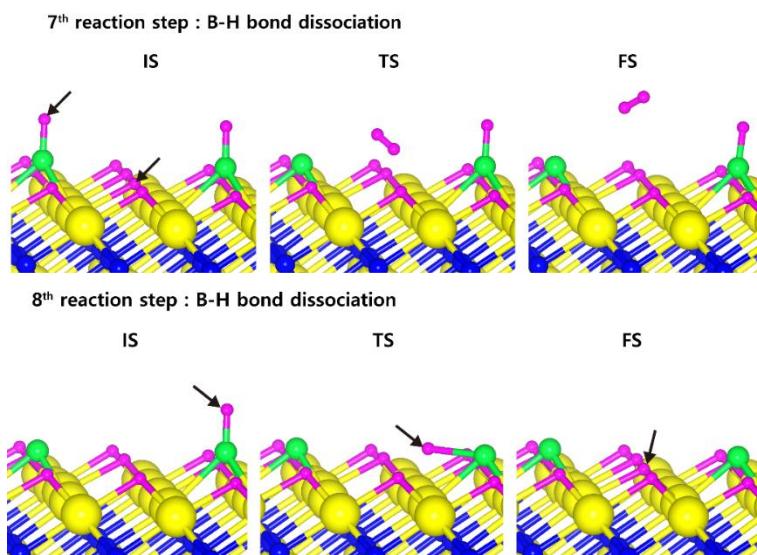


Figure 4.13. Initial (IS), transition (TS), and final (FS) states of intermediate reactions from the 3rd reaction step to the 7th reaction step on the H-covered Ti-terminated TiN (111) surface.

Reaction step	Bond dissociation	E_a (eV)	E_{rxn} (eV)
step 1	B-H	1.24	0.77
step 2	B-H	1.33	-0.21
step 3	B-H	1.45	1.18
step 4	B-H	0.66	-0.48
step 5	B-H	1.63	1.34
step 6	B-B	0.72	0.17
step 7	B-H	2.49	2.10
step 8	B-H	0.91	0.05

Table 4.8. Activation energies (E_a , eV) and reaction energies (E_{rxn} , eV) of B_2H_6 dissociation on the H-covered Ti-terminated TiN (111) surface.

4.3.6. Dissociative reaction of B₂H₆ on H-covered N-terminated TiN(111) surface

Based on the results shown in Section 4.3.3, when the N-terminated TiN (111) surface is subjected to H₂ treatment, the H₂ molecule can be easily dissociated because of the low barrier for H₂ bond dissociation on the surface, and thus H-covered N-terminated TiN (111) surface can be made. **Figure 4.14** shows the decomposition reaction mechanism of B₂H₆ molecules when H-covered N-terminated TiN (111) surface is formed after H₂ treatment. **Figure 4.14 (a)** shows the first reaction step that the H atoms of the B₂H₆ molecule adsorbed on the TiN surface react with the H atoms on the TiN surface, desorbing H₂, and remaining B₂H₅ bound to the surface. The reaction energy is -0.38 eV in **Figure 4.15**, indicating that the reaction is exothermic. The activation energy is 0.87 eV with the transition state in **Figure 4.15**. **Figure 4.14 (b)** shows the second reaction step that the H atom of the B₂H₅ molecule adsorbed on the surface react with the H atom of the TiN surface to be desorbed into H₂. As for the second reaction step, it shows that the reaction energy is 0.04 eV with an activation energy of 1.07 eV in **Figure 4.15**.

The entire energy diagram for the B₂H₆ decomposition on H-covered N-terminated TiN (111) is illustrated in **Figure 4.15**. The detailed structures of B₂H₆ during the overall reaction pathway on the surface for transition state calculations can be found in the **Figure 4.16 and Table 4.9**. During the reaction of the B₂H₆ precursor, this calculation shows that the overall reaction process is endothermic with a calculated overall reaction energy of 1.26 eV in **Table 4.7**. Although the overall reaction from 1st reaction step to 7th reaction

step in the **Figure 4.16** is energetically unfavourable, B_2H_6 dissociative reactions can be occurred from 1st reaction step to 5th reaction step because the overall reaction energy from 1st to 5th step is -0.35 eV in the **Figure 4.16**, meaning that the reaction is energetically favourable. From 5th reaction step, two remaining BH species are difficult to be dissociated due to the uphill reactions of B-H bond breaking with energy barriers of 1.65 eV, and 0.68 eV, respectively in **Figure 4.15**.

Unlike the H-covered Ti-terminated TiN (111), H-covered N-terminated TiN (111) surface can dissociate the B_2H_6 molecule to be BH species up to 5th reaction step. We suggest that those remaining BH species and H atoms would be desorbed as BF_3 and HF from WF_6 in the next ALD cycle.

However, compared to the N-terminated TiN (111) in our previous results[19], dissociative reaction of B_2H_6 is much more favorable on N-terminated TiN (111) surface than the H-covered N-terminated TiN (111) surface as shown in **Table 4.7**. This implies that the low reactivity of B_2H_6 with the surface is attributed to the presence of H-covered surface with compared to the surface. As a result, an effect of the H_2 treatment on the surface is to passivate the TiN surface to prevent it from reacting with the B_2H_6 molecule.

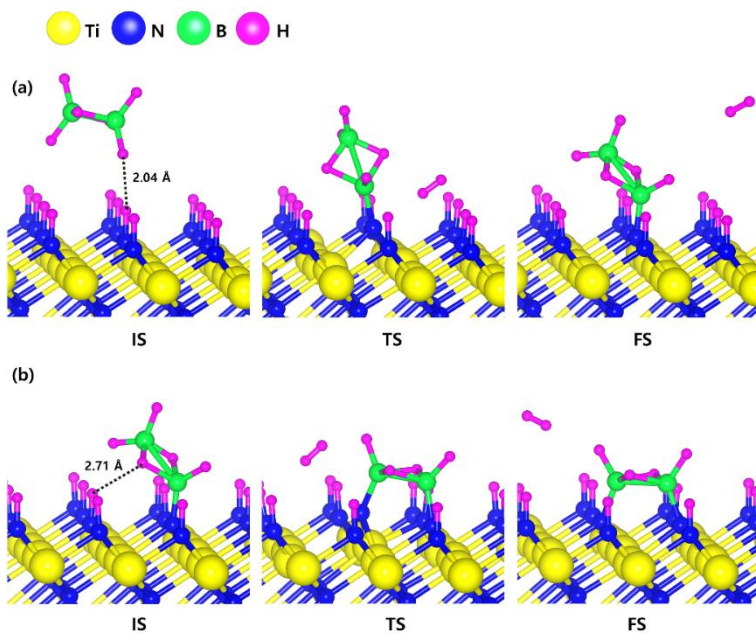


Figure 4.14. Dissociative chemisorption of B_2H_6 on the H-covered Ti-terminated TiN (111) surface: (a) the first reaction step (b) the second reaction step.

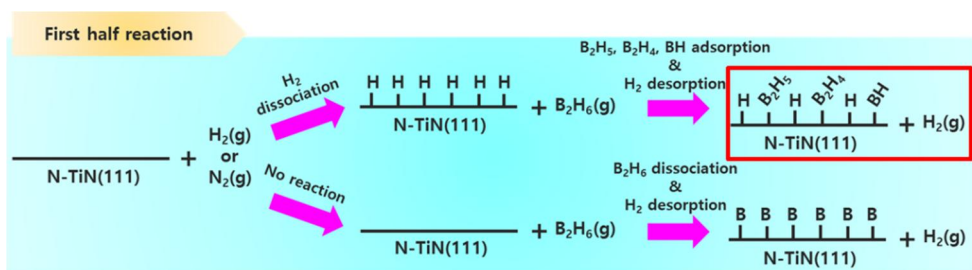
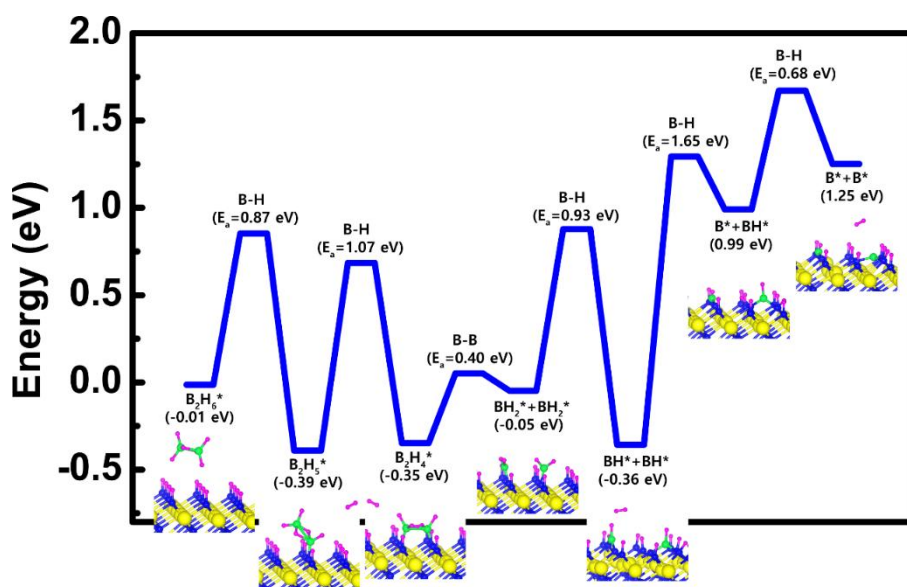


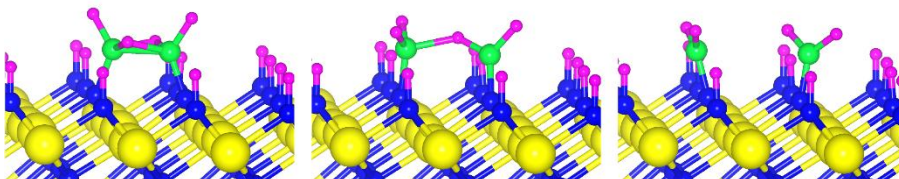
Figure 4.15. Calculated energy diagram of B_2H_6 decomposition on the H-covered N-terminated TiN (111) surface.

3rd reaction step : B-B bond dissociation

IS

TS

FS

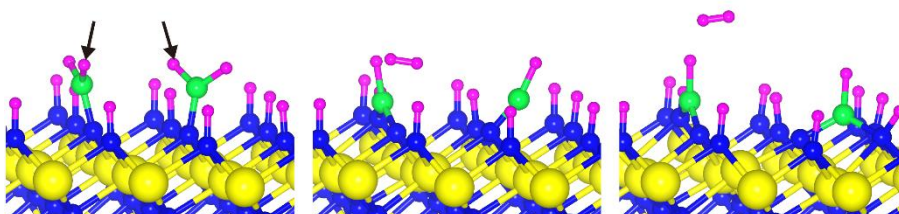


4th reaction step : B-H bond dissociation

IS

TS

FS

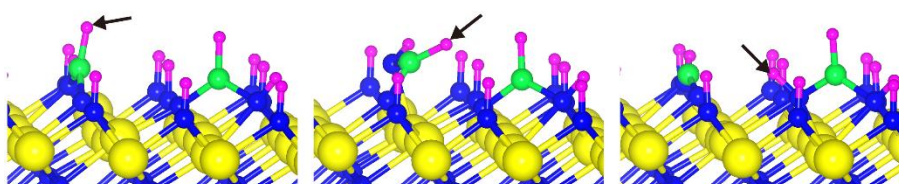


5th reaction step : B-H bond dissociation

IS

TS

FS

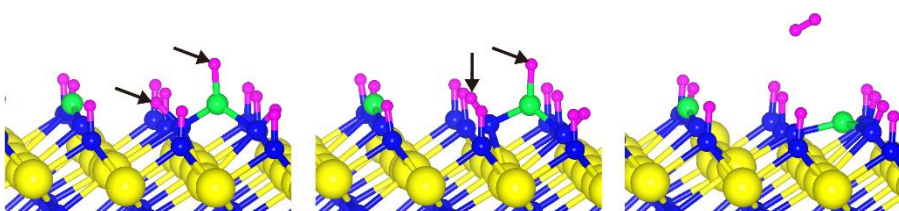


6th reaction step : B-H bond dissociation

IS

TS

FS



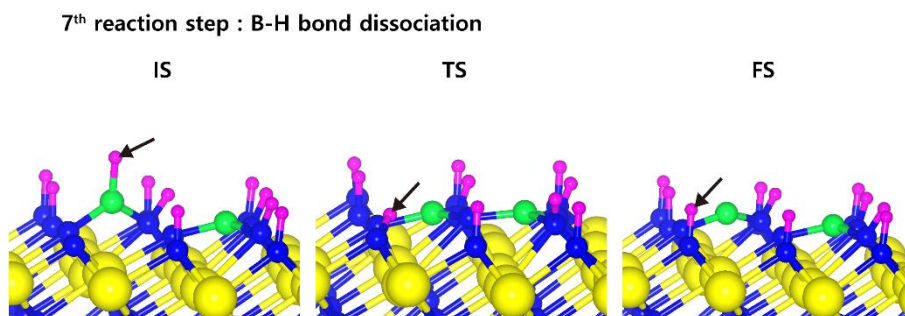


Figure 4.16. Initial (IS), transition (TS), and final (FS) states of intermediate reactions from the 3rd reaction step to the 7th reaction step on the H-covered N-terminated TiN (111) surface.

Reaction step	Bond dissociation	E_a (eV)	E_{rxn} (eV)
step 1	B-H	0.87	-0.38
step 2	B-H	1.07	0.04
step 3	B-B	0.40	0.30
step 4	B-H	0.93	-0.31
step 5	B-H	1.65	1.35
step 6	B-H	0.68	0.26

Table 4.9. Activation energies (E_a , eV) and reaction energies (E_{rxn} , eV) of B_2H_6 dissociation on the H-covered N-terminated TiN (111) surface.

4.3.7. Discussions

Figure 4.17-4.18 show the calculated overall energy diagrams of B_2H_6 decomposition for path a, b, and c on the H-covered TiN (111) surface. There are three reaction paths. As shown in **Figure 4.13**, path a is the path where the H atom of the B_xH_y molecule adsorbed on the surface react with the H atom of the TiN surface to be desorbed into H_2 during 1st, 2nd, 3rd, and 7th reaction steps. At 5th reaction step, B-B bond breaking from B_2H_2 occurs. For 4th, 6th, and 8th reaction steps, H atom of B_xH_y molecule is adsorbed on the site where H atom of the surface is empty due to H_2 desorption in previous reaction steps of 3rd, 5th, and 7th, respectively. Path b is the path where the H atom of the B_xH_y molecule adsorbed on the surface react with the H atom of the TiN surface to be desorbed into H_2 during all reaction steps without the 7th reaction step for B-B bond breaking. Path c is where the H atom of the B_xH_y molecule adsorbed on the surface react with the H atom of the TiN surface to be desorbed into H_2 during 1st, 2nd, 3rd, and 6th reaction steps. For 4th and 6th reaction steps, H atom of B_xH_y molecule is adsorbed on the site where H atom of the surface is empty due to H_2 desorption in previous reaction steps of 3rd and 5th, respectively. At the 7th reaction step, B-B bond breaking from B_2 occurs. **Table 4.10-4.11** indicate comparison of minimum and maximum activation energies ($E_{a, \text{minimum}}$, $E_{a, \text{maximum}}$, eV) and overall reaction energies ($E_{\text{rxn, overall}}$, eV) of B_2H_6 dissociation for path a, b, and c on the H-covered TiN surfaces.

Table 4.7 shows the minimum and maximum activation energies, and overall reaction energies required for B_2H_6 bond dissociation on the H-covered TiN and the TiN surfaces. As for the **Table 4.7**, the information on

the TiN (001) surface is excluded because it is difficult to make an H-covered surface as above mentioned in Section 4.3.4. In addition, it has been reported that B_2H_6 dissociative reaction on TiN (001) surface is energetically unfavorable in our previous study[19], meaning that the TiN (001) is not suitable for B_2H_6 dosing process.

As shown in **Table 4.7**, B_2H_6 dissociative reactions on both H-covered Ti-terminated TiN (111) surface and H-covered N-terminated TiN (111) surface require large overall reaction energies and activation energies, meaning that those reactions are energetically unfavorable. However, B_2H_6 dissociative reactions on both Ti-terminated TiN (111) surface and N-terminated TiN (111) surface are exothermic, meaning that those reactions are energetically favorable. In conclusion, an effect of H_2 treatment on both Ti-terminated TiN (111) surface and N-terminated TiN (111) surface make those surfaces to be H-covered surfaces, leading to degradation of the B_2H_6 dissociative reactions. As a result, H_2 treatment has an effect of passivating the TiN surfaces. However, an effect of N_2 treatment on the TiN surface is more likely to make the surface to be N-terminated TiN (111) surface under ALD process as above mentioned in Section 4.3.4, which leads to making a lot of N-terminated TiN (111) surfaces. **Table 4.7** shows that B_2H_6 dissociative reaction on N-terminated TiN (111) surface is energetically much more favorable than Ti-terminated TiN (111) surface because it has much lower reaction energy. As a result, N_2 treatment has an effect of making the TiN surfaces to be more reactive surface for B_2H_6 bond dissociation. In the next ALD cycle after B_2H_6 dosing process, WF_6 molecule is generally used for W deposition. Since boron (B) adatoms on TiN surface would react with the F atoms of WF_6 , BF_3 desorption process would occur on the surface,

therefore, a uniform W film could be deposited.

Our results imply that making a lot of N-terminated TiN (111) surfaces, by N₂ treatment, plays an important role in improving the properties of the subsequent W nucleation layers during the W ALD process because easily dissociated B adatoms on the surface could dissociate the WF₆ molecule and desorb into BF₃. Since W nucleation layers are experimentally difficult to be grown using only WF₆ molecule without B₂H₆ dosing process[14], B₂H₆ should be easily dissociated on the TiN surfaces for obtaining high quality W nucleation layers during W ALD process. Although H₂ molecule plays a role to lower reactivity of B₂H₆ on the TiN surfaces, this molecule can be useful to remove residual F atoms, which degrade a quality of the W layer. It has been reported that ALD W deposition under H₂ exposure help to remove residual F atoms by desorption of HF.[53] Moreover, they found that adding H₂ during W growth helps passivate SiO₂ against W nucleation as shown in **Figure 4.19**.

Our proposed W ALD process can be seen in **Figure 4.20** since N₂ treatment can make the TiN surfaces become an N-terminated TiN (111), which results in making a lot of N-terminated TiN (111) surfaces, having a very reactive nature for B₂H₆ bond dissociation. This previously experimental results and our theoretical results give insight into how to design the ALD W deposition process to develop the W films for highly integrated devices.

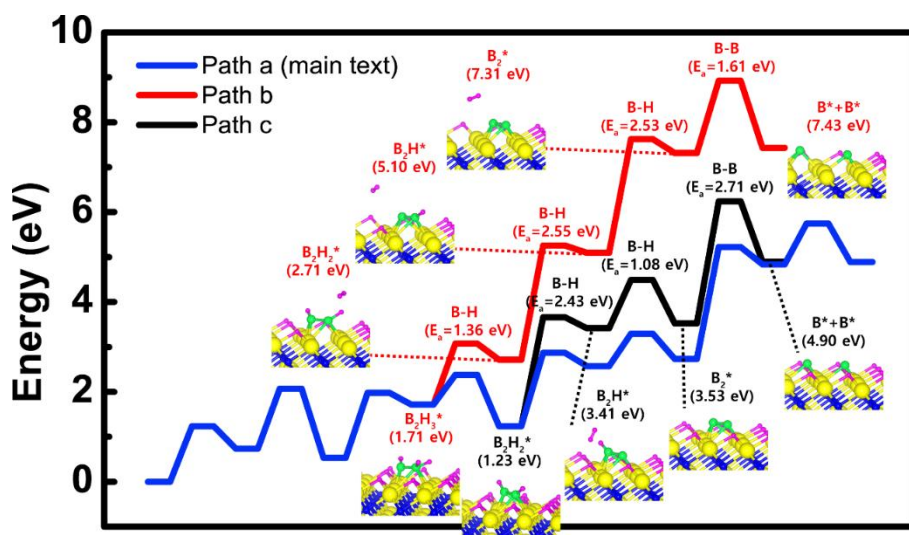


Figure 4.17. Calculated overall energy diagram of B_2H_6 decomposition for path a, b, and c on the H-covered Ti-terminated TiN (111) surface.

Surface	Bond dissociation	$E_{a, \text{minimum}}$ (eV)	$E_{a, \text{maximum}}$ (eV)	$E_{\text{rxn, overall}}$ (eV)	Note
H-covered Ti-terminated TiN (111)	B-B & B-H	0.66	2.49	4.92	Path a (main text)
		1.36	2.55	7.46	Path b
		1.08	2.71	4.93	Path c

Table 4.10. Comparison of minimum and maximum activation energies ($E_{a, \text{minimum}}$, $E_{a, \text{maximum}}$, eV) and overall reaction energies ($E_{\text{rxn, overall}}$, eV) of B_2H_6 dissociation for path a, b, and c on the H-covered Ti-terminated TiN surfaces.

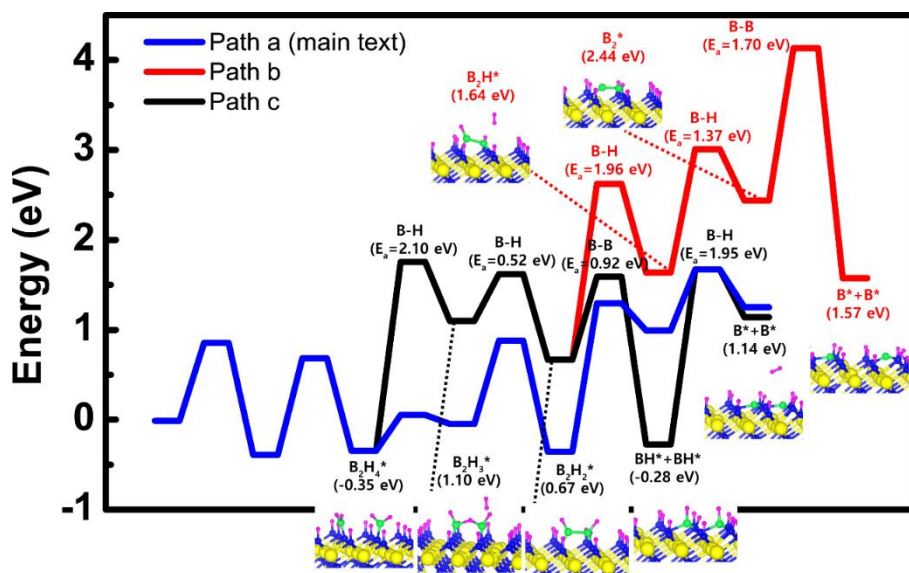


Figure 4.18. Calculated overall energy diagram of B_2H_6 decomposition for path a, b, and c on the H-covered N-terminated TiN (111) surface.

Surface	Bond dissociation	$E_{a, \text{minimum}}$ (eV)	$E_{a, \text{maximum}}$ (eV)	$E_{\text{rxn, overall}}$ (eV)	Note
H-covered N-terminated TiN (111)		0.40	1.65	1.26	Path a (main text)
	B-B & B-H	0.52	2.10	1.58	Path b
		0.52	2.10	1.15	Path c

Table 4.11. Comparison of minimum and maximum activation energies ($E_{a, \text{minimum}}$, $E_{a, \text{maximum}}$, eV) and overall reaction energies ($E_{\text{rxn, overall}}$, eV) of B_2H_6 dissociation for path a, b, and c on the H-covered N-terminated TiN surfaces.

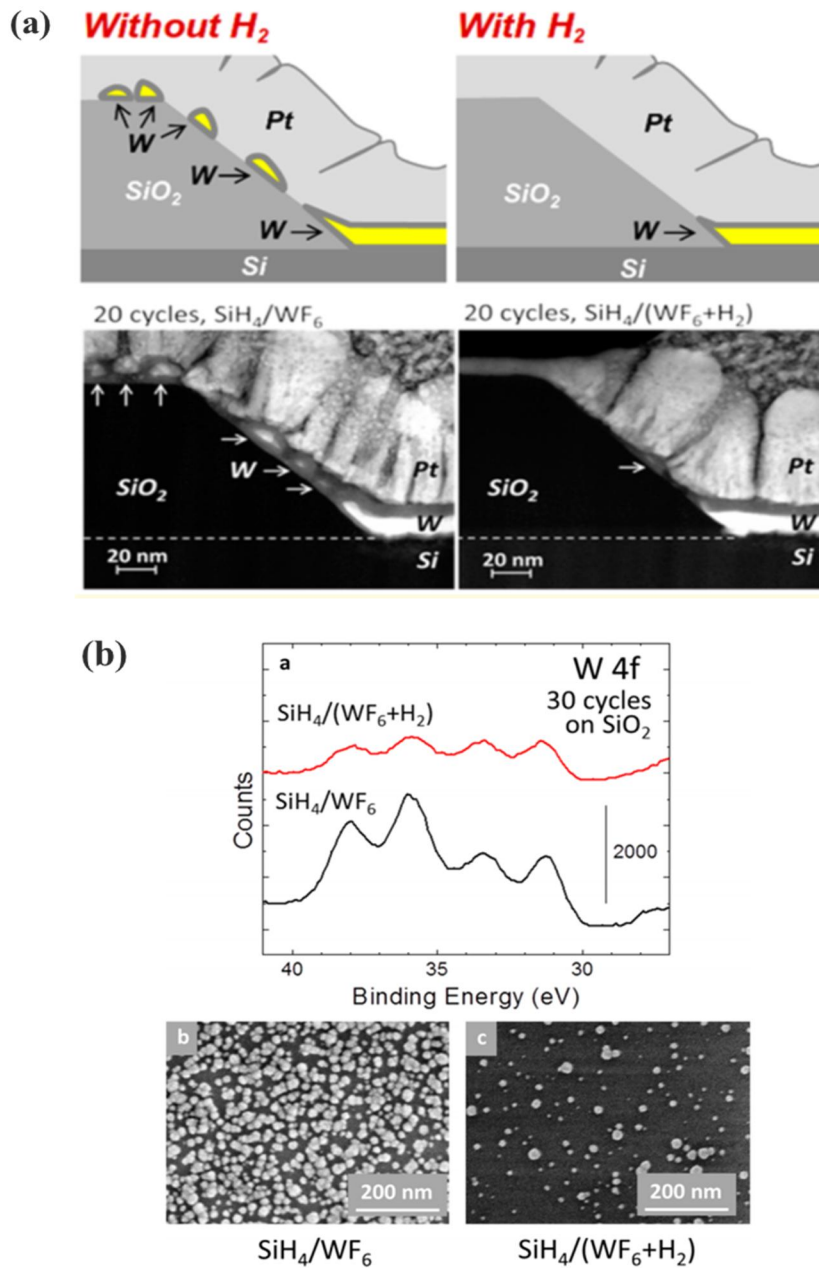


Figure 4.19. (a) Passivated SiO_2 against W nucleation by adding H_2 (b) XPS and SEM for nucleated W on SiO_2 . [53]

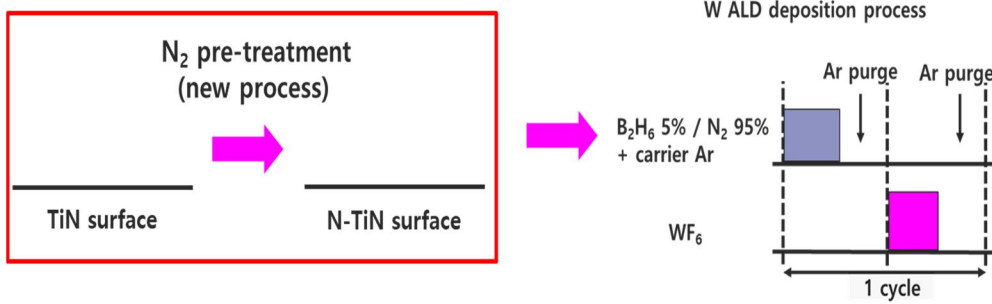


Figure 4.20. Proposed W ALD process.

4.4. Summary

In summary, we investigated the effects of H_2 and N_2 treatment on TiN surfaces for B_2H_6 dosing process based on DFT calculation. Since H_2 molecule is easily dissociated on both Ti-terminated TiN (111) and N-terminated TiN (111) surfaces, H-covered Ti-terminated TiN (111) and H-covered N-terminated TiN (111) surfaces can be made. In our DFT calculated results, H_2 treatment on the TiN surfaces is make the surface to be H-covered TiN surfaces, which results in lowering the reactivity of B_2H_6 precursor since the overall reactions of the B_2H_6 on the H-covered TiN surfaces are energetically less favorable than the TiN surfaces. As a result, an effect of the H_2 treatment is to decrease the reactivity of the B_2H_6 molecule on the TiN surface. However, N_2 treatment on Ti-terminated TiN (111) surface is more likely to make the surface to be N-terminated TiN (111) surface, which results in making a lot of N-terminated TiN (111) surfaces, having very reactive nature for B_2H_6 bond dissociation. As a result, the effect of N_2 treatment serves as a catalyst to decompose B_2H_6 . Although N_2 molecule is more useful for B_2H_6 bond dissociation than H_2 in regard of the reactivity, H_2 molecule has more advantage to remove residual F atoms than N_2 in regard of removing F atoms. From the understanding of the effect of H_2 and N_2 during the B_2H_6 dosing process, the use of proper gas treatment is required for improvement of the W nucleation layers. These results imply that the deep understanding of the role of H_2 and N_2 treatment gives us insight into improving the W ALD process for future memory devices.

4.5. Bibliography

- [1] S.-B. Baek, D.-H. Kim, and Y.-C. Kim, "Adsorption and surface reaction of bis-diethylaminosilane as a Si precursor on an OH-terminated Si (001) surface," *Applied Surface Science*, vol. 258, no. 17, pp. 6341-6344, 2012/06/15/ 2012.
- [2] M. C. Schuille *et al.*, "Experimental and simulation approach for process optimization of atomic layer deposited thin films in high aspect ratio 3D structures," *Journal of Vacuum Science & Technology A*, vol. 35, no. 1, p. 01B118, 2017.
- [3] W. D. Huang *et al.*, "Low temperature PECVD SiN_x films applied in OLED packaging," *Materials Science and Engineering B-Solid State Materials for Advanced Technology*, vol. 98, no. 3, pp. 248-254, Apr 15 2003.
- [4] A. El Amrani, A. Bekhtari, B. Mahmoudi, A. Lefgoum, and H. Menari, "Experimental study of the effect of process parameters on plasma-enhanced chemical vapour deposition of silicon nitride film," *Vacuum*, vol. 86, no. 4, pp. 386-390, 2011/11/11/ 2011.
- [5] N. Sharma, M. Hooda, and S. K. Sharma, "Synthesis and Characterization of LPCVD Polysilicon and Silicon Nitride Thin Films for MEMS Applications," *Journal of Materials*, vol. 2014, p. 8, 2014, Art. no. 954618.
- [6] B. C. Joshi, G. Eranna, D. P. Runthala, B. B. Dixit, O. P. Wadhawan, and P. D. Vyas, *LPCVD and PECVD silicon nitride for microelectronics technology*. 2000, pp. 303-309.
- [7] W. J. Lee, J. H. Lee, C. O. Park, Y. S. Lee, S. J. Shin, and S. K. Rha, "A comparative study on the Si precursors for the atomic layer deposition of silicon nitride thin films," *Journal of the Korean Physical Society*, vol. 45, no. 5, pp. 1352-1355, Nov 2004.
- [8] J. W. Klaus, A. W. Ott, A. C. Dillon, and S. M. George, "Atomic layer controlled growth of Si₃N₄ films using sequential surface reactions," *Surface Science*, vol. 418, no. 1, pp. L14-L19, 1998/11/27/ 1998.
- [9] C. A. Murray, S. D. Elliott, D. Hausmann, J. Henri, and A. LaVoie, "Effect of Reaction Mechanism on Precursor Exposure Time in Atomic Layer Deposition of Silicon Oxide and Silicon Nitride," *ACS Applied Materials & Interfaces*, vol. 6, no. 13, pp. 10534-10541, 2014/07/09 2014.

- [10] S. M. George, "Atomic Layer Deposition: An Overview," *Chemical Reviews*, vol. 110, no. 1, pp. 111-131, 2010/01/13 2010.
- [11] S.-J. Won, J. R. Kim, S. Suh, N.-I. Lee, C. S. Hwang, and H. J. Kim, "Effect of Catalyst Layer Density and Growth Temperature in Rapid Atomic Layer Deposition of Silica Using Tris(tert-pentoxy)silanol," *ACS Applied Materials & Interfaces*, vol. 3, no. 5, pp. 1633-1639, 2011/05/25 2011.
- [12] S. H. Kim, N. Kwak, J. Kim, and H. Sohn, "A comparative study of the atomic-layer-deposited tungsten thin films as nucleation layers for W-plug deposition," *Journal of the Electrochemical Society*, vol. 153, no. 10, pp. G887-G893, 2006.
- [13] S. H. Kim *et al.*, "Atomic layer deposition of low-resistivity and high-density tungsten nitride thin films using B₂H₆, WF₆, and NH₃," *Electrochemical and Solid State Letters*, vol. 9, no. 3, pp. C54-C57, 2006.
- [14] J. W. Klaus, S. J. Ferro, and S. M. George, "Atomic layer deposition of tungsten using sequential surface chemistry with a sacrificial stripping reaction," *Thin Solid Films*, vol. 360, no. 1-2, pp. 145-153, Feb 1 2000.
- [15] C. H. Kim *et al.*, "Pulsed CVD-W Nucleation Layer Using WF₆ and B₂H₆ for Low Resistivity W," *Journal of the Electrochemical Society*, vol. 156, no. 9, pp. H685-H689, 2009.
- [16] G. L. Wang *et al.*, "Application of Atomic Layer Deposition Tungsten (ALD W) as Gate Filling Metal for 22 nm and Beyond Nodes CMOS Technology," *Ecs Journal of Solid State Science and Technology*, vol. 3, no. 4, pp. P82-P85, 2014.
- [17] T. Omstead, G. C. D' Couto, S. H. Lee, P. Wongsenakaum, J. Collins, and K. Levy, "Filling high-AR structures using pulsed nucleation layer deposition," *Solid State Technology*, vol. 45, no. 9, pp. 51-+, Sep 2002.
- [18] S. H. Kim *et al.*, "Characterizations of pulsed chemical vapor deposited-tungsten thin films for ultrahigh aspect ratio W-plug process," *Journal of the Electrochemical Society*, vol. 152, no. 6, pp. C408-C417, 2005.
- [19] H. Park, S. Lee, H. J. Kim, E. Yoon, and G.-D. Lee, "Dissociation reaction of B₂H₆ on TiN surfaces during atomic layer deposition: first-principles study," *RSC Advances*, 10.1039/C7RA11291B vol. 7, no. 88, pp. 55750-55755, 2017.

- [20] D. G. Sangiovanni, D. Edström, L. Hultman, I. Petrov, J. E. Greene, and V. Chirita, "Ab initio and classical molecular dynamics simulations of N₂ desorption from TiN(001) surfaces," *Surface Science*, vol. 624, pp. 25-31, 2014/06/01/ 2014.
- [21] D. G. Sangiovanni, A. B. Mei, L. Hultman, V. Chirita, I. Petrov, and J. E. Greene, "Ab Initio Molecular Dynamics Simulations of Nitrogen/VN(001) Surface Reactions: Vacancy-Catalyzed N₂ Dissociative Chemisorption, N Adatom Migration, and N₂ Desorption," *The Journal of Physical Chemistry C*, vol. 120, no. 23, pp. 12503-12516, 2016/06/16 2016.
- [22] D. G. Sangiovanni *et al.*, "Effects of surface vibrations on interlayer mass transport: Ab initio molecular dynamics investigation of Ti adatom descent pathways and rates from TiN/TiN(001) islands," *Physical Review B*, vol. 97, no. 3, p. 035406, 01/05/ 2018.
- [23] D. Edström, D. G. Sangiovanni, L. Hultman, V. Chirita, I. Petrov, and J. E. Greene, "Ti and N adatom descent pathways to the terrace from atop two-dimensional TiN/TiN(001) islands," *Thin Solid Films*, vol. 558, pp. 37-46, 2014/05/02/ 2014.
- [24] D. G. Sangiovanni, D. Edström, L. Hultman, I. Petrov, J. E. Greene, and V. Chirita, "Ti adatom diffusion on TiN(001): Ab initio and classical molecular dynamics simulations," *Surface Science*, vol. 627, pp. 34-41, 2014/09/01/ 2014.
- [25] D. G. Sangiovanni, D. Edström, L. Hultman, V. Chirita, I. Petrov, and J. E. Greene, "Dynamics of Ti, N, and TiN_{[1]_[2]} (\$x=1--3\$) ad molecule transport on TiN(001) surfaces," *Physical Review B*, vol. 86, no. 15, p. 155443, 10/22/ 2012.
- [26] D. G. Sangiovanni, F. Tasnádi, L. Hultman, I. Petrov, J. E. Greene, and V. Chirita, "N and Ti adatom dynamics on stoichiometric polar TiN(111) surfaces," *Surface Science*, vol. 649, pp. 72-79, 2016/07/01/ 2016. \equiv
- [27] Y. Ren, X. Liu, X. Tan, and E. Westkämper, "Adsorption and pathways of single atomistic processes on TiN (111) surfaces: A first principle study," *Computational Materials Science*, vol. 77, pp. 102-107, 2013/09/01/ 2013.
- [28] C. Tholander, B. Alling, F. Tasnádi, J. E. Greene, and L. Hultman, "Effect of Al substitution on Ti, Al, and N adatom dynamics on TiN(001), (011), and (111) surfaces," *Surface Science*, vol. 630, pp.

- 28-40, 2014.
- [29] S. H. Kim, S. J. Yeom, N. Kwak, and H. Sohn, "Phase and microstructure of ALD-W films deposited using B₂H₆ and WF₆ and their effects on CVD-W growth," *Journal of the Electrochemical Society*, vol. 155, no. 2, pp. D148-D154, 2008.
- [30] G. Ramanath *et al.*, "Electromigration in epitaxial Cu (001) lines," in *AIP Conference Proceedings*, 2002, vol. 612, no. 1, pp. 10-20: AIP.
- [31] C. H. Kim, I. C. Rho, S. H. Kim, Y. S. Sohn, H. S. Kang, and H. J. Kim, "Improvement of Adhesion Performances of CVD-W Films Deposited on B₂H₆-Based ALD-W Nucleation Layer," *Electrochemical and Solid State Letters*, vol. 12, no. 3, pp. H80-H83, 2009.
- [32] U. C. Oh and J. H. Je, "Effects of Strain-Energy on the Preferred Orientation of Tin Thin-Films," *Journal of Applied Physics*, vol. 74, no. 3, pp. 1692-1696, Aug 1 1993.
- [33] J. H. Je, D. Y. Noh, H. K. Kim, and K. S. Liang, "Preferred orientation of TiN films studied by a real time synchrotron x-ray scattering," *Journal of Applied Physics*, vol. 81, no. 9, pp. 6126-6133, May 1 1997.
- [34] J. P. Perdew, K. Burke, and M. Ernzerhof, "Generalized gradient approximation made simple," *Physical Review Letters*, vol. 77, no. 18, pp. 3865-3868, Oct 28 1996.
- [35] G. Kresse and J. Furthmüller, "Efficient iterative schemes for ab initio total-energy calculations using a plane-wave basis set," *Physical Review B*, vol. 54, no. 16, pp. 11169-11186, Oct 15 1996.
- [36] S. Grimme, "Semiempirical GGA-type density functional constructed with a long-range dispersion correction," *Journal of Computational Chemistry*, vol. 27, no. 15, pp. 1787-1799, 2006.
- [37] P. E. Blöchl, "Projector augmented-wave method," *Physical Review B*, vol. 50, no. 24, pp. 17953-17979, 12/15/ 1994.
- [38] N. Schönberg, "An X-Ray Investigation on Ternary Phases in the Ta-Ti-N, Ta-Cr-N, Ta-Mn-N, Ta-Fe-N, Ta-Co-N, Ta-Ni-N Systems," *Acta Chemica Scandinavica*, vol. 8, no. 2, pp. 213-220, 1954.
- [39] D. G. Sangiovanni, V. Chirita, and L. Hultman, "Electronic mechanism for toughness enhancement in TixM1-xN(M=Mo and W)", *Physical Review B*, vol. 81, no. 10, p. 104107, 03/15/ 2010.
- [40] D. G. Sangiovanni, B. Alling, P. Steneteg, L. Hultman, and I. A. Abrikosov, "Nitrogen vacancy, self-interstitial diffusion, and Frenkel-

- pair formation/dissociation in B1 TiN studied by ab initio and classical molecular dynamics with optimized potentials," *Physical Review B*, vol. 91, no. 5, p. 054301, 02/02/ 2015.
- [41] D. Vanderbilt, "Soft self-consistent pseudopotentials in a generalized eigenvalue formalism," *Physical Review B*, vol. 41, no. 11, pp. 7892-7895, 04/15/ 1990.
- [42] W. G. Aulbur, L. Jönsson, and J. W. Wilkins, "Quasiparticle Calculations in Solids," in *Solid State Physics - Advances in Research and Applications* vol. 54, ed, 1999, pp. 1-218.
- [43] J. K. Perry, J. Tahir-Kheli, and W. A. Goddard, "Antiferromagnetic band structure of La₂CuO₄: Becke-3-Lee-Yang-Parr calculations", *Physical Review B*, vol. 63, no. 14, p. 144510, 03/19/ 2001.
- [44] C. Adamo and V. Barone, "Toward reliable density functional methods without adjustable parameters: The PBE0 model," *The Journal of Chemical Physics*, vol. 110, no. 13, pp. 6158-6170, 1999.
- [45] J. Heyd, J. E. Peralta, G. E. Scuseria, and R. L. Martin, "Energy band gaps and lattice parameters evaluated with the Heyd-Scuseria-Ernzerhof screened hybrid functional," *The Journal of Chemical Physics*, vol. 123, no. 17, p. 174101, 2005.
- [46] K. Lassoued, M. Seydou, F. Raouafi, F. Larbi, P. Lang, and B. Diawara, "DFT study of the adsorption and dissociation of 5-hydroxy-3-butanedithiol-1,4-naphthaquinone (Jug-C4-thiol) on Au(111) surface," *Adsorption*, vol. 24, no. 2, pp. 191-201, 2018/02/01 2018.
- [47] N. Wang, Y. Liu, J. Zhao, and Q. Cai, "DFT-based study on the mechanisms of the oxygen reduction reaction on Co(acetylacetonate)₂ supported by N-doped graphene nanoribbon," *RSC Advances*, 10.1039/C6RA17651H vol. 6, no. 83, pp. 79662-79667, 2016.
- [48] N. Y. Dzade, A. Roldan, and N. H. de Leeuw, "DFT-D2 Study of the Adsorption and Dissociation of Water on Clean and Oxygen-Covered {001} and {011} Surfaces of Mackinawite (FeS)," *The Journal of Physical Chemistry C*, vol. 120, no. 38, pp. 21441-21450, 2016/09/29 2016.
- [49] N. Y. Dzade, A. Roldan, and N. H. d. Leeuw, "DFT-D2 simulations of water adsorption and dissociation on the low-index surfaces of mackinawite (FeS)," *The Journal of Chemical Physics*, vol. 144, no. 17, p. 174704, 2016.
- [50] J.-H. Yang, S.-B. Baek, and Y.-C. Kim, "Initial Surface Reaction of

- Di-Isopropylaminosilane on a Fully Hydroxyl-Terminated Si (001) Surface," *Journal of Nanoscience and Nanotechnology*, vol. 14, no. 10, pp. 7954-7960, // 2014.
- [51] D. Gall, S. Kodambaka, M. A. Wall, I. Petrov, and J. E. Greene, "Pathways of atomistic processes on TiN(001) and (111) surfaces during film growth: an ab initio study," *Journal of Applied Physics*, vol. 93, no. 11, pp. 9086-9094, 2003.
- [52] J. A. Dean, *Lange's handbook of chemistry*. McGraw-Hill, 1999.
- [53] B. Kalanyan, P. C. Lemaire, S. E. Atanasov, M. J. Ritz, and G. N. Parsons, "Using Hydrogen To Expand the Inherent Substrate Selectivity Window During Tungsten Atomic Layer Deposition," *Chemistry of Materials*, vol. 28, no. 1, pp. 117-126, 2016.

Chapter 5. Overall reaction mechanism for the early stages of W ALD on TiN surfaces

5.1. Introduction

Following Moore's law for decades, thin film deposition techniques have been intensively advanced to meet the demand for miniaturized and highly integrated devices in the electronics industry.[1] Recently, conformal film deposition techniques, which allows precise thickness control at atomic scale, are becoming very important.[2] Nitride materials, such as titanium nitride and silicon nitride, have been deposited using conventional deposition methods such as low-pressure chemical vapor deposition (LPCVD)[3-4], plasma-enhanced chemical vapor deposition (PECVD).[5-6] However, development of memory devices has required another deposition technique such as atomic layer deposition (ALD)[7-9] to meet the demand for excellent step coverage and high conformality on extremely high aspect ratio structures. The ALD processes utilize well-controlled sequential surface reactions to obtain uniform and conformal films.[10-11]

As one of the most essential materials in fabrication of future memory devices, tungsten (W) has been used for a metal gate with lower resistivity than other candidate materials, which results in enhancement of device performance.[12-13] In the fabrication of recent memory devices, tungsten films have been deposited using ALD by alternatively exposing W precursors such as tungsten hexafluoride (WF_6) and reducing agents such as diborane (B_2H_6) in an ABAB... sequence. In the ALD processes for W

deposition, B_2H_6 dosing process can play an important role in deposition of W films with low resistivity and in removal of residual fluorine (F) atoms on the surface.[14-16]

However, as the size of the memory device becomes smaller and smaller, it becomes difficult to deposit W films having excellent step coverage and conformality due to a severe problem that a seam or void is formed in the process of filling the W metal gate. This problem is a primary obstacle of the development for future memory devices.[17-18] To treat this problem, theoretical comprehension of the ALD process for W deposition is required due to the experimentally limited observations on the sub-nanometer scale. Although a few experimental results on ALD W have been reported, there has been no theoretical report on the overall reaction mechanism for ALD W process.

In our previous study[19], we reported that these severe problems, such as seam or void, in filling the W metal gate for memory devices would be attributed to the difference of deposition rate of W film depending on the orientations of TiN surfaces by analyzing dissociation reaction of B_2H_6 on three different TiN surfaces, such as TiN (001), Ti-terminated TiN (111), and N-terminated TiN (111) using density functional theory (DFT) calculation method. Since this previous study gives only information for B_2H_6 dosing process, we want to report how important the understanding of the overall ALD reaction mechanism could be for improving W deposition process. Motivation of this study is to find reliable W ALD process using DFT modeling for proposal of improved W ALD process as shown in **Figure 5.1**.

Here, we present first-principles study based on DFT calculation to explore overall ALD reaction mechanism for W deposition on the underlying

TiN surfaces well as the detailed dissociative reactions of WF_6 . From our DFT calculated re-sults, the structure of TiN surfaces can be changed depending on exposure to gas molecules, such as B_2H_6 , WF_6 , and H_2 . As a result, the changed structure of the TiN surfaces can have a significant impact on the ALD W process because the under-lying surfaces can have significant effects on the characteris-tics of the subsequent W nucleation layers.[20-21] The TiN sur-faces have been widely utilized as a glue/barrier layer for sub-sequent W nucleation.[22] Three different planes of TiN surfaces, TiN (001), Ti-terminated TiN (111), and N-terminated TiN (111) can be generated because poly-crystalline TiN layers with (001) and (111) preferred orientations were mainly ob-served in deposition of TiN films.[23-24] Our previous results[19] imply that B-covered surface can be generated very well by B_2H_6 flow especially on N-terminated TiN (111) surface ra-ther than other TiN surfaces due to even higher reactivity of B_2H_6 on the former than the latter.

In this study, both N-terminated TiN (111) and B-covered N-terminated TiN (111) surfaces were selected to compare sur-face reactivities of WF_6 . At the first step, the WF_6 decomposi-tion processes on both N-terminated TiN (111) and B-covered N-terminated TiN (111) surfaces were carefully analyzed in order to investigate the effect of the B-covered surface made by B_2H_6 . Then, at the second step, two additional reaction processes right after WF_6 bond dissociation, such as W substi-tution into B site and BF_3 desorption, were investigated to understand the detailed reactions that can occur by WF_6 flow. At the final step, we also studied the effect of H_2 post-treatment on W-covered N-terminated TiN (111) surface in order to remove residual F adatoms, which are known to cause severe problems that

extremely degrade characteristics of memory devices. It is expected that the understanding of the role of gas molecules used for W deposition gives us insight into improving the W ALD process for future memory devices.

W ALD deposition condition

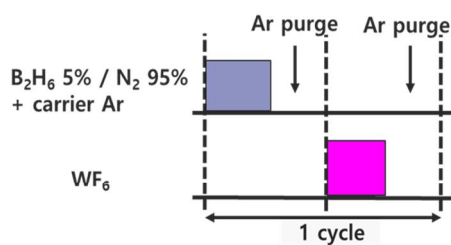


Figure 5.1. W ALD deposition condition and motivation of this study.

5.2. Computational methods

In our theoretical results, all DFT calculations were performed using Vienna ab initio simulation package (VASP) program with the Perdew-Burke-Ernzerhof (PBE) functional in the generalized gradient approximation (GGA).[25-26] We used PBE-D2 functional[27] based on projector augmented wave (PAW) method[28] with a correction to the conventional Kohn-Sham DFT energy to treat the van der Waals (vdW) interactions for all TiN surface calculations. TiN surfaces with B1-NaCl structure were used as the reactive surfaces with the WF_6 precursor. The optimized lattice parameter of TiN was $a_0 = 4.259 \text{ \AA}$, which overestimate somewhat the experimental value ($a_0 = 4.24 \text{ \AA}$)[29] since generally PBE functionals tend to overestimate the lattice parameters. For the N-terminated TiN (111) surface, a 5-layer slab of (2×2) supercell was considered with vacuum gaps of 25.6 \AA in the z direction were included to avoid interactions between adjacent slabs. For comparison, the B-covered N-terminated TiN surface was considered with a 5-layer slab of (2×2) supercell with vacuum gaps of 24.5 \AA . Valence orbitals were described by a plane-wave basis set with the cutoff energy of 400 eV . Electronic energies were calculated with a self-consistent-field (SCF) tolerance of 10^{-4} eV on the total energy. Ultrasoft Vanderbilt-type pseudopotentials[30] were used to describe the interactions between ions and electrons. A $3 \times 3 \times 3$ Monkhorst k-point mesh for bulk TiN was chosen. The Brillouin zone for all TiN surfaces was sampled with a $3 \times 3 \times 1$ Monkhorst-Pack k-point mesh. Geometry optimization was performed by minimizing the forces of all atoms to less than 0.02 eV/\AA with the total energy of the system converged to within 10^{-4} eV during self-consistent iterations. In addition, we

have calculated total energies for various configurations to determine the energy barrier for dissociative reactions of WF_6 on both TiN surfaces in the first step, for both W substitution and BF_3 desorption in the second step, and for both H_2 dissociative reaction and HF desorption in the final step.

To optimize adsorption structures, we considered two orientations and three positions of WF_6 on the N-terminated TiN surface. The details of all six cases are shown in **Figure 5.2**. The optimized adsorption structures with the lowest energy in the **Table 1** were used in this paper. We also checked two orientations and thirteen positions of WF_6 on the B-covered N-terminated TiN (111) surface. The details of all twenty-six cases are shown in **Figure 5.3**. The optimized adsorption structures with the lowest in **Table 2** were used in this study. The adsorption energy (E_{ads}) was calculated using

$$E_{\text{ads}} = E_{\text{tot,ads}} - (E_{\text{surf}} + E_{\text{pre}})$$

where $E_{\text{tot,ads}}$, E_{surf} , and E_{pre} are the total energy of the system after adsorption, and the energy of the surface only and the energy of the precursor only, respectively. The activation energy (E_a) was calculated using

$$E_a = E_{\text{tot,tran}} - E_{\text{tot,b.tr}}$$

where $E_{\text{tot,tran}}$ and $E_{\text{tot,ads}}$ are the total energy of the transition state and the total energy before transition, respectively. The reaction energy (E_{rxn}) was calculated using

$$E_{\text{rxn}} = E_{\text{tot,a.tr}} - E_{\text{tot,b.tr}}$$

where $E_{\text{tot,a.tr}}$, and $E_{\text{tot,b.tr}}$ are the total energies of the system after transition and after transition, respectively.

We considered two orientations and three positions of WF_6 on the N-terminated (111) TiN surface as shown in **Figures 2**. As for the two orientations, we construct two extreme geometries. Geometry 1 is that only

one fluorine atom of octahedral WF_6 is facing towards the surface, and Geometry 2 is that two fluorine atoms are facing towards the surface. Also, three different positions were considered on the surface.

We also checked two orientations and thirteen positions of WF_6 on the B-covered N-terminated (111) TiN surface as shown in **Figures 3**. The two orientations are same to the former case. Also, thirteen different positions were considered on the surface. The adsorption energies of WF_6 calculated on both N-terminated TiN (111) and B-covered N-terminated TiN (111) surfaces for each orientation and position were summarized in **Table 1-2**.

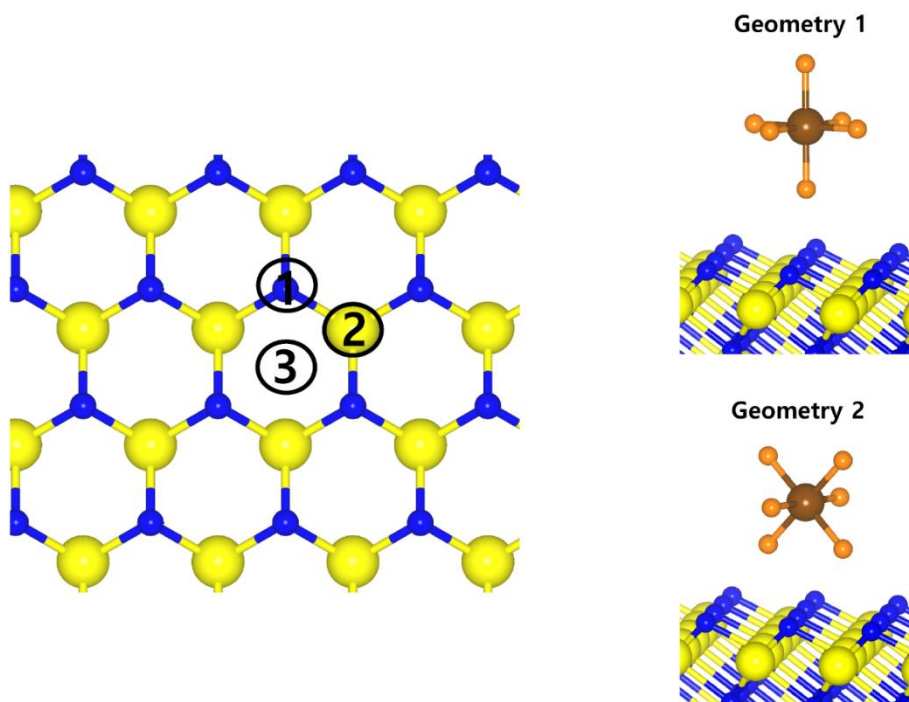


Figure 5.2. Two geometries and three positions of WF_6 on the N-terminated TiN (111) surface.

Geometry	Position	E_{ads} (eV)
1	1	0.05064
1	2	0.04548
1	3	0.00926
2	1	0.07967
2	2	0.03714
2	3	0.02117

Table 5.1. The adsorption energies of WF_6 calculated on the N-terminated TiN (111) surface for each orientation and position.

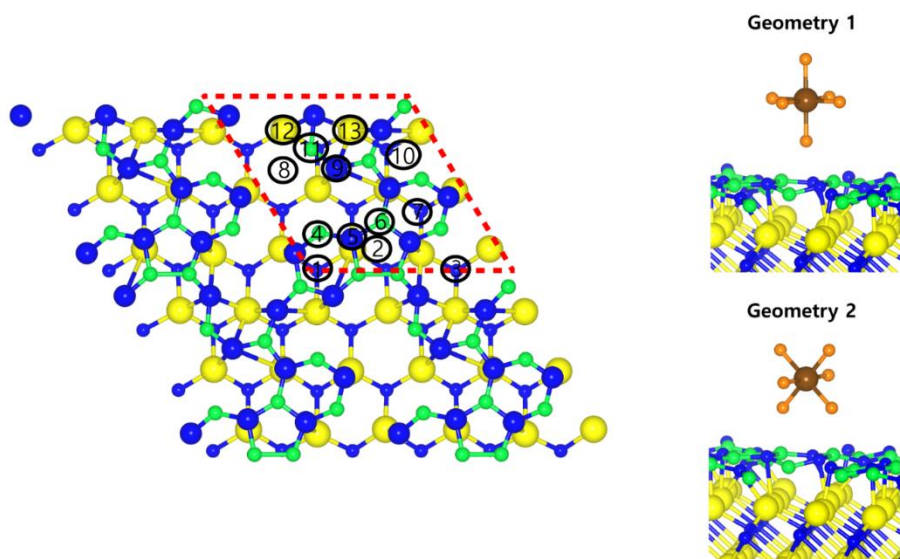


Figure 5.3. Two geometries and thirteen positions of WF_6 on the B-covered N-terminated TiN (111) surface.

Geometry	Position	E ads (eV)
1	1	-0.04537
1	2	-0.06495
1	3	-0.05904
1	4	-0.0066
1	5	-0.05118
1	6	-0.06022
1	7	-0.05046
1	8	-0.07439
1	9	-0.05701
1	10	-0.02979
1	11	-0.08477
1	12	-0.08292
1	13	-0.02978
2	1	-0.08673
2	2	-0.08427
2	3	-0.07326
2	4	-0.07035
2	5	-0.07278
2	6	-0.05566
2	7	-0.06183
2	8	-0.10041
2	9	-0.04205
2	10	-0.07557
2	11	-0.08042
2	12	-0.05213
2	13	-0.06605

Table 5.2. The adsorption energies of WF_6 calculated on the B-covered N-terminated TiN (111) surface for each orientation and position.

5.3. Results and discussion

5.3.1. Analysis of charge density distribution for prediction of the surface reactivity of WF_6 precursor

A broader terminology is applied to the very common case of reactions in which new σ bonds form between electron rich and electron poor regions of molecules. Nucleophiles (meaning nucleus seeking) are molecules that have relatively electron rich p bonds or lone pairs that act as electron sources for arrows making new bonds. Electrophiles (meaning electron seeking) are molecules with relatively electron poor atoms that serve as sinks for these arrows. Analogously, a molecule, or region of a molecule, that is a source for such an arrow is called nucleophilic, while a molecule or region of a molecule that is a sink for these arrows is referred to as being electrophilic. Based on this description, it should be clear that nucleophiles are analogous to Lewis bases and electrophiles are analogous to Lewis acids. Chemists use these terms interchangeably, although nucleophile and electrophile are more commonly used in kinetics discussions while Lewis acid and Lewis base are more commonly used in discussions about reaction thermodynamics as shown in **Figure 5.4**.^[31]

Figure 5.5 shows 3D electron density distribution of the op-timized structures of WF_6 precursor at 0.025 \AA^{-3} isosurface. It shows charge depletion around the W atom with electron loss of $5.34e$ and accumulation (pink area) in the vicinity of the F atom with electron gain of -0.89 . The amount of charge transfer was calculated by Bader charge analysis. **Figure 5.6 (a)**

shows 3D electron density distribution of the optimized structures of the N-terminated TiN (111) surface at 0.025 \AA^{-3} isosurface. The charge depletion around the Ti atom with electron loss of $2.43e$ and accumulation (pink area) in the vicinity of the N atoms with electron gain of $-1.55e$ can be seen. **Figure 5.6 (b)** exhibits 2D electron density map for top-layer of the same surface. **Figure 5.6 (a) and (b)** indicate that the N atoms with a high electron accumulation can be more accessible for electrophilic attack by WF_6 precursor due to the higher electron density and higher surface exposure than Ti atoms. Although the Ti atoms are somewhat positively charged, WF_6 precursor would predominantly interact with the N atoms of the first top-layer due to the shorter distance than the Ti atoms of the second top-layer. **Figure 5.7 (a)** shows 3D electron density distribution of the optimized structures of the B-covered N-terminated TiN (111) surface at 0.025 \AA^{-3} isosurface. It shows charge depletion around the Ti and B atoms with electron loss of $2.19e$ and $2.21e$, respectively.

Charge accumulation (pink area) in the vicinity of the N atoms with electron gain of $-2.99e$ can be seen. 2D electron density map of top-layer of the same surface is displayed in **Figure 5.7 (b)**. **Figure 5.7 (a) and (b)** indicate that the B atoms with a high electron depletion can be more accessible for nucleophilic attack by the lone pair electron on the F atom of WF_6 precursor, forming strong B-F bonding to be anchored on the B-covered N-terminated TiN (111) surface. The N atoms with a high electron accumulation can be electrophilic attacked by the W atom of the WF_6 precursor. Even though the Ti atoms are positively charged, WF_6 precursor would predominantly interact with the N and B atoms of the first top-layer due to the shorter distance than the Ti atoms of the second top-layer. **Table**

5.3 summarizes the bond lengths and amount of charge transfer of the optimized structures of N-terminated TiN (111), B-covered N-terminated TiN (111), and WF_6 precursor. Our results show that Ti-N bond length is elongated from 1.95 Å at the N-terminated TiN (111) to 2.13 Å at the B-covered N-terminated TiN (111) surface due to stronger B-N bonding nature (B-N bond length = 1.48 Å) than Ti-N one, which means that the amount of charge transfer between B and N atoms can increase, while decreasing the one between Ti and N atoms. This indicates that the surface reactivity of WF_6 precursor can be more favorable on the B-covered N-terminated TiN (111) surface than the former because the F atoms that acquire electrons can easily react with B atoms that lose electron, while W atom can react with N atom. In order to confirm the favorable reactivity of WF_6 on the B-covered N-terminated TiN (111) surface, overall reaction energetics for WF_6 bond dissociations were deeply analyzed in the following section.

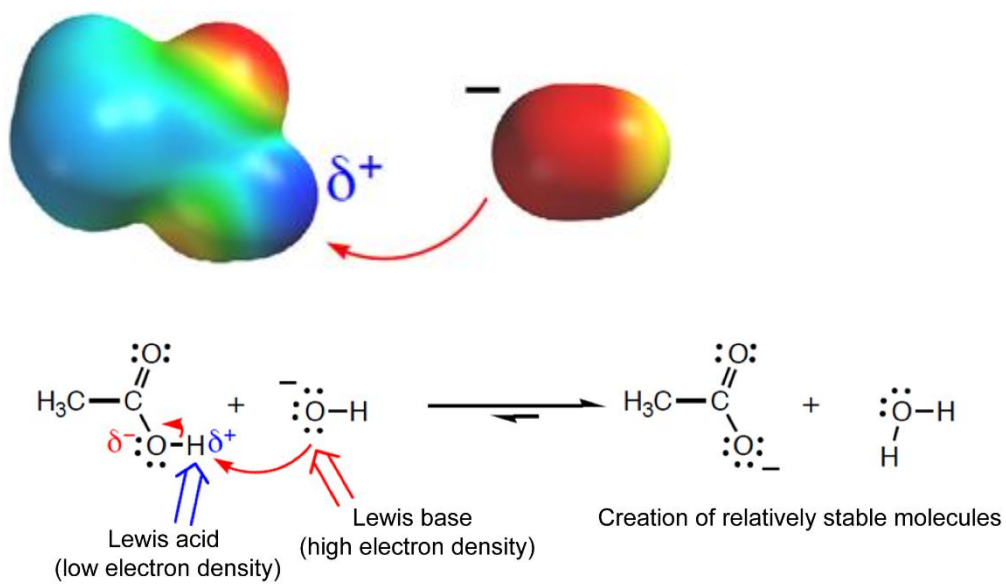


Figure 5.4. Description of Lewis Acid-Base Reaction. [31]

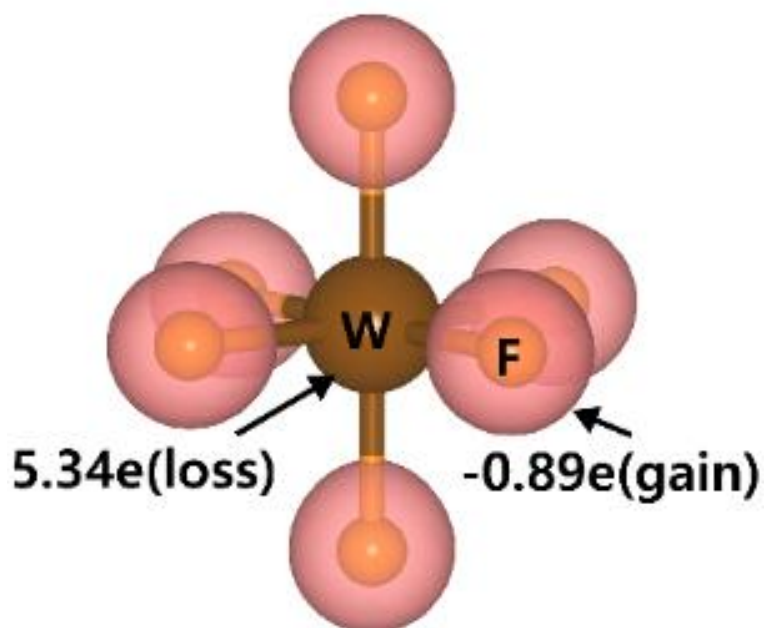


Figure 5.5. 3D electron density distribution of the optimized structure of the WF_6 precursor. Charge depletion around the W atom with electron loss of $5.34e$ and accumulation (pink area) in the vicinity of the F atom with electron gain of $-0.98e$ can be seen.

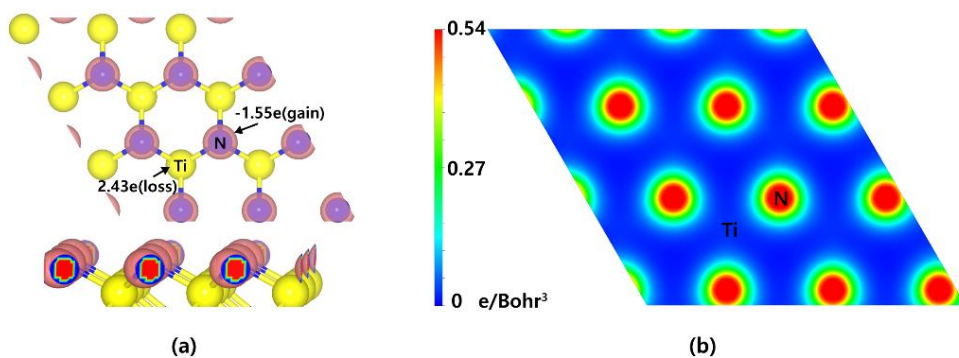


Figure 5.6. The optimized structure of the N-terminated TiN (111) surface: (a) 3D electron density of top and side views at 0.025 \AA^{-3} isosur-face. Charge depletion around the Ti atom with electron loss of $2.43e$ and accumulation (pink area) in the vicinity of the N atoms with electron gain of $-1.55e$ can be seen. (b) 2D electron density map for top-layer of the same surface.

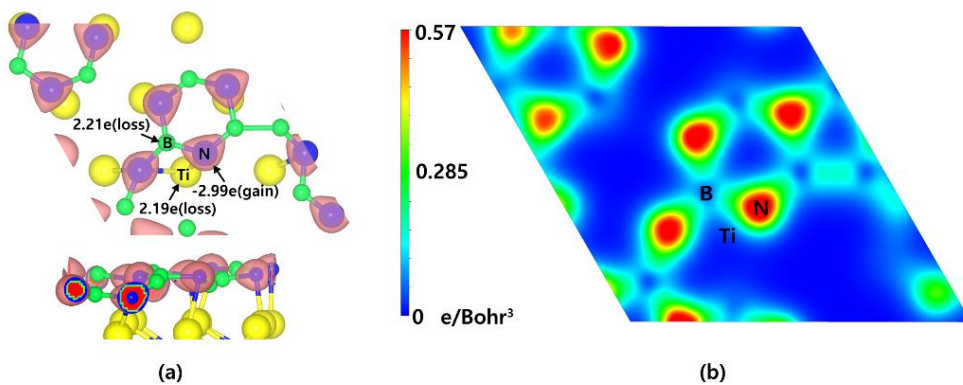


Figure 5.7. The optimized structure of the B-covered N-terminated TiN (111) surface: (a) 3D electron density of top and side views at 0.025 \AA^{-3} isosurface. It shows charge depletion around the Ti atom and B atom with electron loss of $2.19e$ and $2.21e$, respectively. Charge accumulation (pink area) in the vicinity of the N atoms with electron gain of $-2.99e$ can be seen. (b) 2D electron density map for top-layer of the same surface.

	N-terminated TiN (111)	B-covered N- terminated TiN (111)	WF₆ molecule
Bond length (Å)	Ti-N: 1.95	Ti-N: 2.13 B-N: 1.48	W-F: 1.86
ΔQ (e)	Ti: 2.43 (loss) N: -1.55 (gain)	Ti: 2.19 (loss) N: -2.99 (gain) B: 2.22 (loss)	W: 5.34 (loss) F: -0.89 (gain)

Table 5.3. Bond lengths (Å) and amount of charge transfer (e) of the optimized structures for N-terminated TiN (111), B-covered N-terminated TiN (111), and WF6 molecule.

5.3.2. Dissociative reaction of WF_6 on N-terminated TiN(111) surface

For ALD reaction to proceed, the WF_6 precursor first undergoes dissociative reaction on the TiN surfaces. The optimized structures of initial, transition, and final states for the first dissociative reaction step of WF_6 molecule on the N-terminated TiN (111) surface are shown in **Figure 5.8**. The calculated overall energy diagram of WF_6 decomposition on the N-terminated TiN (111) surface is shown in **Figure 5.9**. The initial state (IS) in **Figure 5.8** shows the optimized structure with the lowest adsorption energy of WF_6 on the surface, which is 0.01 eV. The final state (FS) presents that the dissociated F atom from the WF_6 molecule reacts with the N atom of the surface, and remaining WF_5 reacts with another N atom of the surface. The reaction energy can be calculated as the energy difference between the initial state and the final state. As shown in **Figure 5.9**, the calculated reaction energy of WF_6 for the first reaction step on the N-terminated TiN (111) surface is -0.39 eV. The first reaction step is kinetically difficult due to a high activation energy of 2.98 eV.

To complete the overall reaction energetics of WF_6 , the calculated energy diagram of WF_6 decomposition on the N-terminated TiN (111) surface is depicted in **Figure 5.9**. The detailed structures of WF_6 during the overall reactions on the N-terminated TiN (111) surface for transition state calculations can be found in **Figure 5.10 and Table 5.4**. During the dissociative reactions of the WF_6 molecule on the surface, this calculation shows that the overall reaction process is endothermic, with a calculated overall reaction energy of 4.73 eV. These results indicate that the reaction is thermodynamically unfavorable due to the uphill reactions. Furthermore,

WF₆ dissociative chemisorption on the N-terminated TiN (111) is kinetically difficult due to high activation energies that range from a minimum of 0.70 eV to a maximum of 3.45 eV. The low reactivity of WF₆ with the N-terminated TiN (111) surface might be attributed to weak N-F bonding nature, which makes it difficult for W-F bond breaking of WF₆ to occur. The weak N-F bonding nature may be originated from electron-withdrawing nature of both atoms due to high electronegativity of them (N = 3.04, F = 3.98), which causes N-F bonding nature to weaken, while strong bonding nature of B-N (B-N bond length = 1.48 Å) in **Table 5.3** may be attributed to the electron-donation nature of B atom and the electron-withdrawing nature of N atom, which causes B-N bond to strengthen.[32]

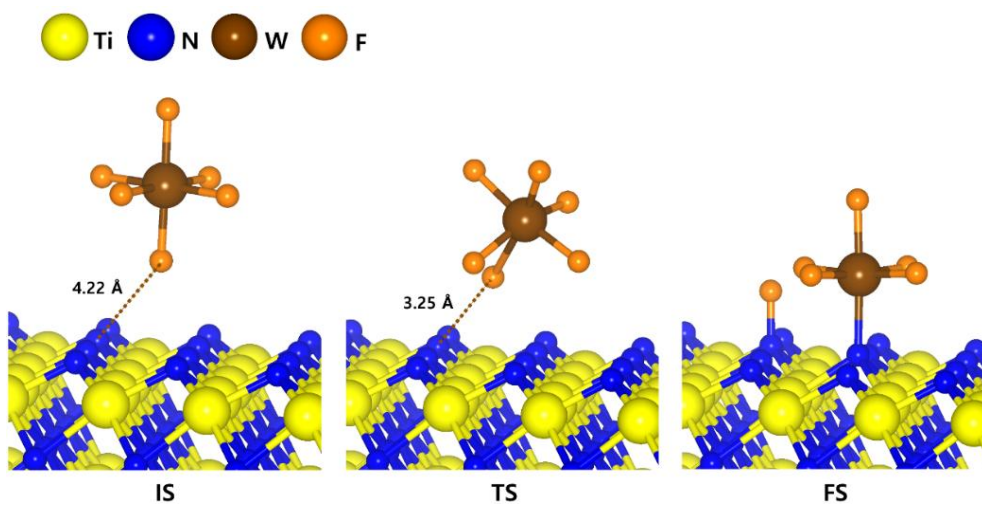


Figure 5.8. The optimized initial, transition, final structures for the first dissociative reaction step of WF_6 on the N-terminated TiN (111) surface.

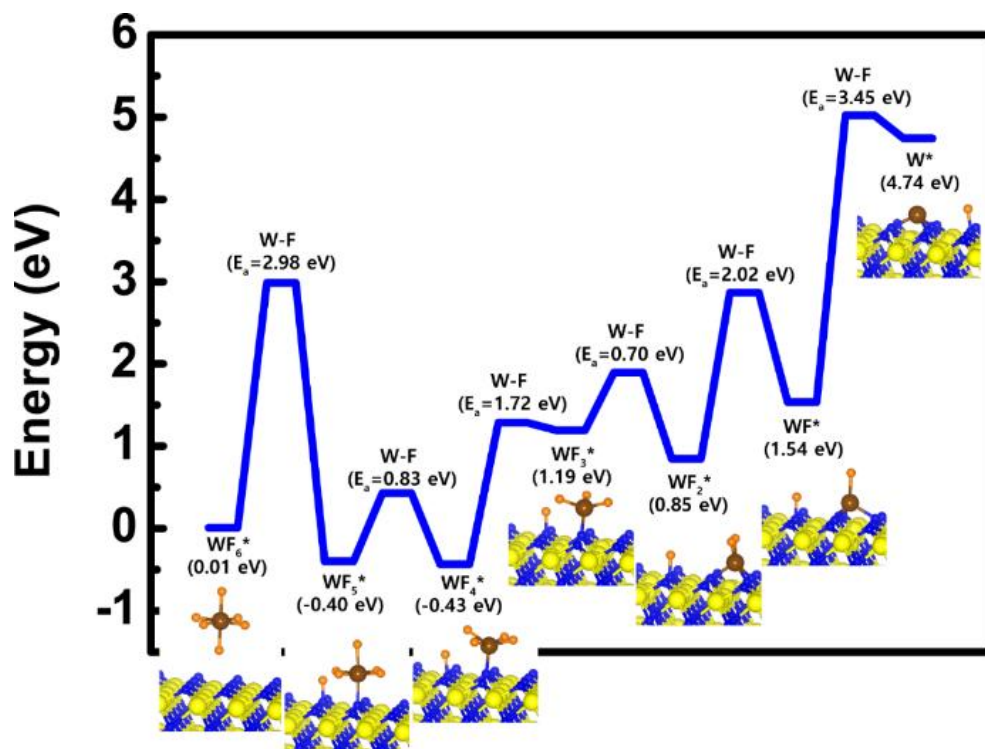
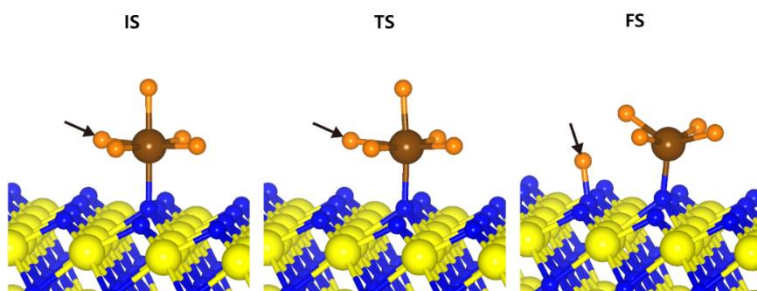
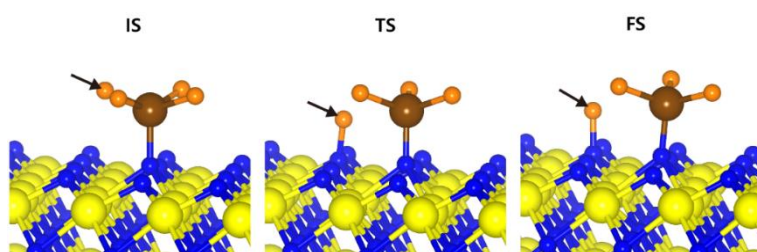


Figure 5.9. Calculated energy diagram of WF_6 decomposition on the N-terminated TiN (111) surface.

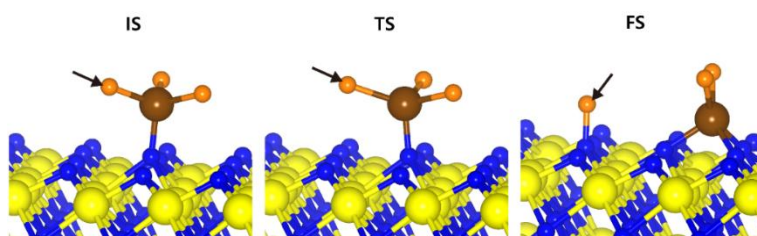
2nd reaction step : W-F bond dissociation



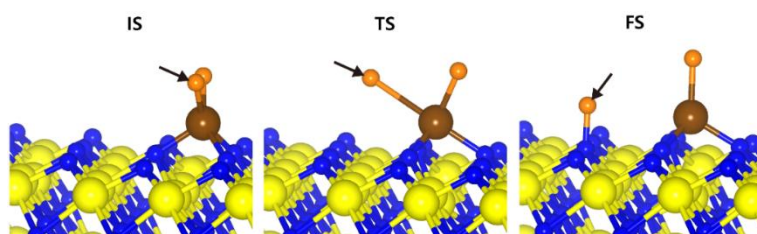
3rd reaction step : W-F bond dissociation



4th reaction step : W-F bond dissociation



5th reaction step : W-F bond dissociation



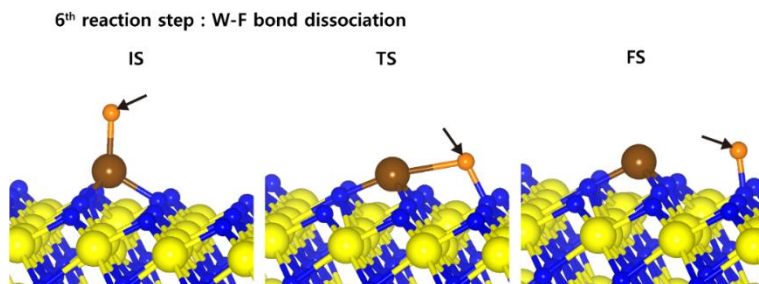


Figure 5.10. Calculated energy diagram of B_2H_6 decomposition on the Ti-terminated TiN (111) surface.

Reaction step	Bond dissociation	E_a (eV)	E_{rxn} (eV)
step 1	W-F	2.98	-0.39
step 2	W-F	0.83	-0.03
step 3	W-F	1.72	1.62
step 4	W-F	0.70	-0.34
step 5	W-F	2.02	0.69
step 6	W-F	3.45	3.20

Table 5.4. Calculated energy diagram of B_2H_6 decomposition on the Ti-terminated TiN (111) surface.

5.3.3. Dissociative reaction of WF_6 on B-covered N-terminated TiN(111) surface

After B_2H_6 flow on the N-terminated TiN (111) surface, B-covered N-terminated TiN (111) surface can be made due to energetically favorable reaction of B_2H_6 bond dissociation on the N-terminated TiN surface, which was confirmed by our previous report.[19] In order to estimate the difference between the N-terminated TiN (111) and B-covered N-terminated TiN (111) surfaces, the decomposition mechanism of WF_6 was also studied on the B-covered N-terminated TiN (111) surface. The optimized structures of initial, transition, and final states for the first dissociative reaction step of WF_6 molecule are shown in **Figure 5.11**. It was found that dissociated F atoms were adsorbed on the B atoms, and remaining WF_4 species was adsorbed on the N atom. The lowest adsorption energy of WF_6 on the B-covered N-terminated TiN (111) surface is -0.10 eV, showing that the adsorption is energetically favorable. The reaction energy from IS to FS during the first dissociative step of WF_6 is -0.28 eV, indicating that the reaction is exothermic with low activation energy of 0.19 eV.

To complete the overall reaction energetics of WF_6 , the calculated energy diagram of WF_6 decomposition on the B-covered N-terminated TiN (111) surface is shown in **Figure 5.12**. The detailed structures of WF_6 during the over-all reaction pathway on the surface for transition state calculations can be found in **Figure 5.13 and Table 5.5**. During the reaction of the WF_6 molecule, this calculation shows that the overall reaction process is exothermic, with a calculated overall reaction energy of -2.86 eV. This result indicates that WF_6 dissociative chemisorption on B-covered N-terminated

TiN (111) is energetically favorable due to the downhill reactions and low activation energies that range from a minimum of 0.19 eV to a maximum of 0.69 eV. WF_3 species has the highest activation energy of W-F bond dissociation among WF_x species, which implies that the W-F bond dissociation of WF_3 is the rate-determining step along the overall reaction.

Our calculated results suggest that the high reactivity of WF_6 with the surface is attributed to the presence of B-covered surface made by B_2H_6 with compared to bare surface as discussed above Section 5.3.3, proving that dis-sociative reaction of WF_6 is energetically unfavorable on the N-terminated TiN (111) surface. Aforementioned in Section 5.3.2, B-covered surface can have even larger reactivity with WF_6 molecule than the case of bare surface since the B atoms that lose electron can easily react with F atoms that acquire electrons, which induces W-F bond breaking of WF_6 to occur easily. This analysis was confirmed by higher binding energy of F adatom with the B-covered N-terminated TiN (111) than N-terminated TiN (111), the former is 6.3 eV and the latter is 3.6 eV in our calculations. As a result, an effect of the B_2H_6 flow on the surface is to make the TiN surface be reactive for WF_6 bond dissociation, meaning that the B_2H_6 serves as a catalyst to decompose WF_6 .

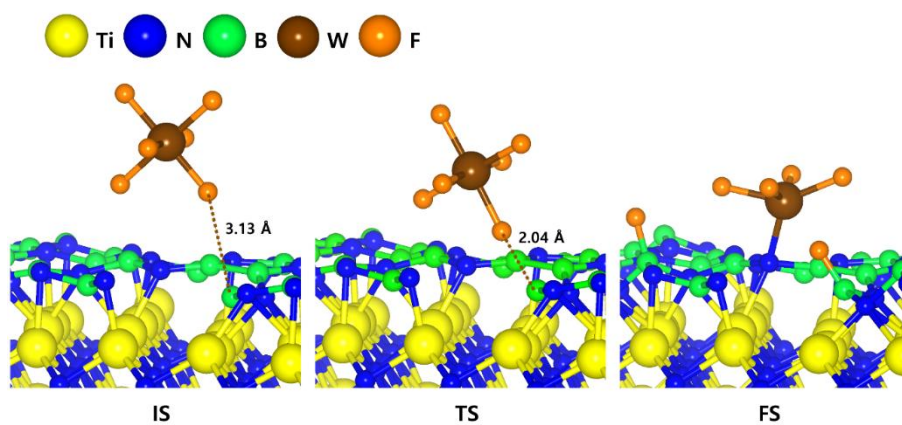
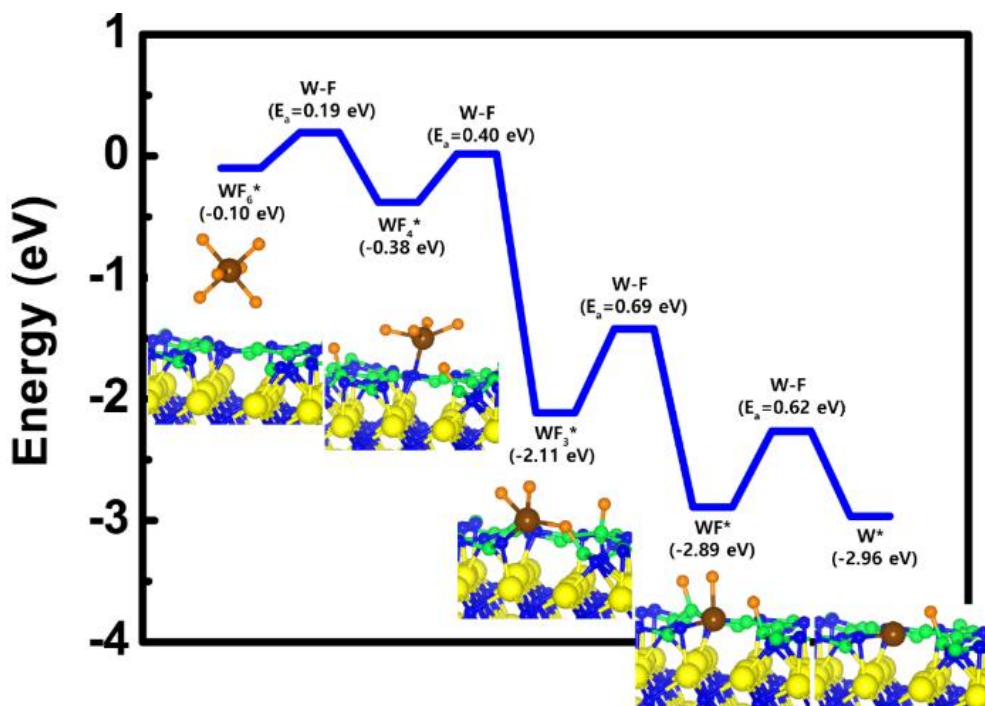


Figure 5.11. The optimized initial, transition, final structures for the first dissociative reaction step of WF_6 on the B-covered N-terminated TiN (111) surface.



Second half reaction

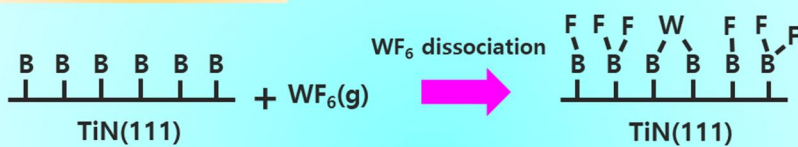


Figure 5.12. Calculated energy diagram of WF_6 decomposition on the B-covered N-terminated TiN (111) surface

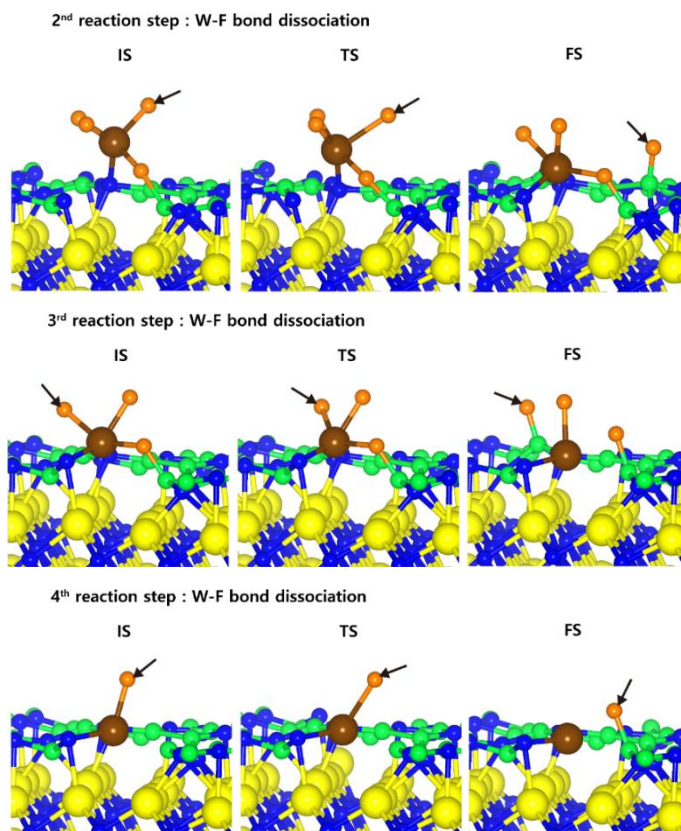


Figure 5.13. Initial (IS), transition (TS), and final (FS) states of intermediate reactions from 2nd reaction step to the 4th reaction step of WF_6 bond dissociation on the B-covered N-terminated TiN (111) surface.

Reaction step	Bond dissociation	E_a (eV)	E_{rxn} (eV)
step 1	W-F	0.19	-0.28
step 2	W-F	0.40	-1.73
step 3	W-F	0.69	0.78
step 4	W-F	0.62	-0.07

Table 5.5. Activation energies (E_a , eV) and reaction energies (E_{rxn} , eV) of WF_6 bond dissociation on the B-covered N-terminated TiN (111) surface.

5.3.4. Two additional reaction processes right after WF_6 bond dissociation; W substitution into B atom, BF_3 desorption

Right after WF_6 dissociative reaction on B-covered N-terminated TiN (111), two additional reaction processes can occur; W substitution and BF_3 desorption. For the first additional reaction process, the diffusion barrier of W adatom from atop (IS) to sub-layer (FS) was calculated to see if the W adatom can be substituted by B atoms in the sub-layer. As shown in **Figure 5.14 (a)**, it was found that during W adatom diffusion from IS to FS, B-N bonded atoms just below the W adatom were broken and pushed out to bond with other B, N atoms in the vicinity. This phenomenon is attributed to strong binding energy of W adatom with the TiN surface than other B and N atoms (W: 10.9 eV, B: 5.9 eV, N: 9.4 eV, F: 4.4 eV) in our calculations. This gives new information why the TiN surface is greatly suitable for adhesion layer of W thin films. **Figure 5.14 (b)** shows W adatom diffusion from atop (IS) to sub-layer (FS) with a low activation energy of 0.43 eV and large reaction energy of -7.37 eV, which means that the diffusion is energetically favorable. This indicates that W atoms can be covered on the TiN surfaces due to the strong bonding nature of W with the TiN surface rather than B atoms covered on the surface. As a result, W-covered N-terminated TiN (111) surface can be made by an additional process of W substitution. In addition, remaining atoms, such as B and F, can be adsorbed on the W-covered N-terminated TiN (111) surface due to lower binding energy of those atoms with the surface than the one of W atom.

For the second additional reaction process, energy diagram of BF_3 desorption was calculated to see if remaining B and F atoms can be desorbed

as BF_3 molecule. The calculated energy diagram of BF_3 desorption on the W-covered N-terminated TiN (111) surface is shown in **Figure 5.15**. The detailed structures during the overall reaction pathway on the surface for transition state calculations can be found in **Figure 5.16 and Table 5.6**. During the reaction for BF_3 desorption, this calculation shows that the overall reaction process is exothermic, with a calculated overall reaction energy of -0.69 eV. This result indicates that BF_3 desorption on W-covered N-terminated TiN (111) is energetically favorable due to the downhill reactions and low activation energies that range from a minimum of 0.25 eV to a maximum of 0.72 eV. As a result, right after W substitution, remaining B and F atoms can be easily desorbed as by-product, that is, BF_3 molecule on the W-covered N-terminated TiN (111) surface.

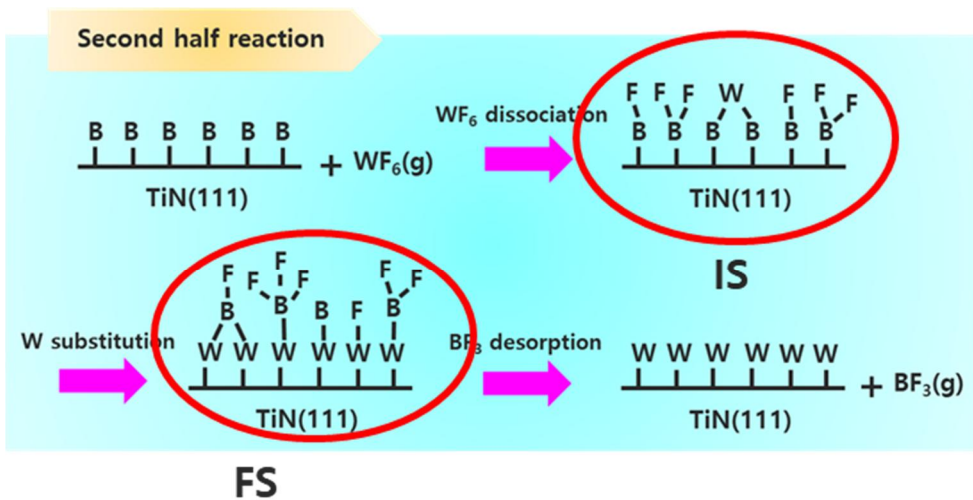
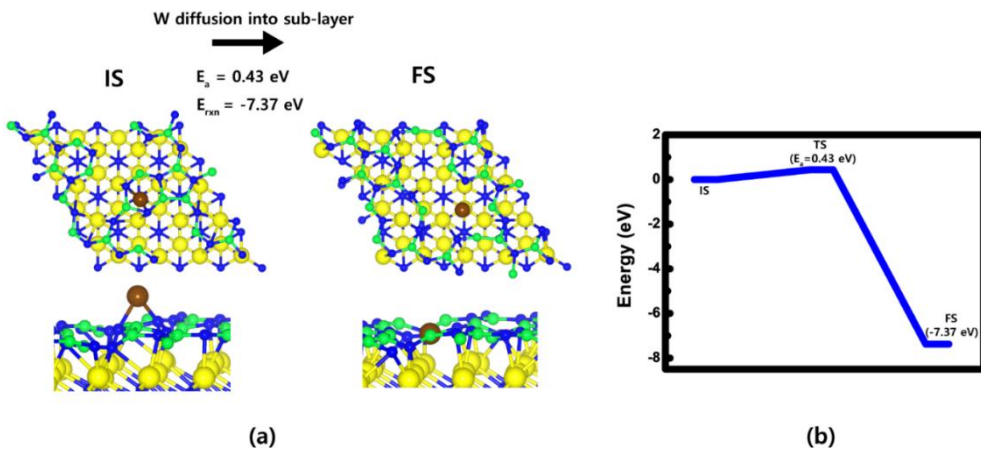


Figure 5.14. W adatom diffusion from atop (IS) to sub-layer (FS): (a) top and side views of W adatom on B-covered N-terminated TiN (111) surfaces. (b) energy profile.

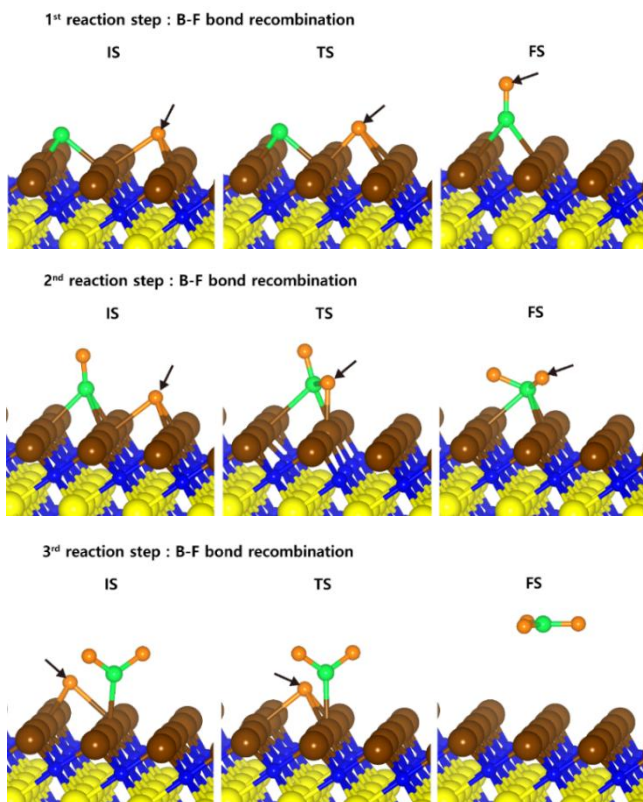


Figure 5.16. Initial (IS), transition (TS), and final (FS) states of intermediate reactions from 1st reaction step to the 3rd reaction step of BF_3 desorption on the W-covered N-terminated TiN (111) surface.

Reaction step	Bond recombination	E_a (eV)	E_{rxn} (eV)
step 1	B-F	0.29	-0.71
step 2	B-F	0.25	-0.10
step 3	B-F	0.72	0.12

Table 5.6. Activation energies (E_a , eV) and reaction energies (E_{rxn} , eV) of B-F bond recombination on the W-covered N-terminated TiN (111) surface.

5.3.5. H₂ post-treatment for removal of F adatoms

Even though F adatoms can be removed by BF₃ desorption, it may be difficult to completely remove F adatoms on the W-covered N-terminated TiN (111) surface because a large number of F adatoms can be generated right after WF₆ dissociative reaction, which means that it is difficult to remove too many F adatoms by BF₃ desorption. In fact, these residual F adatoms cause severe problems, such as, attack on under-layer materials and degradation of performance of memory devices, which is because F atoms with highly electron withdrawing nature have strong reactivity on other atoms with electron donation nature, such as Al, B, Si, etc., leading to breaking the atomic bond of under-layer materials.[33,34] In order to see if F adatoms can be removed by HF desorption, we investigated the effect of H₂ post-treatment on W-covered N-terminated TiN (111) surface.

The calculated energy diagrams of H₂ dissociation on the W-covered N-terminated TiN (111) and HF desorption on the H-saturated W-covered N-terminated TiN (111) surface are shown in **Figure 5.17 (a) and (b)**, respectively. As for the first reaction step in **Figure 5.17 (a)**, it shows that H₂ dissociative reaction is energetically favorable, with a reaction energy of -1.22 eV and a low activation energy of 0.26 eV. This indicates that the injection of H₂ molecule makes the W-covered N-terminated TiN (111) surface be the H-saturated surface. The detailed structures during the overall reaction pathway on the surface for transition state calculations can be found in **Figure 5.18 and Table 5.7**.

As for the second reaction step in **Figure 5.17 (b)**, it shows that HF desorption is energetically unfavorable, with a reaction energy of 0.85 eV and

an activation energy of 1.17 eV. However, the forward reaction $[H(s) + F(s) \rightarrow HF(g)]$ can be increased under H_2 ambience since large amount of H adatoms generated by H_2 dissociation can increase the frequency of the forward reaction, which results in enhancing the reaction rate. In addition, the forward reaction may occur well under somewhat high temperature due to a bit high activation energy. In previous experimental study, Berç Kalanyan et al.[35] reported that adding H_2 with WF_6 molecule promotes HF formation during the ALD process of W deposition as shown **Figure 5.19**. The combination of their results and our results provides how to effectively remove residual F atoms on the TiN surface.

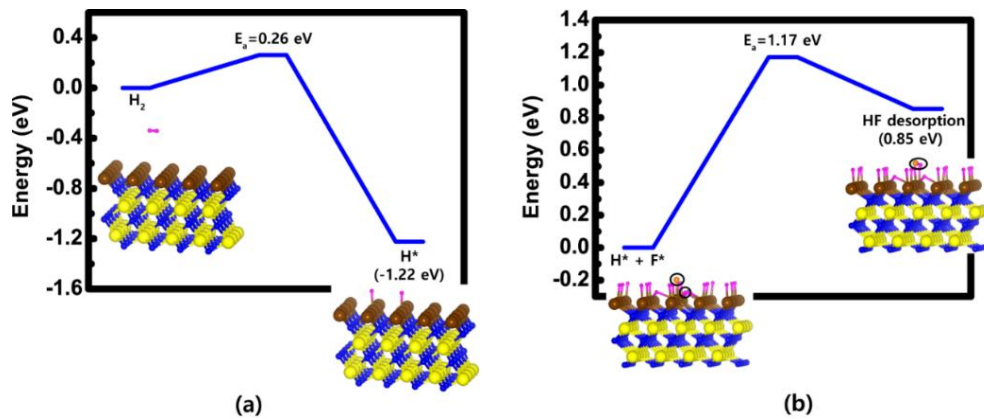


Figure 5.17. Calculated energy diagram of (a) H₂ dissociation on the W-covered N-terminated TiN (111) surface and (b) HF desorption on the H-saturated W-covered N-terminated TiN (111) surface.

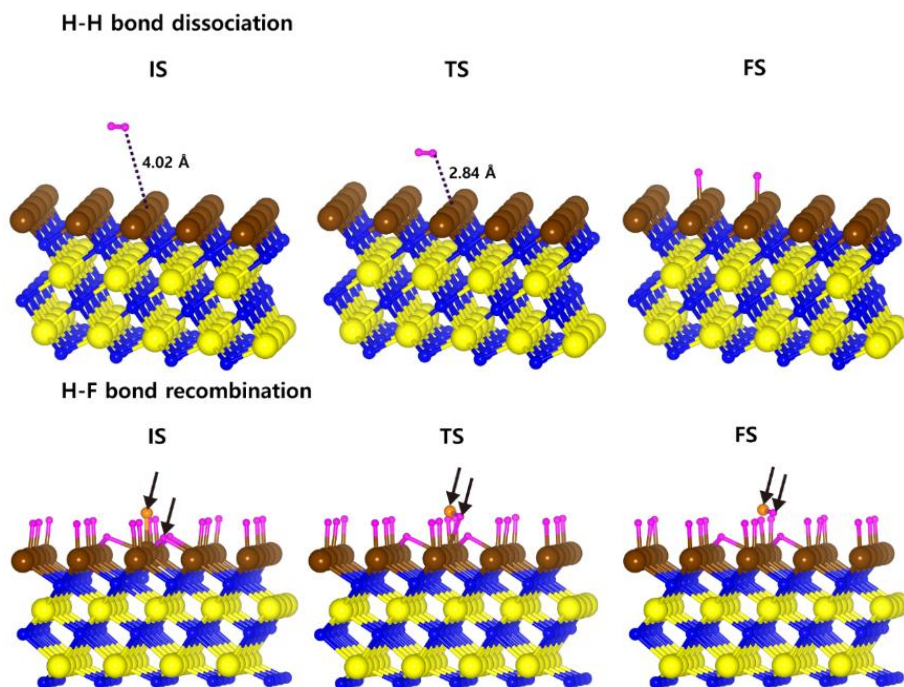


Figure 5.18. Initial (IS), transition (TS), and final (FS) states of H₂ bond dissociation and HF desorption on the W-covered N-terminated TiN (111) surface.

Bond dissociation	E_a (eV)	E_{rxn} (eV)
H-H	0.26	-1.22
Bond recombination	E_a (eV)	E_{rxn} (eV)
H-F	1.17	0.85

Table 5.7. Activation energies (E_a , eV) and reaction energies (E_{rxn} , eV) of H₂ bond dissociation and HF desorption on the W-covered N-terminated TiN (111) surface.

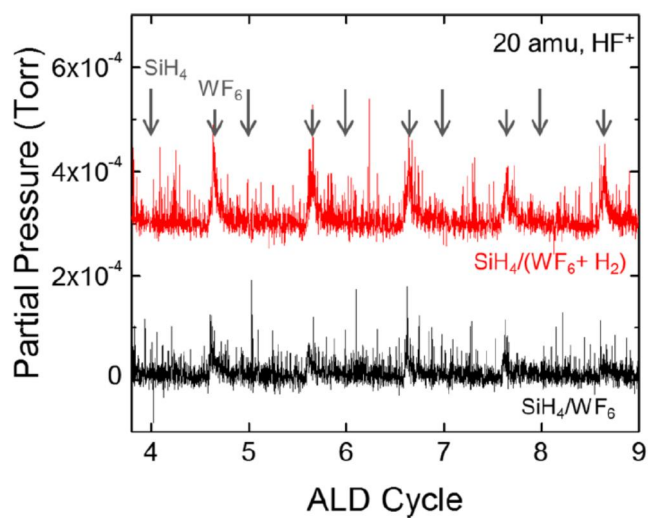


Figure 5.19. Mass spectrometry results of W ALD using $\text{SiH}_4/(\text{WF}_6 + \text{H}_2)$ and SiH_4/WF_6 . [35]

5.3.6. Proposed overall ALD reaction mechanism for W deposition

In order to summarize overall ALD reaction mechanism for W deposition as above discussed in Section 5.3.1-5.3.5, we drew the overall ALD reaction scheme for clear understanding of W deposition. **Figure 5.20** shows proposed overall ALD reaction scheme for W deposition. At the process 1 for B_2H_6 flow, there are two reaction steps; B_2H_6 dissociative reaction and H_2 desorption. It shows that B_2H_6 dissociative reaction is easy to occur on the N-terminated TiN (111) due to low activation energies ($E_{a, \min} =$ barrier-less, $E_{a, \max} = 0.39$ eV) and overall reaction energy ($E_{rxn, overall} = -19.0$ eV), which was reported in our previous results.[19] Therefore, B-covered N-terminated TiN (111) surface can be made by B_2H_6 flow. The re-maining H adatoms on the surface can be desorbed as H_2 molecule with activation energy ($E_a = 0.81$ eV) and reaction energy ($E_{rxn} = 0.48$ eV) under B_2H_6 ambience because large amount H adatoms generated by B_2H_6 dissociation can increase the frequency of the forward reaction [$H(s) + H(s) \rightarrow H_2(g)$] even though the reaction energy is positive value. At the process 2 for WF_6 flow, there are three reaction steps; WF_6 dissociative reaction, W substitution, and BF_3 desorption. It shows that all three reaction steps are easy to occur due to low activation energies and overall reaction energies as above discussed in Section 5.3.3-5.3.5. At the process 3 for the effect of H_2 post-treatment, there are two reaction steps; H_2 dissociative reaction, HF desorption. It shows that both H_2 dissociative reaction and HF desorption can occur enough well as above discussed in Section 5.3.5, therefore, a uniform W film could be deposited by removing residual F adatoms, which extremely degrade device performance.

Our results indicate that the understanding of the role of gas molecules used for W deposition plays an important role in improving the properties of the subsequent W nucleation layers during the W ALD process.

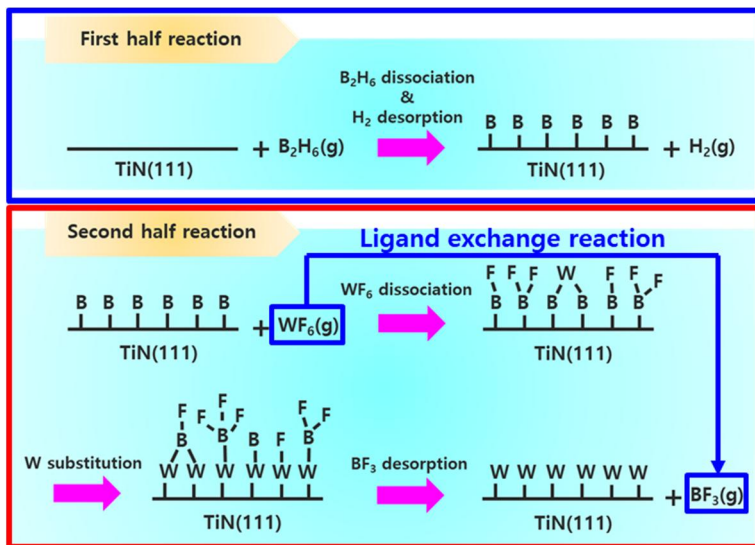
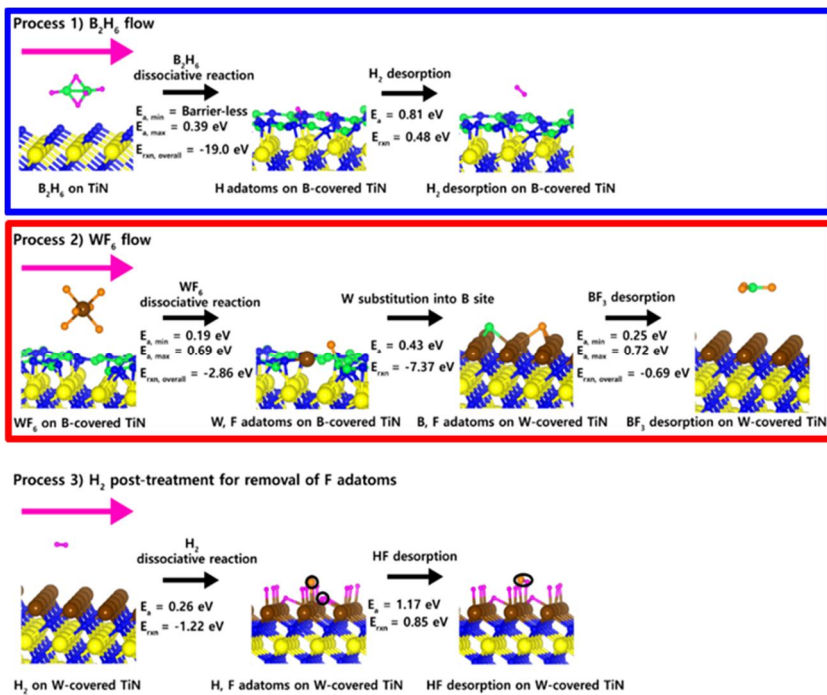


Figure 5.20. Proposed overall ALD reaction mechanism for W deposition.

5.4. Future work

In order to develop next-generation highly integrated memory semiconductor chips, most of the existing CVD processes are being replaced by ALD processes capable of conformal & uniform thin film deposition. Basically, CVD and ALD differ in the thin film deposition mechanism. In the case of the CVD process, the thin film deposition takes place by the "precursor [mass] transport limited reaction" mechanism which depends on the precursor flow rate in the high temperature process in which two kinds of precursors are completely decomposed. Thin film thickness increases linearly with pulse time. In CVD, since two precursors are implanted at one time, uneven heterogeneous growth occurs due to various complicated chemical reactions, which limits the precise thickness control.

In the case of the ALD process, a "self-limited reaction" in which the reaction is limited by the pre-adsorbed precursor, as in the case of thin film deposition in a low-temperature process where the surface is adsorbed rather than decomposed by elongating the purging between the two precursors, Mechanism enables atomic layer thickness control. The precursor used in the ALD process can be present in the gas, liquid, or solid form at room temperature and is selected from organic compounds, inorganic compounds, or organometallic compounds. The importance of precursor selection in the success or failure of the ALD process can not be overestimated several times, especially in semiconductor-related ALDs that require more complex and detailed structures in three dimensions with the development of the semiconductor industry. In the ALD precursor screening step, the precursors having the lowest energy values are selected through the calculation of the

density functional theory (DFT) based on quantum mechanics based on ligand-exchange reaction energy values in the gas phase as shown in **Figure 5.21**.

The ALD mass production process has been tried through trial-and-error without analyzing the precursors' chemical reaction and deposition mechanism. Recently, there are problems in the ALD process that can not be analyzed by complex chemical reaction and thin film growth mechanism. For example, in the case of a 1 nm thick ALD deposition, the problem of actually growing into an island shape without forming a layer and void formation at a slightly thicker thickness actually occurs. In order to solve these problems, it is necessary to accurately analyze the physicochemical phenomena occurring on the atomic scale by quantum computation. Furthermore, it is necessary to develop a quantitative computation technique which can reproduce experimentally, thereby reducing time & cost consuming procedures, it is essential to minimize. For the selected precursor, the chemical reaction with the surface is calculated by DFT, and all the reactants that can be formed on the surface are analyzed and the information is stored as the input value. As shown in **Figure 5.22**, they developed an algorithm that repeatedly adsorbs the input value until it saturates from the surface to the monolayer, and performs structural optimization with molecular dynamics simulation at the moment of layer formation. In 2018, an experimental ALD simulation technique was developed and reported for the first time in the Jeremy S. Luterbacher group, Switzerland, for both Al_2O_3 and SiO_2 materials. However, this is the case when the substrate material and thin film material are coincident and only very limited information is provided. Generally, experimental results are different according to substrate material and thin

film material. Therefore, development of ALD simulation technique is required for various materials through collaborative research with experimental team and finally develop technology to provide information on the web for the future work.

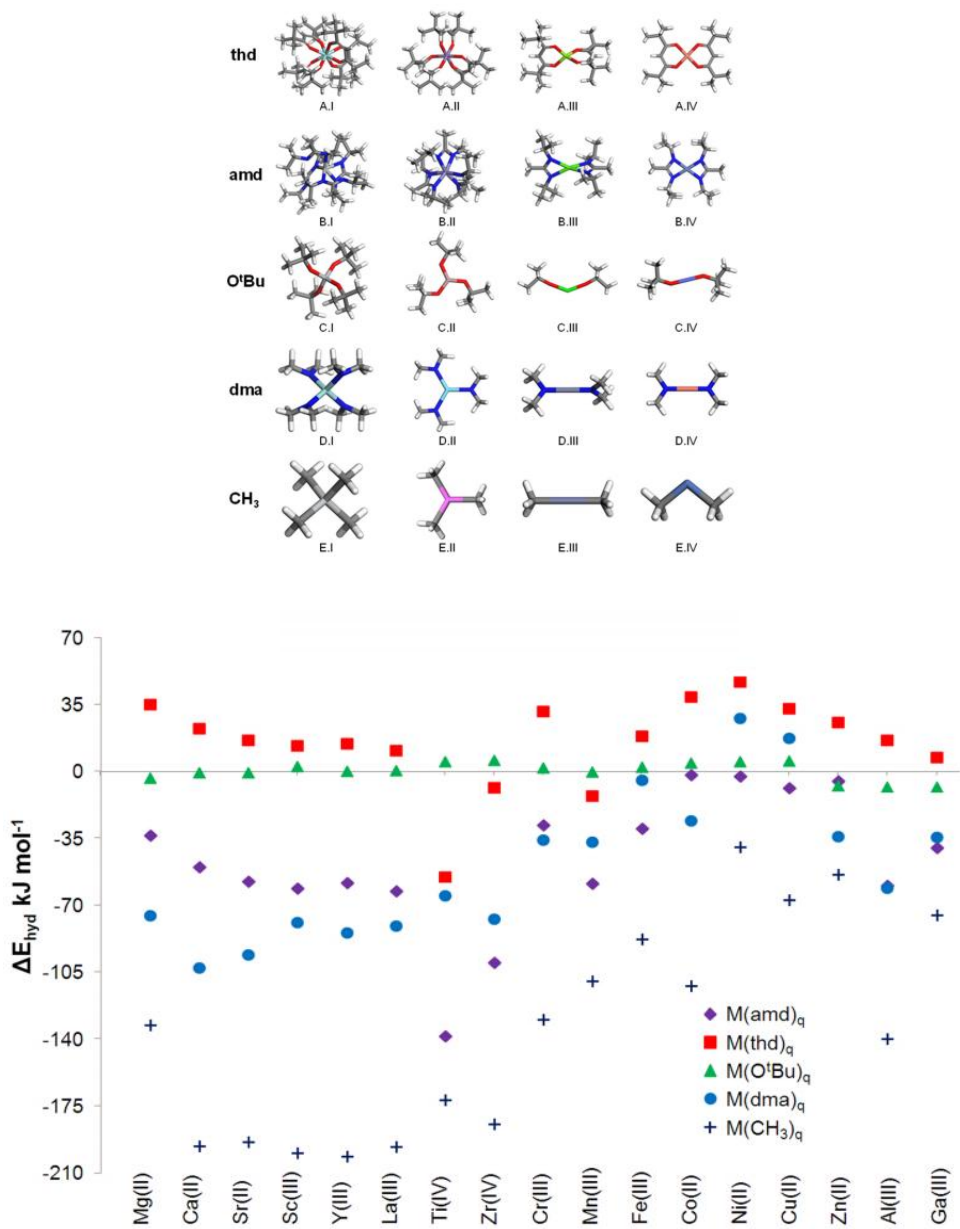


Figure 5.21. DFT optimized various metal precursors and DFT calculated energies of hydrolysis in gas phase for various metal precursors. [36]

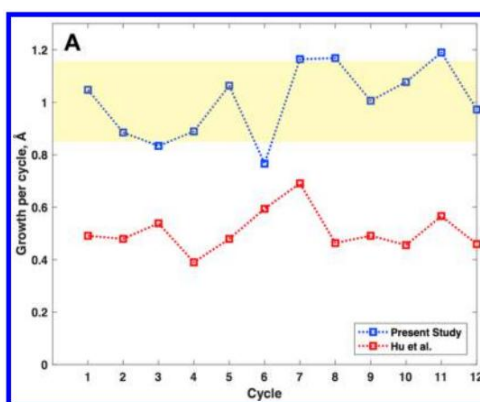
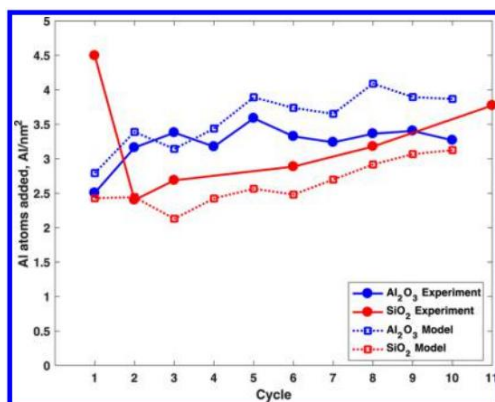
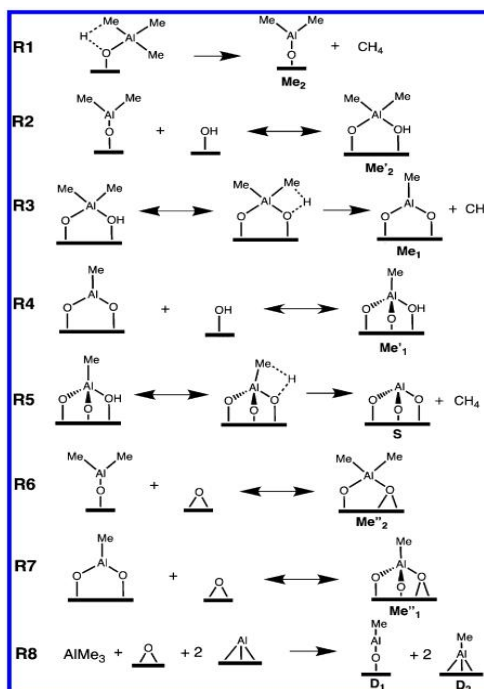
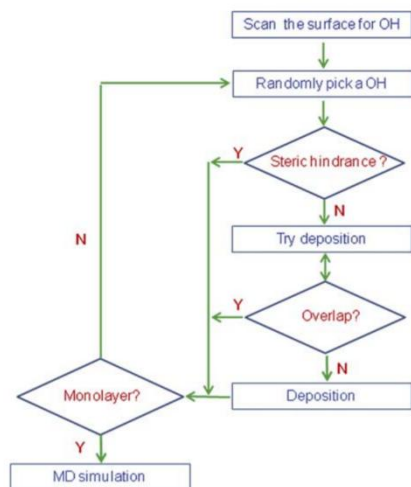


Figure 5.22. Surface saturation algorithm Al₂O₃ dep. on Al₂O₃ surface (upper left) and TMA reaction pathways confirmed by DFT (upper right), Similarity of growth rate between MD simulation and experiments (lower) [37,38]

5.5. Summary

In summary, we investigated overall ALD reaction mechanism for W deposition on the TiN surfaces based on DFT calculation as well as the detailed dissociative reactions of WF_6 . Our calculated results suggest that the overall reactions of the WF_6 on the B-covered TiN surfaces are energetically much more favorable than the one on the TiN surfaces, which means that the high reactivity of WF_6 with the B-covered TiN surface is attributed to the presence of B-covered surface made by B_2H_6 molecule. As a result, an effect of the B_2H_6 flow serves as a catalyst to decompose WF_6 molecule. Two additional reaction processes right after WF_6 bond dissociation, such as W substitution and BF_3 desorption, were also explored to clearly understand the detailed reactions that can occur by WF_6 flow. At the first additional reaction process, W atoms can be substituted into B site and covered on the TiN surfaces due to the strong bonding nature of W with the TiN surface than B atoms. At the second additional reaction process, remaining atoms, such as B and F, can be easily desorbed as by-product, that is, BF_3 . Furthermore, we also investigated the effect of H_2 post-treatment on W-covered TiN surface in order to remove residual F adatoms, which are known to cause severe problems that extremely degrade characteristics of memory devices. It was found that both H_2 dissociative reaction and HF desorption can occur enough well under somewhat high temperature and H_2 ambience, which is confirmed by the our DFT results and previously reported experimental results. These results imply that the understanding of the role of gas molecules used for W deposition gives us insight into improving the W ALD process for future memory devices.

5.6. Bibliography

- [1] S.-B. Baek, D.-H. Kim, and Y.-C. Kim, "Adsorption and surface reaction of bis-diethylaminosilane as a Si precursor on an OH-terminated Si (001) surface," *Applied Surface Science*, vol. 258, no. 17, pp. 6341-6344, 2012/06/15/ 2012.
- [2] M. C. Schwille *et al.*, "Experimental and simulation approach for process optimization of atomic layer deposited thin films in high aspect ratio 3D structures," *Journal of Vacuum Science & Technology A*, vol. 35, no. 1, p. 01B118, 2017.
- [3] W. D. Huang *et al.*, "Low temperature PECVD SiNx films applied in OLED packaging," *Materials Science and Engineering B-Solid State Materials for Advanced Technology*, vol. 98, no. 3, pp. 248-254, Apr 15 2003.
- [4] A. El Amrani, A. Bekhtari, B. Mahmoudi, A. Lefgoum, and H. Menari, "Experimental study of the effect of process parameters on plasma-enhanced chemical vapour deposition of silicon nitride film," *Vacuum*, vol. 86, no. 4, pp. 386-390, 2011/11/11/ 2011.
- [5] N. Sharma, M. Hooda, and S. K. Sharma, "Synthesis and Characterization of LPCVD Polysilicon and Silicon Nitride Thin Films for MEMS Applications," *Journal of Materials*, vol. 2014, p. 8, 2014, Art. no. 954618.
- [6] B. C. Joshi, G. Eranna, D. P. Runthala, B. B. Dixit, O. P. Wadhawan, and P. D. Vyas, *LPCVD and PECVD silicon nitride for microelectronics technology*. 2000, pp. 303-309.
- [7] W. J. Lee, J. H. Lee, C. O. Park, Y. S. Lee, S. J. Shin, and S. K. Rha, "A comparative study on the Si precursors for the atomic layer deposition of silicon nitride thin films," *Journal of the Korean Physical Society*, vol. 45, no. 5, pp. 1352-1355, Nov 2004.
- [8] J. W. Klaus, A. W. Ott, A. C. Dillon, and S. M. George, "Atomic layer controlled growth of Si₃N₄ films using sequential surface reactions," *Surface Science*, vol. 418, no. 1, pp. L14-L19, 1998/11/27/ 1998.
- [9] C. A. Murray, S. D. Elliott, D. Hausmann, J. Henri, and A. LaVoie, "Effect of Reaction Mechanism on Precursor Exposure Time in Atomic Layer Deposition of Silicon Oxide and Silicon Nitride," *ACS Applied Materials & Interfaces*, vol. 6, no. 13, pp. 10534-10541, 2014/07/09 2014.

- [10] S. M. George, "Atomic Layer Deposition: An Overview," *Chemical Reviews*, vol. 110, no. 1, pp. 111-131, 2010/01/13 2010.
- [11] S.-J. Won, J. R. Kim, S. Suh, N.-I. Lee, C. S. Hwang, and H. J. Kim, "Effect of Catalyst Layer Density and Growth Temperature in Rapid Atomic Layer Deposition of Silica Using Tris(tert-pentoxy)silanol," *ACS Applied Materials & Interfaces*, vol. 3, no. 5, pp. 1633-1639, 2011/05/25 2011.
- [12] S. H. Kim, N. Kwak, J. Kim, and H. Sohn, "A comparative study of the atomic-layer-deposited tungsten thin films as nucleation layers for W-plug deposition," *Journal of the Electrochemical Society*, vol. 153, no. 10, pp. G887-G893, 2006.
- [13] S. H. Kim *et al.*, "Atomic layer deposition of low-resistivity and high-density tungsten nitride thin films using B₂H₆, WF₆, and NH₃," *Electrochemical and Solid State Letters*, vol. 9, no. 3, pp. C54-C57, 2006.
- [14] J. W. Klaus, S. J. Ferro, and S. M. George, "Atomic layer deposition of tungsten using sequential surface chemistry with a sacrificial stripping reaction," *Thin Solid Films*, vol. 360, no. 1-2, pp. 145-153, Feb 1 2000.
- [15] C. H. Kim *et al.*, "Pulsed CVD-W Nucleation Layer Using WF₆ and B₂H₆ for Low Resistivity W," *Journal of the Electrochemical Society*, vol. 156, no. 9, pp. H685-H689, 2009.
- [16] G. L. Wang *et al.*, "Application of Atomic Layer Deposition Tungsten (ALD W) as Gate Filling Metal for 22 nm and Beyond Nodes CMOS Technology," *Ecs Journal of Solid State Science and Technology*, vol. 3, no. 4, pp. P82-P85, 2014.
- [17] T. Omstead, G. C. D' Couto, S. H. Lee, P. Wongsenakaum, J. Collins, and K. Levy, "Filling high-AR structures using pulsed nucleation layer deposition," *Solid State Technology*, vol. 45, no. 9, pp. 51-+, Sep 2002.
- [18] S. H. Kim *et al.*, "Characterizations of pulsed chemical vapor deposited-tungsten thin films for ultrahigh aspect ratio W-plug process," *Journal of the Electrochemical Society*, vol. 152, no. 6, pp. C408-C417, 2005.
- [19] H. Park, S. Lee, H. J. Kim, E. Yoon, and G.-D. Lee, "Dissociation reaction of B₂H₆ on TiN surfaces during atomic layer deposition: first-principles study," *RSC Advances*, 10.1039/C7RA11291B vol. 7, no. 88, pp. 55750-55755, 2017.

- [20] S. H. Kim, S. J. Yeom, N. Kwak, and H. Sohn, "Phase and microstructure of ALD-W films deposited using B₂H₆ and WF₆ and their effects on CVD-W growth," *Journal of the Electrochemical Society*, vol. 155, no. 2, pp. D148-D154, 2008.
- [21] G. Ramanath *et al.*, "Electromigration in epitaxial Cu (001) lines," in *AIP Conference Proceedings*, 2002, vol. 612, no. 1, pp. 10-20: AIP.
- [22] C. H. Kim, I. C. Rho, S. H. Kim, Y. S. Sohn, H. S. Kang, and H. J. Kim, "Improvement of Adhesion Performances of CVD-W Films Deposited on B₂H₆-Based ALD-W Nucleation Layer," *Electrochemical and Solid State Letters*, vol. 12, no. 3, pp. H80-H83, 2009.
- [23] U. C. Oh and J. H. Je, "Effects of Strain-Energy on the Preferred Orientation of Tin Thin-Films," *Journal of Applied Physics*, vol. 74, no. 3, pp. 1692-1696, Aug 1 1993.
- [24] J. H. Je, D. Y. Noh, H. K. Kim, and K. S. Liang, "Preferred orientation of TiN films studied by a real time synchrotron x-ray scattering," *Journal of Applied Physics*, vol. 81, no. 9, pp. 6126-6133, May 1 1997.
- [25] J. P. Perdew, K. Burke, and M. Ernzerhof, "Generalized gradient approximation made simple," *Physical Review Letters*, vol. 77, no. 18, pp. 3865-3868, Oct 28 1996.
- [26] G. Kresse and J. Furthmuller, "Efficient iterative schemes for ab initio total-energy calculations using a plane-wave basis set," *Physical Review B*, vol. 54, no. 16, pp. 11169-11186, Oct 15 1996.
- [27] S. Grimme, "Semiempirical GGA-type density functional constructed with a long-range dispersion correction," *Journal of Computational Chemistry*, vol. 27, no. 15, pp. 1787-1799, 2006.
- [28] P. E. Blöchl, "Projector augmented-wave method," *Physical Review B*, vol. 50, no. 24, pp. 17953-17979, 12/15/ 1994.
- [29] N. Schonberg, "An X-Ray Investigation on Ternary Phases in the Ta-Ti-N, Ta-Cr-N, Ta-Mn-N, Ta-Fe-N, Ta-Co-N, Ta-Ni-N Systems," *Acta Chemica Scandinavica*, vol. 8, no. 2, pp. 213-220, 1954.
- [30] D. Vanderbilt, "Soft self-consistent pseudopotentials in a generalized eigenvalue formalism," *Physical Review B*, vol. 41, no. 11, pp. 7892-7895, 04/15/ 1990.
- [31] *Everything You Need to Know About Mechanisms*. Available: <http://iverson.cm.utexas.edu/courses/310M/MainPagesSp06/Mechanism.html>

- [32] H. R. Jiang, T. S. Zhao, L. Shi, P. Tan, and L. An, "First-Principles Study of Nitrogen-, Boron-Doped Graphene and Co-Doped Graphene as the Potential Catalysts in Nonaqueous Li-O₂ Batteries," *The Journal of Physical Chemistry C*, vol. 120, no. 12, pp. 6612-6618, 2016/03/31 2016.
- [33] H. Yang *et al.*, "A comparison of TiN processes for CVD W/TiN gate electrode on 3 nm gate oxide," in *International Electron Devices Meeting. IEDM Technical Digest*, 1997, pp. 459-462.
- [34] M. Dammann, M. Chertouk, W. Jantz, K. Köhler, and G. Weimann, "Reliability of InAlAs/InGaAs HEMTs grown on GaAs substrate with metamorphic buffer," *Microelectronics Reliability*, vol. 40, no. 8, pp. 1709-1713, 2000/08/01/ 2000.
- [35] B. Kalanyan, P. C. Lemaire, S. E. Atanasov, M. J. Ritz, and G. N. Parsons, "Using Hydrogen To Expand the Inherent Substrate Selectivity Window During Tungsten Atomic Layer Deposition," *Chemistry of Materials*, vol. 28, no. 1, pp. 117-126, 2016.
- [36] Ciaran Murray and Simon D. Elliott, "Density Functional Theory Predictions of the Composition of Atomic Layer Deposition-Grown Ternary Oxides," *ACS Applied Materials & Interfaces*, vol. 5, pp. 3704-3715, 2013.
- [37] Zheng Hu, Junxia Shi and C. Heath Turner, "Molecular dynamics simulation of the Al₂O₃ film structure during atomic layer deposition," *Molecular Simulation*, vol. 35, no. 4, pp. 270-279, 2009.
- [38] Kristopher S. Brown, Chiara Saggese, Benjamin P. Le Monnier, Florent Héroguel, and Jeremy S. Luterbacher, "Simulation of Gas- and Liquid-Phase Layer-By-Layer Deposition of Metal Oxides by Coarse-Grained Modeling," *The journal of Physical Chemistry C*, vol. 122, pp. 6713-6720, 2018.

Chapter 6. Conclusions

We investigated overall ALD reaction mechanism for W deposition on the TiN surfaces based on DFT calculation as well as the detailed dissociative reactions of precursors, such as B_2H_6 , H_2 & N_2 , and WF_6 .

Firstly, we have investigated the dissociation reaction of B_2H_6 on three different TiN surfaces, TiN (001), Ti-terminated TiN (111), and N-terminated TiN (111), using DFT calculations. N-terminated TiN (111) shows the lowest overall reaction energy for B_2H_6 . These results imply that severe problems, such as a seam or void, in filling the W metal gate for memory devices could be attributed to the difference in the deposition rate of W films on TiN surfaces. From this study, it was found that the control of the texture of the TiN film is essential for improving the subsequent W nucleation.

Secondly, we have investigated the effects of H_2 and N_2 treatment on TiN surfaces for B_2H_6 dosing process. In our DFT calculated results, H_2 treatment on the TiN surfaces is to make the surface to be H-covered TiN surfaces, which results in lowering the reactivity of B_2H_6 precursor since the overall reactions of the B_2H_6 on the H-covered TiN surfaces are energetically less favorable than the TiN surfaces. As a result, an effect of the H_2 treatment is to decrease the reactivity of the B_2H_6 molecule on the TiN surface. However, N_2 treatment on Ti-terminated TiN (111) surface is more likely to make the TiN surface to be N-terminated TiN (111) surface, which results in making a lot of N-terminated TiN (111) surfaces, having very reactive nature for B_2H_6 bond

dissociation. As a result, the effect of N_2 treatment serves as a catalyst to decompose B_2H_6 . From the deep understanding of the effect of H_2 and N_2 during the B_2H_6 dosing process, the use of proper gas treatment is required for improvement of the W nucleation layers.

Lastly, we investigated overall ALD reaction mechanism for W deposition on the TiN surfaces based on DFT calculation as well as the detailed dissociative reactions of WF_6 . Our calculated results suggest that the overall reactions of the WF_6 on the B-covered TiN surfaces are energetically much more favorable than the one on the TiN surfaces, which means that the high reactivity of WF_6 with the B-covered TiN surface is attributed to the presence of B-covered surface made by B_2H_6 molecule. As a result, an effect of the B_2H_6 flow serves as a catalyst to decompose WF_6 molecule. Two additional reaction processes right after WF_6 bond dissociation, such as W substitution and BF_3 desorption, were also explored to clearly understand the detailed reactions that can occur by WF_6 flow. At the first additional reaction process, W atoms can be substituted into B site and covered on the TiN surfaces due to the strong bonding nature of W with the TiN surface than B atoms. At the second additional reaction process, remaining atoms, such as B and F, can be easily desorbed as by-product, that is, BF_3 because BF_3 desorption is energetically favorable reaction with low activation energy. Furthermore, we also investigated the effect of H_2 post-treatment on W-covered TiN surface in order to remove residual F adatoms, which are known to cause severe problems that extremely degrade characteristics of memory devices. It was found that both H_2 dissociative reaction and HF desorption can occur enough well under somewhat high temperature and H_2 ambience, which is confirmed

by the our DFT results and previously reported experimental results. These results imply that the understanding of the role of gas molecules used for W deposition gives us insight into improving the W ALD process for future memory devices.

국문 초록

우리는 DFT 기반으로 W 증착을 위해 사용되는 B_2H_6 , H_2 & N_2 및 WF_6 와 같은 전구체의 분해반응을 통해 WALD 증착 메커니즘을 연구하였다.

우선, ALD W 증착에서 B_2H_6 주입 공정에서 하부막 TiN 층의 반응 메커니즘을 탐구하기 위해 DFT 계산을 기반으로 하여 B_2H_6 분자에 대해 세 가지 TiN 표면에 대한 반응성을 조사하였다. TiN 증착 시 주로 (001) 및 (111) texture를 갖는 poly-crystalline TiN 박막이 관측되기 때문에 본 연구에서는 TiN (001), Ti-terminated TiN (111), and N-terminated TiN (111) 세 가지 표면에 대해 연구를 진행하였다. 결과적으로, 세 가지 표면 중 N-terminated TiN (111) 표면에서 B_2H_6 분해 반응이 가장 잘 일어나며 표면 방향에 따른 W 증착속도 차이로 인해 void 형성 문제가 발생할 수 있음을 해석하였다.

다음으로, B_2H_6 주입 과정에서 H_2 및 N_2 처리가 TiN 표면에 미치는 영향을 조사하였다. 우리의 DFT 계산 결과에서, TiN 표면에 대한 H_2 처리는 TiN 표면을 H 커버된 TiN 표면으로 만드는 것으로 B_2H_6 precursor의 반응성을 낮추는 결과를 낳았다. 그 이유는 H 커버된 TiN 표면에서의 B_2H_6 분해반응은 bare TiN 표면에 비해 에너지적으로 불안정해지는 반응이기 때문이다. 결과적으로, H_2 처리의 효과는 TiN 표면의 B_2H_6 분자의 반응성을 감소시켜서 표면을 passivation 시키는 역할을 한다. 그러나, N_2 처리는 TiN 표면을 N-terminated TiN (111) 표면을 많이 만들어서 B_2H_6 분해반응이 잘 일어나도록 해준다. 결과적으로, N_2 처리의 효과는 B_2H_6 를 분해시키는 촉매 표면을 만드는 역할을 한다. B_2H_6 주입 공정 동안 H_2 및 N_2 의 적절한 gas 사용은 W 박막 특성에 큰 영향을 미칠 수 있을 것으로 기대된다.

마지막으로, 우리는 WF_6 의 분해반응뿐만 아니라 DFT 계산에 기초한 TiN 표면위에서의 W 증착에 대한 전반적인 ALD 반응 메커니즘을 조사했다. 결과적으로 bare TiN 표면 대비 B-covered TiN 표면에서 WF_6 분자의 분해반응이 에너지 적으로 훨씬 유리한 것으로 나타났으며, 이를 통해 B_2H_6 주입의 효과는 WF_6 분자를 분해시키는 촉매 표면을 만드는 역할을 한다. W 치환과 BF_3 탈착과 같은 WF_6 분해반응이 일어난 직후의 두 개의 추가 반응 과정도 정확한 반응 메커니즘을 이해하기 위해 수행되었다. 첫 번째 추가 반응 과정에서 W 원자는 B 원자에 비해 TiN 표면과의 binding energy가 훨씬 높아서 B 원자와 치환이 가능하다. 두 번째 추가 반응 과정에서, BF_3 탈착은 낮은 에너지배리어와 에너지 적으로 안정해지는 반응이기 때문에 B 및 F와 같은 잔류 원자들은 BF_3 로 쉽게 탈착 될 수 있다. 또한, 우리는 메모리 소자의 특성을 극도로 저하시키는 심각한 문제를 일으키는 것으로 알려진 잔류 F 원자를 제거하기 위해 W-covered TiN 표면에 대한 H_2 후 처리의 영향을 조사하였다. H_2 분해반응과 HF 탈착은 우리의 DFT 결과 및 이전에 보고된 실험 결과에 의해 확인되는 다소 높은 온도 및 H_2 분위기 하에서 충분히 잘 일어날 수 있는 것으로 밝혀졌다. 이러한 결과는 W 증착에 사용된 가스 분자의 역할에 대한 이해가 향후 메모리 소자에 대한 W ALD 공정 개선에 대한 통찰력을 제공할 것으로 기대된다.

주요어 :

제일원리계산, 원자층 증착법, 텅스텐, 분해반응, 에너지 배리어, B_2H_6 , WF_6

학번 : 2014-21439

Publication List

Journal Papers:

1. **Hwanyeol Park**, Sungwoo Lee, Ho Jun Kim, Euijoon Yoon* and Gun-Do Lee*, “Dissociation reaction of B_2H_6 on TiN surfaces during atomic layer deposition: first-principles study”, RSC Advances, Vol. 7, 55750, (2017).
2. **Hwanyeol Park**, Sungwoo Lee, Ho Jun Kim, Daekwang Woo, Se Jun Park, Kangsoo Kim, Euijoon Yoon* and Gun-Do Lee*, “Effects of H_2 and N_2 treatment for B_2H_6 dosing process on TiN surfaces during atomic layer deposition: An ab-initio study”, RSC Advances, Vol. 8, pp. 21164 (2018).
3. **Hwanyeol Park**, Sungwoo Lee, Ho Jun Kim, Daekwang Woo, Jong Myeong Lee, Euijoon Yoon* and Gun-Do Lee*, “Overall reaction mechanism for a full atomic layer deposition cycle of W films on TiN surfaces: First-principles study”, RSC Advances, Vol. 8, pp. 39039 (2018).
4. **Hwanyeol Park**, Sungwoo Lee, Ho Jun Kim, Daekwang Woo, Se Jun Park, Jong Myeong Lee, Euijoon Yoon* and Gun-Do Lee*, “Effects of nitrogen doping in amorphous carbon layers for diffusion of fluorine atom: First-principles study”, Journal of Applied Physics (Under revision).
5. **Hwanyeol Park**, Gun-Do Lee, Euijoon Yoon, Ho Jun Kim*, “Analysis of surface adsorption kinetics of SiH_4 and Si_2H_6 for deposition of a

- hydrogenated silicon thin film using intermediate pressure SiH₄ plasmas”, Applied Surface Science (submitted).
6. Ji-Yong Kim, **Hwanveol Park**, Sungwoo Lee, Dae-Hyun Nam, Wonhyo Joo, Hyoung Gyun Kim, In-Kyoung Ahn, Ho-Young Kang, Gi-Baek Lee, In-ho Jung, Mi-Young Kim, Gun-Do Lee, and Young-Chang Joo*, “Gaseous Activity Regulation for Stoichiometric Modification of Ni Phosphide/Carbon Nanofibers as Electrocatalysts”, Advanced Functional Materials (Submitted).
 7. So-Yeon Lee, Kyung-Tae Jang, Min-Woo Jeong, **Hwanveol Park**, Geon-Tae Kim, Gun-Do Lee, Mi-Young Kim and Young-Chang Joo*, Bonding structure and etching characteristics of amorphous carbon for a hardmask deposited by DC sputtering, Carbon (Under review)
 8. Gun-Do Lee, Alex Robertson, Sungwoo Lee, **Hwanveol Park**, Young-Chang Joo, Euijoon Yoon, Jamie H. Warner, and Chris P. Ewels*, “Direct Observation and Catalytic Role of Mediator atom in 2D and 3D materials”, Nature Materials (Complete of 1st Revision).
 9. Jeonghwan Jang[‡], Seung-Yong Lee[‡], **Hwanveol Park**, Sangmoon Yoon, Gyeong-Su Park, Gun-Do Lee, Yongjo Park, Miyoung Kim*, and Euijoon Yoon*, “Solid-phase epitaxial growth of an alumina layer having a stacking-mismatched domain structure of the intermediate γ -phase”, ACS Applied Materials & Interfaces, Vol. 10, 48, 41487-41496 (2018).
 10. Dae-Myeong Geum, SangHyeon Kim, SooSeok Kang, Hosung Kim, **Hwanveol Park**, Pyo Rho, Seung Yeop Ahn, Jindong Song, Won Jun Choi, and Euijoon Yoon*, "Room temperature operation of mid-infrared InAs_{0.81}Sb_{0.19} based photovoltaic detectors with an In_{0.2}Al_{0.8}Sb barrier layer grown on GaAs substrates", Optics Express, Vol. 26, No. 6249, pp.

6259 (2018).

11. Sehun Park, Daehan Choi, **Hwanyeol Park**, Daeyoung Moon, Duk Kyu Bae, Euijoon Yoon*, and Yongjo Park*, "Suppression of surface leakage current in InSb photodiode by ZnS passivation", International Journal of Nanotechnology, Vol. 13, (2016).

Conference Presentation:

International conferences

1. **Hwanyeol Park**, Sungwoo Lee, Shanshan Wang, Euijoon Yoon, Jamie H. Warner, and Gun-Do Lee, “Detailed Atomic Reconstruction of Extended Line Defects in Monolayer MoS₂”, Graphene 2017, 2017.03.29, Barcelona, Spain.
2. **Hwanyeol Park**, Sehun Park, Dae-Myeong Geum, Yongjo Park and Euijoon Yoon, “High quality AlInSb electron blocking layer grown by MOCVD for performance enhancement of AlInSb/InSb infrared photodetectors”, IVC-20, 2016.08.25, BEXCO, Pusan, Korea.
3. **Hwanyeol Park**, Sehun Park, Dae-Myeong Geum, Won Jun Choi, Yongjo Park and Euijoon Yoon, “Epitaxial growth and characterization of Al_xIn_{1-x}Sb barrier layer for high performance MWIR InSb photodetector”, The 18th International Conference on Crystal Growth and Epitaxy, 2016.08.10, Nagoya, Japan.
4. Sehun Park, Daehan Choi, **Hwanyeol Park**, Daeyoung Moon, Yongjo Park and Euijoon Yoon, “Study of InSb surface passivation and its effects on electrical properties”, 16th International Conference on Thin Films (ICTF-16), October, 13-16, Dubrovnik, Croatia.
5. Chulkyun Seok, Sujin Kim, Jaeyel Lee, Sehun Park, **Hwanyeol Park**, Yongjo Park and Euijoon Yoon, “Analysis for degradation cause of SiO₂ passivation layer deposited on InSb using PECVD”, The 5th

International Conference on Microelectronics and Plasma Technology (ICMAP), 2014.07.10, GSCO, Gunsan, Korea.

6. Chulkyun Seok, Seungmin Lee, Sehun Park, **Hwanyeol Park**, Yongjo Park and Euijoon Yoon, “Epitaxial growth and coalescence of InSb nano crystals on GaAs substrate using MOCVD”, NANO KOREA 2014, 2014.07.04, COEX, Seoul, Korea.

Domestic conferences

1. **Hwanyeol Park**, Sungwoo Lee, Ho Jun Kim, Daekwang Woo, Jong Myeong Lee, Euijoon Yoon, Gun-Do Lee, “Reactivity of WF_6 precursor on TiN Surfaces for Tungsten Atomic Layer Deposition: An ab-initio study”, 2018 가을 한국물리학회, 2018.08.26, 창원컨벤션센터, 창원.
2. **Hwanyeol Park**, Sungwoo Lee, Ho Jun Kim, Daekwang Woo, Euijoon Yoon, Gun-Do Lee, “Ab initio study of the reactivity of B_2H_6 molecule on TiN Surfaces for Tungsten Atomic Layer Deposition”, 제14회 고등과학원 전자구조 계산학회, 2018.06.05, 고등과학원, 서울.
3. **Hwanyeol Park**, Sungwoo Lee, Ho Jun Kim, Euijoon Yoon, Gun-Do Lee, “First principles analysis of the role of B_2H_6 on TiN Surfaces for Tungsten Atomic Layer Deposition”, 2018 봄 한국물리학회, 2018.02.27, 대전컨벤션센터, 대전.

4. **Hwanyeol Park**, Sungwoo Lee, Shanshan Wang, Jamie H. Warner, Gun-Do Lee, Euijoon Yoon, “Atomic Structure and Band Gap Tuning of Extended Line Defects in Monolayer MoS₂” 제1회(창립) 한국LED·광전자학회 학술대회, 2018.02.22, 차세대융합기술연구원, 수원.
5. **Hwanyeol Park**, Sungwoo Lee, Shanshan Wang, Jamie H. Warner, Gun-Do Lee, Euijoon Yoon, “Detailed atomic reconstruction of extended line defects in monolayer MoS₂” 제13회 고등과학원 전자구조 계산학회, 2017.06.15, 고등과학원, 서울.
6. **Hwanyeol Park**, Dae-Myeong Geum, Yongjo Park and Euijoon Yoon, “Analysis on epitaxially grown AlInSb layers using MOCVD for AlInSb/InSb barrier infrared photodetectors”, 2016 가을 한국재료학회, 2016.11.18, 경주 현대호텔, 경주.
7. **Hwanyeol Park**, Dae-Myeong Geum, Yongjo Park and Euijoon Yoon, “Study of AlInSb epitaxial layers grown by metal organic chemical vapor deposition for AlInSb/InSb barrier infrared photodiodes”, 2016 봄 한국재료학회, 2016.05.19, 여수 디오션 리조트, 여수.
8. **Hwanyeol Park**, Sehun Park, Dae-Myeong Geum, Yongjo Park and Euijoon Yoon, “Epitaxial growth and characterization of Al_xIn_{1-x}Sb layers on InSb substrate by LP-MOCVD”, 2015 가을 한국재료학회, 2015.11.26, 부산 해운대 그랜드호텔, 부산.

9. **Hwanveol Park**, Sehun Park, Yongjo Park and Euijoon Yoon, “Reduction of dark current in InSb photodiode through band alignment engineering of barrier layer”, 제22회 한국반도체학술대회, 2015.02.12, 송도컨벤시아, 인천.
10. 박세훈, **박환열**, 김상혁, 최원준, 송진동, 오은순, 박용조, 윤의준, “Low temperature photoluminescence of MOCVD grown InSb epilayers”, 2015 가을 한국재료학회, 2015.11.26, 부산 해운대 그랜드호텔, 부산.
11. 석철균, **박환열**, 최대한, 임원철, 송종한, 박용조, 송진동, 윤의준, “Be 임플란트된 InSb 기판의 열처리를 통한 결함 회복 및 활성화 연구”, 2014 한국군사과학기술학회 종합무기학술대회, 2014.06.20, 국제컨벤션센터, 제주.
12. 박세훈, 최대한, **박환열**, 석철균, 박용조, 윤의준, “유도결합 플라즈마 화학 기상 증착법(ICP-CVD)을 이용한 Si₃N₄ 박막 증착 연구”, 2014 한국군사과학기술학회 종합무기학술대회, 2014.06.19, 국제컨벤션센터, 제주.
13. 석철균, 최대한, 이재열, 김수진, 박세훈, **박환열**, 박용조, 윤의준, “적외선 검출기용 InSb FPA 표면에 형성되는 Passivation 층의 열화 및 이에 의한 특성 파괴 메커니즘 연구”, 2014 한국군사과학기술학회 종합무기학술대회, 2014.06.19, 국제컨벤션센터, 제주.